Politecnico di Torino

Scuola di Dottorato
Dottorato in Ingegneria Meccanica - XXXI Ciclo

Tesi di Dottorato

Refined one-dimensional models applied to biostructures and fluids

Daniele Guarnera

Supervisors
Prof. Erasmo Carrera
Dr. Alfonso Pagani

February 2019

Acknowledgements

L'esperienza del dottorato stata una bellissima fase della mia vita e per questo desidero ringraziare prima di tutto colui che me ne ha data l'opportunità, il Professor Carrera. La sua personalità, la sua professionalità e il costante supporto sono stati una guida fondamentale in questo percorso di ricerca. Naturalmente, un doveroso grazie va a tutti i componenti del gruppo MUL2, Alfonso, Enrico, Matteo, Marco e Mirella, senza il cui aiuto probabilmente non avrei scritto nemmeno una riga. Un ringraziamento speciale va ai ragazzi con cui ho iniziato quest'avventura, Alberto, Liuk e Ibrahim per tutti momenti passati insieme e per tutte quelle volte che, devo ammetterlo, mi hanno fatto da supervisors aggiunti. Grazie inoltre, ad Andrea e Riccardo, per l'aiuto reciproco, gli scambi e le risate in ufficio. In ultimo, ma solo per ragione di tempo, desidero ringraziare Marianna, per questa importante esperienza americana, da dove peraltro, sto scrivendo queste parole.

Abstract

Fast, reliable and accurate computational methods are highly sought in biomechanics. To reduce the amount of invasive tests and to predict the mechanical response of biological components and anatomic parts, the Finite Element Method is the most popular approach. Despite the accuracy of FEM, the analyses often require prohibitive computational times. This work proposes a novel approach for the analysis of bio-structures and fluids, with low computational cost, based on the use of higher-order 1D models, developed within the Carrera Unified Formulation. Whitin CUF, it is possible to express the unknown field (i.e. velocity, displacements etc.) by using an arbitrary expansion. Refined, hierarchical models can be obtained, where the order of approximation is a free parameter of the analysis. The cross-section is described through the use of the expansion function and the equations are expressed in terms of fundamental nuclei (FN).

A new approach for the computational analysis of anatomic structures based on CUF is presented in this manuscript, called Component-Wise approach (CW). CW allows to model multi-component and multi-material structures through 1D CUF models automatically accounting for the interfaces. First, examples are shown for static and free-vibration analysis of various complex bio-component. Then, extension to nonlinear CUF frameworks is introduced, which is fundamental to model tissues that show high nonlinearities. In this context, the CUF approach provides accurate predictions reducing extremely the analysis time.

Parallel to the structural formulation, 1D CUF models for the Computational Fluid Dynamics (CFD) have been developed. In particular, 1D formulations for incompressible and highly viscous fluids have been derived from Navier-Stokes equations. Similarly to the structural models, Taylor and Lagrange polynomial are used to describe velocity and pressure, even in presence of different boundary conditions. CFD/CUF approach has been extended to *node-dependent* kinematic models (NDK), which is an adavnced modelling method that allows to modify the kinematics of the model node-by-node. This novel techinique allows the enhancement of the approximation only in limited parts of the domain, providing flexibility and reducing furtherly the computational effort.

Validation has been provided for a large number of numerical examples. Typical biomechanics structures, as tendons or arterial tissues, have been analyzed in linear and nonlinear regime. Flows in cylindrical and non-conventional pipes have been investigated, taking into account different velocity profiles. Results show that CUF models, with uniform or variable kinematics, provide accurate and reliable results, in terms of stress/strain fields and flow parameters. The last part of the work has been dedicated to the Fliud-Structure Interaction (FSI), to provide the ground work for a future method for the efficient description of this interaction.

Sommario

La velocità e l'affidabilità delle analisi condotte per via di metodi computazionali, sono caratteristiche altamente richieste in tutte le branche della meccanica, sopratutto quando devono interfacciarsi con realtà non più meramente accademiche. Da questo punto di vista, la biomeccanica, e i suoi risvolti in campo clinico, rappresenta un esempio calzante. L'idea di poter predire con sufficiente accuratezza il comportamento di qualsivoglia bio-struttura senza ricorrere all'uso di test invasivi o dispendiose prove di laboratorio, ha spinto fortemente allo sviluppo di modelli computazionali avanzati. Gli approcci più utilizzati sono i metodi numerici, come gli elementi finiti (FEM) o simili, in quanto si prestano abilmente ad implementazioni all'interno di codici numerici automatici e forniscono risultati affidabili. Tuttavia, nonostante la potenza di calcolo delle macchine moderne, il costo computazionale richiesto per ottenere tale affidabilità in applicazioni tipiche della biomeccanica, risulta spesso proibitivo. È per questo motivo che lo sviluppo di modelli ridotti diventa fondamentale ed è in questo contesto che si inserisce questa tesi. Questo lavoro infatti, propone un nuovo approccio per l'analisi di bio-strutture e fluidi con costi computazionali notevolmente ridotti. Tale approccio è basato sull'utilizzo di modelli 1D ad alto ordine, sviluppati in seno alla Carrera Unified Formulation (CUF). Attraverso la CUF è possibile esprimere il campo incognito (velocità, spostamento etc.) per mezzo di un'espansione arbitraria delle incognite generalizzate; in questo modo si ottengono modelli gerarchici e raffinati, in cui l'ordine delle variabili incognite è un parametro libero del problema. L'espansione attraverso la sezione trasversale del modello avviene per mezzo di polinomi interpolanti, e, nel presente lavoro, sono stati impiegati polinomi di Taylor (TE) e di Lagrange (LE). A prescindere dalla scelta di tali funzioni, le equazioni vengono espresse in termini di nuclei fondamentali che sono indipendenti dalla classe e dall'ordine polinomiale.

Sulla base della tecnica CUF, si sviluppano modelli avanzati atti a descrivere il comportamento meccanico di strutture complesse, quali parti anatomiche. Attraverso l'approccio Component-Wise (CW), si possono modellare strutture multi-component attraverso singoli modelli CUF-1D, garantendo comunque continuità alle interfacce. Tale approccio, oltre che per analisi della risposta statica, viene impiegato per l'analisi delle vibrazioni libere. In questa tesi, viene proposta inoltre un'estensione della teoria che tiene conto della non-linearità fisica dei materiali biologici. Diversi tessuti infatti, come ossa o tendini, presentano una spiccata plasticità ad alti carichi, la cui descrizione richiede tecniche iterative che allungherebbero ulteriormente i tempi delle analisi se affrontati con metodi convenzionali.

Parallelamente alla formulazione strutturale, sono stati sviluppati modelli CUF-1D per la fluido-dinamica computazionale (CFD). In particolare, a partire dalle equazioni di Navier-Stokes sono state derivate formulazioni 1D per fluidi incomprimibili ad alta viscosità. Come per i modelli strutturali, la CUF si avvale dei polinomi di Taylor e di Lagrange per descrivere agilmente velocità e pressione anche in presenza di particolari condizioni al contorno. In questo contesto, la formulazione è stata estesa a modelli con cinematica *node-dependent*, ossia modelli che permettono di arricchire l'accuratezza dell'approssimazione solo in alcune parti del dominio, garantendo così maggiore flessibilità al metodo e riducendo ulteriormente lo sforzo computazionale.

I modelli proposti in questo lavoro sono stati verificati per mezzo di un largo numero di esempi numerici. Strutture tipicamente studiate dalla biomeccanica, come tendini e tessuti arteriosi, sono state analizzate in regime lineare e non-lineare, evidenziando le vaste potenzialità dei modelli CUF-1D in termini di accuratezza e costi computazionali. I modelli 1D proposti infatti, riescono a descrivere perfettamente lo stress/strain anche localmente, in strutture dalle geometrie molto complesse. Per quanto riguarda la fluido-dinamica, sono stati sviluppati flussi in condotti cilindrici e non, con diversi profili di velocità. Anche in questo caso si è potuto evidenziare come i modelli CUF, a cinematica fissa e variabile, forniscono risultati accurati e affidabili. A valle di tali esempi, le ultime pagine riguardano l'interazione fluido-struttura. Gli esempi proposti, seppur semplificati, gettano le basi per una formulazione unificata in grado di descrivere tale interazione in maniera diretta e meno dispendiosa in termini di costi computazionali.

Contents

Acknowledgements **i**

Abstract **iii**

Sommario **v**

List of Figures **xi**

List of Tables **xv**

1 Introduction **1**
- 1.1 Computational Mechanics for Bio-Applications 1
  - 1.1.1 What is the Biomechanics? 1
  - 1.1.2 Contribution of Biomechanics to Medicine 2
  - 1.1.3 The Computational Biomechanics 2
- 1.2 A brief review on the Carrera Unified Formulation 3
  - 1.2.1 One-dimensional models for Fluid-Dynamics 6

2 Carrera Unified Formulation for Structural Mechanics **9**
- 2.1 Refined one-dimensional models 9
  - 2.1.1 Preliminaries 9
  - 2.1.2 Refined beam models 11
    - Taylor Expansion 11
    - The Lagrange Expansion 13
  - 2.1.3 The Component-Wise approach 14
- 2.2 Finite Element Method 15
- 2.3 Principle of Virtual Displacements and Governing Equations 16
- 2.4 Matrices 18
- 2.5 FEM for Nonlinear Problems 22
  - 2.5.1 The Newton-Raphson Method 22
  - 2.5.2 The Nonlinear Plasticity 23
- 2.6 The Carrera Unified Formulation for nonlinear problems 24

3 Carrera Unified Formulation for Fluid-Dynamics **27**
- 3.1 Stokes equations and Galerkin approximation 27

- 3.1.1 Boundary conditions . . . 29
- 3.1.2 Galerkin approximation . . . 30
- 3.2 One-dimensional Carrera Unified Formulation models for Stokes flows 31
- 3.3 Finite Element formulation . . . 31
- 3.3.1 The fundamental nuclei for Computational Fluid Dynamics . 32
- 3.4 Boundary conditions . . . 35

4 Computational Fluid Dynamics and Carrera Unified Formulation with Node-Dependent Kinematics 39
- 4.1 One-dimensional fluid-dynamics models with Node-Dependent Kinematics . . . 39
- 4.2 The NDK model for Fluid-Dynamics . . . 41

5 Numerical Results 45
- 5.1 Structural Mechanics - Linear Materials . . . 45
- 5.1.1 Atherosclerotic Plaque . . . 45
- 5.1.1.1 Static Analysis . . . 47
- 5.1.1.2 Free Vibration Analysis . . . 49
- 5.1.2 Dental Prosthesis . . . 51
- 5.1.2.1 Static Analysis . . . 52
- 5.1.2.2 Free Vibration Analysis . . . 55
- 5.2 Structural Mechanics, Physical Nonlinearity . . . 58
- 5.2.1 Static Analysis: Lumbar Vertebra . . . 58
- Shear test . . . 61
- 5.2.2 Static Analysis: Achilles Tendon . . . 62
- 5.2.3 Static Analysis: Artery, healty and diseased . . . 65
- . . . 67
- 5.3 Computational Fluid Dynamics . . . 71
- 5.3.1 The Poiseuille Flow . . . 71
- 5.3.2 Different Velocity Profiles at Inlet . . . 74
- 5.3.3 Square-section Pipes . . . 77
- 5.3.3.1 Instability . . . 79
- 5.3.4 Change section pipes . . . 80
- 5.4 Computational Fluid Dynamics with Node-dependent Kinematics . 83
- 5.4.1 Poiseuille flow analysis . . . 83
- 5.4.2 Analysis of flow with complex inlet velocity profiles . . . 85
- 5.4.3 Analysis of a flow in a square-section pipes . . . 88
- 5.5 Fluid-Structure Interaction . . . 92
- 5.5.1 Introduction . . . 92
- 5.5.2 Circular Pipe . . . 93
- 5.5.3 Artery Profile . . . 94

6 Conclusions 97
- 6.1 Remarks . . . 97

6.2 Future Developments 98

List of Figures

1.1 Leonardo da Vinci's sketch on *Anatomia Humana*. 1

2.1 Generic beam structure and system of reference 10
2.2 Homogeneous condition of transverse stress components at the unloaded edges of the beam 11
2.3 The Taylor Expansion model 12
2.4 The Lagrange Expansion model 13
2.5 Component-Wise approach applied to dental prosthesis. 14
2.6 1D Lagrange polynomials as shape functions of B3 element 16
2.7 Derivation of the element stiffness matrix from the fundamental nucleus. Example procedure for a B3 element and L4 Lagrange expansion function. 20
2.8 Classical FEM assembly procedure of two B3 element matrices . . . 20
2.9 Load-displacemnt: application of the NR method for 1-DOF system 23

3.1 Computational domain Ω. 28
3.2 CUF LE model discretizations of pressure and velocity fields. 32
3.3 Procedure to build the finite element matrices and vectors expanding the fundamental nuclei. Scheme for *momentum* conservation equation. 33
3.4 Condensed problem in FE scheme. 35
3.5 Pipe with circular cross-section 36

4.1 A scheme of three different level of accuracy on the description of circulatory system. Image taken from [1] 40
4.2 A three-node 1D finite element with node-dependent kinematics. . . 41
4.3 FEM model of fluid-dynamics model using node-dependent kinematics. The expansion of the velocity and of the pressure fields change node-by-node and this determines the dimension of the matrices. 42

5.1 Atherosclerotic plaque. Materials subdivision (a) and LE9 subdivision (b) 46
5.2 Horizontal displacement component u_x on the mid-span cross-section. Comparison between TE ($N = 4$ to $N = 20$), LE, and 3D NASTRAN Solid model. Values in mm. 47

5.3 Axial stress σ_{yy} MPa distribution on the mid-span cross-section of the atherosclerotic plaque subjected to clamped-free boundary conditions and forces along y. 49
5.4 Representative mode shapes of the atherosclerotic plaque; CW model. 50
5.5 Modal Assurance Criterion (MAC) between 3D FEM solution and LE model. 50
5.6 Dental Implant. Geometry (a) and implant in gingiva (b) 52
5.7 Deformed states of the cantilever implant subjected to the masticatory force. 53
5.8 Deformed states of the dental implant with gingiva and bone. . . . 54
5.9 Cross-sectional stress distribution (σ_{yy}, MPa) at the implant/bone (a) and bone (b) regions of the dental implant; CW model. 54
5.10 Natural frequencies of the dental implant vs. numerical model adopted. 56
5.11 Representative mode shapes of the dental implant; CW model. . . . 56
5.12 MAC matrix of the eigenvectors from traditional 3D FEM solution and 36LE CW model. 57
5.13 Lumbar vertebra. Materials subdivision (a) and geometry (b) . . . 58
5.14 Von Mises stress comparison between 72LE-20B4 CUF model and 3D NASTRAN model, in MPa. Linear compression analysis. A-A cross-section. 59
5.15 Nonlinear compression analysis. Stress-strain curves comparison between two 1D CUF models (a) von Mises stress contour plots comparison between best 1D model and solid model (b). Values are in MPa. 60
5.16 Relative error of the plastic equivalent strain. Numbers 10 and 20 indicate the number of finite elements used along the beam axis. . . 61
5.17 Propagation of the equivalent plastic strain along the A-A cross-section. The top-left image represents the 50 % of load. Nonlinear compression analysis. 61
5.18 Nonlinear shear analysis. Von Mises stress contour (in MPa) plots comparison between most refinied 1D model and solid 3D solution. 62
5.19 Relative error of the plastic equivalent strain. Numbers 10 and 20 indicate the number of finite elements used along the beam axis. Nonlinear shear analysis. 63
5.20 The Achille's Tendon geometry 63
5.21 The Achille's Tendon nonlinear analysis: Comparison between 1D CUF and 3D NASTRAN models of σ_{yy} (in MPA) and PEEQ, at longitudinal cross-section A-A. 64
5.22 The Achille's Tendon nonlinear analysis: trends of displacements and inelastic eq. strain (a); 3D sketch of the model at the end of the analysis. The displacement values are in [mm]. 65
5.23 Relative error of the plastic equivalent strain and von Mises stress. Nonlinear shear analysis. 65

5.24 Plastification starting point of Achille's tendons with different cross-section geometry. . . . 66
5.25 The atherosclerotic plaque and its materials. . . . 66
5.26 Principal stress along x direction. Comparison between linear and nonlinear models. . . . 67
5.27 Convergence analysis of von Mises stress for linear and nonlinear models respect to NASTRAN 3D solutions. . . . 68
5.28 Displacement ditribution, in mm, on the midspan cross-section: linear model (a) nonlinear model (b). LE55 models. . . . 68
5.29 Measure of inelastic equivalent strain of CUF models. 3D NASTRAN (a) and 1D CUF model (b). . . . 69
5.30 Comparison between diseased and non-diseased artery portion. Values of displacement in mm, **u**, and PEEQ on the left; on the right, the cross-section of the deformed non-diseased case with a blood pressure five times greater than nominal. . . . 69
5.31 Poiseuille flow velocity profile at $y = 3$ m, $z = 0$. . . . 72
5.32 Pressure trend comparison between LE and TE models along the longitudinal axis y (a), 3D scheme of the pressure trend of the Lagrange model $5L16^U$ - $5L9^P$, results are in m^2/s^2 (b). Poiseuille flow. . . . 73
5.33 Trend of L^2 norm of pressure relative error. Convergence analysis of TE and LE models (a) and of two different Lagrange models (b). 74
5.34 Fourth-order inlet boundary condition. The profile for axial velocity u_y (a), and for pressure (b). Comparison of OpenFOAM results with CUF reuslts. . . . 75
5.35 3D plot of axial velocity profile through the transition area in [m/s]. Fifth-order inlet boundary condition, TE model, $N^U = 6, N^P = 5$. . 77
5.36 Fifth-order inlet boundary condition. Transition of u_y axial velocity (a); pressure shapes across the inlet section(b). Comparison of OpenFOAM results with CUF results. . . . 77
5.37 Example of Lagrange elements across the section. 1xL9 for Velocity and 1xL4 for Pressure. . . . 78
5.38 Second-order flow in a square-section pipe. Parabolic behaviour of the axial velocity (a); decreasing pressure along the conduct (b). . . 78
5.39 Axial velocity u_y in square-section pipe. Comparison of three different models (a),(b),(c), values are in [m/s]; 3D plot of u_y of $4L9^U 4L4^P$ model (d). . . . 79
5.40 Pressure trend comparison: models with different FE order of the y-axis (a); models with different order of expansion across the section (b). . . . 80
5.41 Transversal narrowing conduct geometry. . . . 80
5.42 Longitudinal velocity trends along the centerline of the pipe. . . . 81
5.43 Comparison between the $48LE^{U,P}$ one-dimensional model with finite volume model. Longitudinal trend (a) and transversal distribution (b). . . . 82

5.44 Longitudinal pressure distribution on yz-plane. Comparison between the $48LE^{U,P}$ one-dimensional model with finite volume model. 82
5.45 Pressure trends of the Poiseuille flow. Comparison between constant and node-dependent kinematic one-diemnsional models. The gray part defines the region of domain in which NDK models change the kinematics. 84
5.46 Velocity trends of the Poiseuille flow. Comparison between constant and node-dependent kinematic one-diemnsional models. 84
5.47 Node-dependent kinematics scheme of fourth-order inlet velocity case. Changing of expansion order for velocity N^U and pressure N^P node-by-node. 85
5.48 Comparison of the presure path between uniform and NDK 1D CUF models. The gray area denotes the domain where the TE2,0 model has been used. Fourth-order inlet velocity profile. 86
5.49 Comparison of the velocity distribution between CUF-1D models and OpenFOAM results at inlet and midspan cross-section. Fourth-order inlet velocity profile. 87
5.50 Fifth-order inlet boundary condition, ditrubutions across the section. Velocity (a) and pressure (b). 88
5.51 Comparison of the velocity distribution between CUF-1D models and OpenFOAM results at inlet and midspan cross-section. Fifth-order inlet velocity profile. 88
5.52 Scheme of the one-dymensional model with mixed kinematics LE/TE. 89
5.53 Comaprison of pressure trends for different one-dimensional models. The gray area denotes the domain where the NDK model with $TE^{4,0}$ model has been used. 90
5.54 Parabolic shape of axial velocity at 8^{th} where the change of kinematics is. 90
5.55 Scheme of Lagrange points between structural and fluid-dynamic domain. 92
5.56 One-dimensional fluid-dynamic analysis of an incompressible highly viscous flow. Pressure trend (a) and velocity trend (b). 93
5.57 Displacement field of a pipe subjected to fluid pressure. Linear and decay along the pipe axis (a), 3D sketch of the deformed pipe (b). . . 94
5.58 Fluid-dynamic analysis of blood flow whitin artery affected by atherosclerotic plaque. Axial velocity distribution along the inlet and midspan cross-sections (a), pressure decay along the vessel(b). 95
5.59 Mechanical static resposnse of arterial walls under effect of blood flow. Displacement and deformation trends in Fibrous Cap along the vessel (a), displacement magnitude 3D sketch (b). 96
5.60 Shear deformation at midspan-cross-section. 96

List of Tables

2.1 MacLaurin's polynomials . . . 12

5.1 Materials properties of the atherosclerotic plaque. . . . 46
5.2 Maximum horizontal displacement component, u_x (mm), of the atherosclerotic plaque subjected to internal pressure. . . . 48
5.3 In-plane normal, σ_{xx}, and shear, σ_{xz}, stress components (10^2 MPa) on each material of the atherosclerotic plaque at mid-span cross-section subjected to internal pressure. . . . 48
5.4 Values of σ_{yy} MPa and u_x mm for different points and materials of the section. . . . 49
5.5 Natural frequencies (Hz) of the clamped-clamped atherosclerotic plaque. . . . 50
5.6 Mechanical properties of the materials used in the study of the dental implant. . . . 51
5.7 Displacements components mm measured at three different points of the cantilever implant. . . . 53
5.8 Stress components, in MPa, measured at two different points of the cantilever implant. . . . 54
5.9 Stress components (in MPa) measured at three different points of the dental implant with gingiva and bone. . . . 54
5.10 Natural frequencies (Hz) of the cantilever dental implant (see Fig. 5.7). 55
5.11 Materials properties of the lumbar vertebra. The Young's modulus is expressed in MPa. . . . 59
5.12 Linear compression analysis. Results from 1D CUF models and 3D solution in section A-A. Values are in MPa. . . . 59
5.13 Nonlinear compression analysis. Results from 1D CUF models and 3D solution in section A-A. Values of stresses are in MPa. . . . 60
5.14 Nonlinear shear analysis. Results from 1D CUF models and 3D solution in section A-A. Values of stresses are in MPa. . . . 62
5.15 Nonlinear static analysis of the Achille's Tendon: values of different 1D CUF and 3D NASTRAN models. Values are in MPa . . . 64
5.16 Comparison between two Achille's tendons with different geometries. Values of Von Mises stress, longitudinal stress and plastic equivalent strain. . . . 66
5.17 Comparison between linear and nonlinear models. Values of σ_{xx} and von Mises stress. . . . 67

5.18 Comparison between linear and nonlinear models. Values of von Mises stress of 1D CUF and 3D NASTRAN models. 68
5.19 Inlet pressure and maximum axial velocity at y=3 in terms of percentage errors versus analytical solution for the Poiseuille flow. Comparison of OpenFOAM results with CUF results. 73
5.20 Maximum inlet pressure and maximum axial velocity at $y = 3$m. Comparison of OpenFOAM results with CUF results, fourth-order inlet velocity profile. 75
5.21 Maximum inlet pressure and maximum axial velocity at $y = 3$m. Comparison of OpenFOAM results with CUF results, fifth-order inlet velocity profile. 76
5.22 Flow and geometry data. 80
5.23 Maximum inlet pressure and axial velocity at $y = 3.0$m and $z = 0$m . Comparison of FLUENT results with CUF results, constant inlet velocity profile. 81
5.24 Values of pressure at inlet and midspan sections. Comparison of CUF-1D results. Fourth-order inlet velocity profile. 86
5.25 Maximum value of pressure at inlet y=0m and maximum axial velocity at midspan y=3m. Comparison among different 1D CUF results and OpenFoam solutions .Fourth-order inlet velocity profile. 87
5.26 Maximum value of pressure at inlet y=0m and maximum axial velocity at midspan y=3m. Comparison among different 1D CUF results and OpenFoam solutions. Fifth-order inlet velocity profile. . 89
5.27 Input data of the model. 93
5.28 Results of displacements, von Mises stress and Plastic equivalent strain for linear and nonlinear model. 94
5.29 Fluid data input. 95

Ad Alessio.

Chapter 1

Introduction

1.1 Computational Mechanics for Bio-Applications

1.1.1 What is the Biomechanics?

The biological world is a part of the physical world around us and naturally is an object of inquiry in mechanics; so, we can say that the biomechanics is mechanics applied to biology, to the living system.

The biomechanics allows us to understand the normal function of an organism, help us to predict the alterations and propose how to intervene artificially. It is a modern subject with ancient roots and covers a vast and unexplored territory. At ancient Greece, Aristotle had already described the anatomy and the functions of the internal organs in *" On the parts of animals"*, and since that moment many scientists have dealt with this subject. It was the advent of the modern mechanics which encouraged the biomechanics through the scientists' researches. Scientists like Descartes, Euler, Helmotz and many others. Descartes was inspired by Galilei and Harvey results and published a book on the physiology. Euler wrote a text

Fig. 1.1: Leonardo da Vinci's sketch on *Anatomia Humana*.

on the propagation of pulse waves in arteries in 1775. Hermann von Helmotz can be considered one of the fathers of the biomechanics due to his discoveries on the mechanism of the eye, on the functioning of hearing and due to his many medical inventions. Nowadays, due to the contribution of many great scientists, the biomechanics has made significant progress, most of these resumed by Y.C. Fung in [2]. This was one of the first reviews on the theme, even if most of the problems are still open.

1.1.2 Contribution of Biomechanics to Medicine

It can be easily asserted that the biomechanics has participated, directly or indirectly, to almost every progress in the medical field.

Biomechanics has supported the clinic of the cardiovascular system by introducing the heart valves, pacemakers or stents; similarly, it has helped patients in the post-operative trauma and, in the problems of the respiratory system as well. Biomechanics has given a substantial contribution on the study of atherosclerosis and of blood flows, not to say about advances in orthopedics: prostheses, implantable materials, and artificial arts are common objects in every operating room by now.

Nowadays it is impossible to think about the medicine without taking into account the biomechanics, that is the bridge between the traditional problems and standards of mechanics and medicine.

1.1.3 The Computational Biomechanics

A large number of positive aspects have led the computational biomechanics to rapid growth in the last years. The possibility of making computer-assisted simulations, qualitative and quantitative, has contributed in nearly every advance in modern medicine. The computational models, in fact, allow to obtain a series of information, about the object inquired, above all when it is located in regions where it may be challenging to get experimental measurements.

The advances made in the imaging processing and geometry reconstruction fields, summed to the increasing power of the machines, have allowed reproducing more and more accurately the biological materials.

The computer simulation for physical phenomena has been used since the 1950s for traditional engineering. In the 1970s, researchers started to apply the principle of computational solid and fluid mechanics to biology, mainly using the newborn finite element method (FEM), [3, 4, 5, 6, 7, 8]. Bone, muscle, ligament present complex structures not adequately described by the traditional engineering methods and therefore, novel constitutive models were developed in the attempt to study these materials, [9, 10, 11]. Since that moment, biomechanics has been seen as an essential player on the study of the human body and now, the studies cover each human sub-apparate. From the biomechanics of the brain [12] to the determination of the skeletal fragility [13], from the musculoskeletal injuries [14] to the balloon angioplasty [15], just to cite some examples.

However, in order to convince doctors and scientists to extrapolate useful data from the model, it must be credible. A credible computational model should be governed by mathematical equations well implemented, should represent correctly the physics of the problem and should take into account a certain grade of error and uncertainty. Moreover, a good model should be combined as much as possible with experimental measurements and data. Hence, such models undergo the process of *verification and validation* (V&V) to satisfy the requirements exposed above, although many argued that ”verification and validation of numerical models of natural systems is impossible” [16].

The quality of the model lays at the base of a fundamental perspective of the computational biomechanics, the Computer-Integrated Surgery (CIS), [17]. CIS could allow overcoming some limitations of traditional surgery, by decreasing the error probability and the number of trauma [18]. A system like this depends on the ability to produce a robust and reliable model, [19], and such that can be interpreted by personnel not confident in numerical science. A crucial point of CIS is the speed: the computational model must be not only accurate but must give the response fastly (less than 40 min.) [20]. Creating robust but simple models is indeed one of the main topic of contemporary biomechanics, a wide field that involves the subject of this Ph.D. thesis.

1.2 A brief review on the Carrera Unified Formulation

The computational biomechanics, as above depicted, has to be considered within the wide context of the computational sciences, that play a fundamental role in many research fields. The computational mechanics, in fact, is a transversal science employed on the resolution of problems that, not rarely, are common to different research fields. The results shown in this thesis, are a consequence of the employment of some models previously developed for structural and aerospace engineering. In particular, the results here presented are based on the application of the *Carrera Unified Formulation* (CUF). The CUF is an advanced theory, that can be used to deal with 3D structural problems and reduce them to 2D or 1D ones in a unified manner. The capabilities of this technique have been exploited for a wide range of problems, and a brief review of the utilization of CUF in literature is here presented.

Thin-walled and reinforced structures 1D CUF models were initially introduced to analyze the isotropic and thin components by Carrera *et al.* in [21] and in [22]. In these papers, 1D Taylor series were used to express the transversal kinematics, and closed-form and finite element models were taken into account. The 1D CUF hierarchical features permit to handle various structural problems employing the same formulation since the approximation level can be imposed as an input and can be opportunely chosen through a convergence analysis. The comparison of 1D CUF models respect to 2D shell models was studied in Carrera *et al.* in [23] to investigate thin-walled structures. The absence of shear, membrane lockings, and computational efficiency are enlightened in this paper. Carrera and Petrolo presented a new family of 1D CUF models in [24]; in this work, Lagrange functions are employed to describe the orthogonal displacement field. Lagrange expansion models make use only pure displacement unknowns.

An investigation on composite materials has been carried out through 1D CUF models by Carrera and Petrolo in [25] exploiting Lagrange Expansion models. Aeronautic longerons were considered as an example of real application. The results enlighted the performances of 1D CUF models to predict 3D stress fields with a drastic reduction of DOFs than solid FEs. Further improvements of the 1D CUF were introduced in Carrera *et al.* [26, 27] by using trigonometric and zig-zag kinematics. Correct displacement/strain/stress responses were provided for slender and short structures. During last years, CUF has extensively enlarged its range of applicability for analysis of composited structures: Pagani *et al.* proposed the Legendre expansion functions in [28], and the higher-order theories have been introduced for the mechanics of structure genome in [29]. The mapping scheme was used by Carrera *et al.* [30] in a component-wise approach for laminated structures and static analysis of sandwich beam structures were investigated by De Pietro *et al.* [31]. Recently, fiber-reinforced failure behavior has been investigated through one-dimensional higher-order models by Kaleel *et al.* in [32, 33].

1D CUF has been extended to the free vibration analysis of isotropic structures by Carrera *et al.* in [34] via the finite element method (FEM). Particular modes as those characterized by severe distortions could be detected by 1D models with at least ten times fewer DOFs than shells. Similar results have been found for buckling by Giunta *et al.* in [35] and for sandwich beam structures by Hui *et al.* [36].

Functionally graded material (FGM) structures have been analyzed through closed-form (Giunta *et al.*, [37, 38]) and finite element method ([39]) solutions. Dynamic and static analyses have been taken into account for compact and thin-walled structures. In these works, 1D CUF predicts the complete 3D-like behavior, based on the opportune expansion order. Additionally, a thermal stress analysis of FGM has been conducted by De Pietro *et al.* in [40].

A mixed axiomatic/asymptotic model has recently been proposed by Carrera and Petrolo [41] and Carrera *et al.* [42] to study the influence of a single generalized displacement component in a higher-order model. In this context, the effect of each variable is evaluated by evaluating the consequence of its repression on the solution. By using this method, the ineffective variables can be found and removed to build further reduced models keeping on the same accuracy of full models, but less unknown variables.

Refined models were firstly employed for aeroelastic problems by Carrera *et al.* ([43]) and Varello *et al.* [44]. The Vortex Lattice Method (VLM) was used together with 1D CUF to analyze the static aeroelastic behavior of surfaces. 1D CUF demonstrated to manage the typical aeroelastic bending-torsion solicitations, with low computational exertion. Varello *et al.* [45] improved the 1D CUF aeroelastic formulation by using a 3D panel aerodynamic technique. Generally speaking, higher-order 1D models are of great interest for aeroelastic problems in which fast and highly accurate analysis are needed. Unsteady aeroelasticity for the analysis of flutter has been conducted by Pagani *et al.* [46] and Petrolo [47, 48] via the Doublet Lattice Method (DLM). Carrera and Zappino [49] and Carrera *et al.* [26] have used CUF-LE models, to predict the supersonic panel flutter of thermal insulation panels for space applications. Punctual, particular boundary conditions were taken into account and 1D CUF proved to be a reliable method to handle the 2D structures.

Rotors and rotating blades 1D CUF models were improved for rotor dynamics tests in Carrera and Filippi [50] and Carrera *et al.* [51]. Compact rotating structures accounted for Coriolis and centrifugal effects in free vibration analyses. Exact frequencies and modal shapes, involving shell-like effect, were captured. The efficiency of 1D CUF models has been tested for metallic/composite rotors in [52, 53] while results coming from the free-vibration analysis of composite blades can be found in [54].

Varello and Carrera in [55] have introduced 1D CUF to biomechanics applications. In particular, the atherosclerotic plaque pathology was initially employed as a typical biostructure with complex geometries and was analyzed for homogeneous and nonhomogeneous material cases, using 1D Taylor models. Carrera *et al.* has forwarded this work in [56], in which static and free-vibration analysis of biostructures such as arteries and dental prosthesis have been investigated. Comparisons with full solid FEs models enlighted the extraordinary three-dimensional efficiency in the investigation of even short and multi-material structures with arbitrary geometry, offering an important reduction in computational costs.

1D CUF has been developed also for multi-field analysis. Thermomechanical analyses were conducted by Giunta *et al.* [57, 57] through closed-form solutions and via the radial basis functions. The temperature field was obtained by employing the Fourier heat conduction formula and then used as an external load in the mechanical analysis. Hygrothermal effects have been investigated for composite laminates by Cinefra *et al.* in [58]. Piezo-electric issues have been investigated by Giunta *et al.* [59]. The displacement and the electric potential were described above the transversal section through Lagrange functions in a layer-wise sense. Recently, piezo-ceramic actuators for high-temperature applications have been analyzed by Zappino *et al.* in [60].

Structural modeling often requires higher-order capabilities in a limited part of the domain due to local changes on geometries or boundary conditions. The development of methods allowing to couple lower- and higher-order models alongside the same structure, has recently been introduced. Biscani *et al.* in [61] used the

Arlequin method to put together different 1D models along the axis of the beam. Close results have been obtained by Carrera *et al.* [62]through the use of Lagrange multipliers. Higher-order models, based on the variation of the kinematics along the cross-section, were employed to study thin-walled and composite structures. In this context, the *node-dependent kinematic approach* was introduced in the CUF framework by Zappino *et al.* in [63]. Through this novel technique, it is possible to change the family and the order of the approximation node-by-node along the finite element obtaining a further reduction in terms of computational costs. This feature allowed CUF to extend its capabilities: node-dependent kinematic models were used for analysis of beam with piezo-patches [64], as well as for global-local analyses of laminated structures [65] and rotating structures [66], among the others.

In Carrera *et al.* [67] it is presented the analysis of free-vibration of wings. Particularly, box wings were accounted for and the tests underlined the properties of this method to handle the shell-like response of thin bodies. The Component-Wise approach (CW) has been recently implemented alongside the 1D CUF. In this approach, the various component of the structure are designed via 1D CUF models. The employment of Lagrange elements makes the union of these components easy, due to the imposition of the continuity at the interface. Additionally, also 3D components can be described via 1D models, thanks to the enrichment of the kinematics. The CW has been exploited by Carrera *et al.* [68, 69] to perform the different analysis of a number of aerospace components. The results were compared to solid 3D models and results coming from literature, highlighting very much precision and high computational capability. The component-wise approach has been used also to perform a multiscale analysis. In particular, CW can be employed to express the different scale parts - matrices, layers, and fibers - by only considering their material characteristics without any coupling formulations. In general, no homogenization is required for the different materials and, indeed, the multi-scale models can be easily assembled. Microscale level higher-order models are used uniquely where needed, i.e., when failure can happen, whereas macroscale models can be employed elsewhere. The CW has been employed also in Carrera *et al.* [70], to predict the behavior of composite structures.

1.2.1 One-dimensional models for Fluid-Dynamics

One-dimensional models in fluid-dynamics have attracted the interest of many researchers working in fluid-dynamics modeling, although the fundamental 3D nature of the phenomena considered. Many engineering applications have a characteristic dimension which makes the problem nearly as one-dimensional. In example, a river beds as well as vessels, present a predominant direction for a river or a blood flow, as suggested by [71] and [72]. Taking into account the computational hemodynamics, probably the first one-dimensional model belongs to [73], who derived the partial differential equations (PDEs) for mass and momentum conservations. From the mathematical point of view, this theory was later formalized by the Navier-Stokes set of equations. This still represents a fundamental basis for fluids applications. More recently, the circulatory system was largely investigated by Fung in [74].

The derivation of a flow model from 3D to 1D is a challenging task, and probably, it could include strong simplifications due to the presence of vortex, boundary conditions, and other issues. However, 1D models of flows can be useful for a better understanding of entire networks, and in terms of computational effort. With this aim, FEM and spectral methods have been coupled by Perotto *et al.* [75]. Formaggia *et al.* [76] formulated a one-dimensional model of incompressible fluids using the cross-sectional integration of the Navier-Stokes equations orthogonally to the axial direction. On the other hand, the proper orthogonal decomposition (POD) based on isogeometric analyses was presented by Salmoiraghi *et al.* [77]. In a like manner, Smith *et al.*. [78] proposed the integration of axial velocity of the blood flow within a finite difference model, whereas the use of spectral/hp element spatial discretization was introduced by Sherewin *et al.* [79], for a 1D study of a vascular system. In Ref.[80], a class of 1D nonlinear systems for the propagation of blood pulsation in compliant arteries was analyzed. Another ramification of research is related to the real-time solutions and active control of the PDEs in the case of complex fluids. The employment of CFD reduced models in this context has been analyzed by Ravindran *et al.* [81] and by Quarteroni *et al.* [82]. The quality of this one-dimensional approach is improved by the possibility to be coupled with more refined models (i.e., 2D and 3D) in some limited parts of the domain, as proposed by Perotto *et al.* [83] and by Formaggia *et al.* [76].

The fluid-dynamic formulation presented in this work moves from the results achieved by Varello *et al.*, [84, 85], and Pagani, [86]. In these works, the framework of the Carrera Unified Formulation has been extended to fluid-dynamic problems, by coupling a finite element model of the Navier-Stokes equations to the cross-sectional expansion functions. In this thesis will be exposed this preliminary results, and the extension of the formulation to the node-dependent kinematic will be presented. The results provided demonstrate how the 1D models may be of interest in various application as blood flows in compliant vessels.

Chapter 2

Carrera Unified Formulation for Structural Mechanics

The fundamental assumptions that limit the range of applicability of the classical one-dimensional theories, such as the Euler-Bernoulli beam theory (EBBT), or the Timoshenko beam theory (TBT), have been overcome over time by introducing more refined models. Due to these improvements, it has been possible to detect the 3D-like effects and local phenomena of a structure without to resort to solid models. In this chapter a unified approach is presented, able to recollect and enhance the higher-order theories, in a compact manner; through the Carrera Unified Formulation, in fact, the higher-order theories can be derived hierarchically. According to CUF, the kinematics is postulated as an arbitrary expansion of the generalized unknowns and, through the Principle of Virtual Displacement, the governing equations are expressed in terms of fundamental nuclei of finite element arrays. This chapter shows in detail the concepts exposed above and, in the end, it presents the extension to nonlinear problems.

2.1 Refined one-dimensional models

2.1.1 Preliminaries

Let consider the Fig. 2.1, with the sketch of a generic beam structure. The cross-section of the beam lies on the xz-plane and it is denoted by Ω, whereas the boundaries over y are $0 \leq y \leq L$.

Let us introduce the transposed displacement vector,

$$\mathbf{u}(x, y, z; t) = \left\{ \begin{array}{ccc} u_x & u_y & u_z \end{array} \right\}^T \tag{2.1}$$

The time variable (t) will be omitted in the remaining part of the chapter for sake of clarity. The stress, $\boldsymbol{\sigma}$, and strain, $\boldsymbol{\epsilon}$, components are expressed in transposed

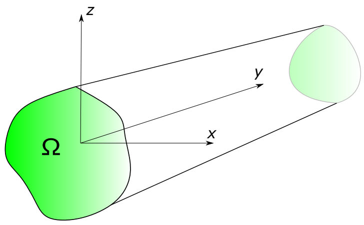

FIG. 2.1: Generic beam structure and system of reference

forms as follows:

$$\boldsymbol{\sigma} = \left\{ \begin{array}{cccccc} \sigma_{yy} & \sigma_{xx} & \sigma_{zz} & \sigma_{xz} & \sigma_{yz} & \sigma_{xy} \end{array} \right\}^T$$
$$\boldsymbol{\epsilon} = \left\{ \begin{array}{cccccc} \epsilon_{yy} & \epsilon_{xx} & \epsilon_{zz} & \epsilon_{xz} & \epsilon_{yz} & \epsilon_{xy} \end{array} \right\}^T \tag{2.2}$$

When the displacements considered are small compared to a characteristic dimension in the plane Ω, the strain-displacement relations are

$$\boldsymbol{\epsilon} = \mathbf{D}\mathbf{u} \tag{2.3}$$

where $\mathbf{D}$ is the linear differential operator matrix, as follows

$$\mathbf{D} = \begin{bmatrix} 0 & \frac{\partial}{\partial y} & 0 \\ \frac{\partial}{\partial x} & 0 & 0 \\ 0 & 0 & \frac{\partial}{\partial z} \\ \frac{\partial}{\partial z} & 0 & \frac{\partial}{\partial x} \\ 0 & \frac{\partial}{\partial z} & \frac{\partial}{\partial y} \\ \frac{\partial}{\partial y} & \frac{\partial}{\partial x} & 0 \end{bmatrix} \tag{2.4}$$

Constitutive laws are now exploited to obtain stress components to give

$$\boldsymbol{\sigma} = \tilde{\mathbf{C}}\boldsymbol{\epsilon} \tag{2.5}$$

The coefficients $\tilde{C}_{ij}$ depend on Young and Poisson moduli in case of isotropic materials. The explicit formulation of the coefficients $\tilde{C}_{ij}$ are not noticed here, but they can be found in classical bokks, see for example Tsai [87] and Reddy [88]. As reported in [89], all the coefficients of the matrix $\tilde{\mathbf{C}}$ are non-zero in presence of anisotropic materials. Furthermore, in case of models with constant and linear distributions of the in-plane displacement components, u_x and u_z, the materials coefficients should be modified in order to overcome the Poisson locking, see [90].

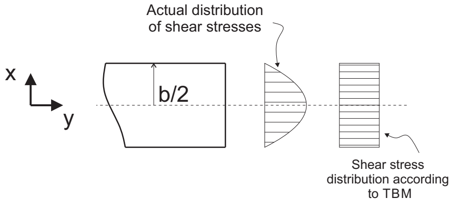

FIG. 2.2: Homogeneous condition of transverse stress components at the unloaded edges of the beam

2.1.2 Refined beam models

The one-dimensional models move from the Euler-Bernoulli beam theory (EBBT), which considers the displacements in the $yz-plane$ and imposes the orthogonality of the section respect to the beam axis. The Timoshenko beam theory (TBT) allows the section not to be perpendicular it takes into account only a homogeneous distribution of the shear stress over the beam cross-section. In order to obtain a parabolic distribution of the shear stress as in Fig. 2.2, one should consider the Reddy-Vlasov beam theory in which it is possible to impose null shear stress at the top/bottom of the section, [91]. No one of these methods accounts for torsional kinematics but one can add a term for the rigid rotation with ease.

By adding these contributions to the kinematic field of the displacements, one can solve a number of macro-structural problems but the detection of *higher-order* phenomena could be hard to accomplish. Many different refined beam models have been proposed over the last century, even one can say that, as a general statement, that the richer the kinematic field, the most accurate the 1D model becomes, [92].

Taylor Expansion Due to the tipical large difference between the dimension belonging to the transversal plane and those related to the beam axis, the variation of the unknowns lying on the first one (ω) can be approximated. According to the Carrera Unified Formulation (CUF), the kinematics of any order beam theories can be adequately expressed by a hierarchical expansions of the generalized unknowns $\mathbf{u}_\tau$, defined along the 1D domain; i.e.,

$$\mathbf{u}(x,y,z;t) = F_\tau(x,z)\mathbf{u}_\tau(y;t), \qquad \tau = 1,2,\cdots,M \tag{2.6}$$

In Eq. 2.6, F_τ represents the interpolation functions over ω and M is the number of the expansion terms employed in the description of the displacement field. In the notation proposed, τ denotes summation. Figure 2.3 shows a sketch a TE element.

The choice of the functions F_τ and the number M determines the class and order of the beam theory adopted and therefore, the accuracy of the approximation. Over the last years, several interpolation functions have been implemented within the CUF-based one-dimensional models, such as Taylor Expansions (TE), Lagrange Expansions (LE), Hierarchical Legendre Expansions (HLE), and any combinations of these in a mixed-kinematics sense. A short dissertation on TE and LE, since have been largely adopted in this thesis, are given hereinafter for clarity reasons.

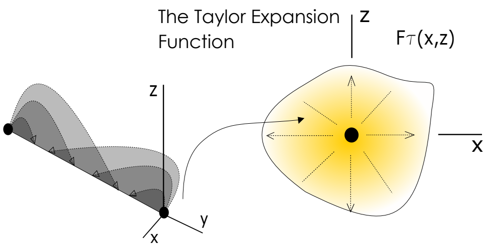

FIG. 2.3: The Taylor Expansion model

N	M	F_τ
0	1	$F_1 = 1$
1	3	$F_2 = x$ $F_3 = z$
2	6	$F_4 = x^2$ $F_5 = xz$ $F_6 = z^2$
3	10	$F_7 = x^3$ $F_8 = x^2 z$ $F_9 = xz^2$ $F_{10} = z^3$
⋮	⋮	⋮
N	$\frac{(N+1)(N+2)}{2}$	$F_{(N^2+N+2)/2} = x^N$ $F_{(N^2+N+4)/2} = x^{N-1}$ $\ldots$ $F_{N(N+3)/2} = xz^{N-1}$ $F_{(N+1)(N+2)/2} = z^N$

TABLE 2.1: MacLaurin's polynomials

The McLaurin series polynomials $x^i z^j$ are employed as F_τ cross-sectional functions in the case of TE models, where i and j positive integers. Table 2.1 shows M and F_τ as functions of the expansion order, N, which represents the maximum order of the polynomials used in the expansion. As an example, the second-order ($N = 2$) TE beam model appears as follows:

$$\begin{aligned} u_x(x,y,z) &= u_{x_1}(y) + x\ u_{x_2}(y) + z\ u_{x_3}(y) + x^2\ u_{x_4}(y) + xz\ u_{x_5}(y) + z^2\ u_{x_6}(y) \\ u_y(x,y,z) &= u_{y_1}(y) + x\ u_{y_2}(y) + z\ u_{y_3}(y) + x^2\ u_{y_4}(y) + xz\ u_{y_5}(y) + z^2\ u_{y_6}(y) \\ u_z(x,y,z) &= u_{z_1}(y) + x\ u_{z_2}(y) + z\ u_{z_3}(y) + x^2\ u_{z_4}(y) + xz\ u_{z_5}(y) + z^2\ u_{z_6}(y) \end{aligned} \tag{2.7}$$

In this scheme, classical beam theories can be considered as particular cases of TE models. As an example, the Euler-Bernoulli and the Timoshenko beam theories, are particular cases of the linear ($N = 1$) TE model, expressed as

$$\begin{aligned} u_x &= u_{x_1} + x\ u_{x_2} + z\ u_{x_3} \\ u_y &= u_{y_1} + x\ u_{y_2} + z\ u_{y_3} \\ u_z &= u_{z_1} + x\ u_{z_2} + z\ u_{z_3} \end{aligned} \tag{2.8}$$

where the right-hand parameters (u_{x_1}, u_{y_1}, u_{z_1}, u_{x_2}, etc.) are the displacements of the beam axis and their first derivatives. A more deep explanation about Taylor Expansion models can be found in [93], where the derivation of classical theories from the linear ($N = 1$) TE model and a number of numerical examples are also presented.

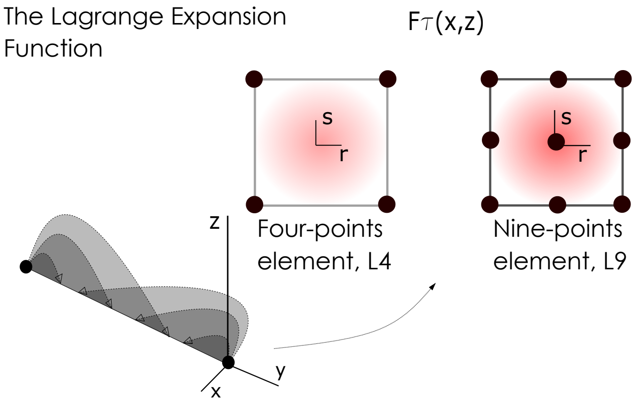

FIG. 2.4: The Lagrange Expansion model

The Lagrange Expansion In the case of more complex geometries, particular boundary conditions and non-uniform material structures, the use of TE should be inadequate. LE models adopt the Lagrange polynomials functions as F_τ local the displacement variables over the cross-sectional domain, in a isoparametric logic. In the context of LE, beam theories with different orders can be implemented depending on the choice of the Lagrange polynomials set employed to describe the cross-sectional displacements. In fact, linear L3, bi-linear L4, or quadratic L9 beam theories can be implemented with ease by using CUF, see Fig. 2.4. As an example, the LE quadratic beam model holds the following kinematics:

$$\begin{aligned} u_x(x,y,z) &= F_1\, u_{x_1}(y) + F_2\, u_{x_2}(y) + F_3\, u_{x_3}(y) + \cdots + F_9\, u_{x_9}(y) \\ u_y(x,y,z) &= F_1\, u_{y_1}(y) + F_2\, u_{y_2}(y) + F_3\, u_{y_3}(y) + \cdots + F_9\, u_{y_9}(y) \\ u_z(x,y,z) &= F_1\, u_{z_1}(y) + F_2\, u_{z_2}(y) + F_3\, u_{z_3}(y) + \cdots + F_9\, u_{z_9}(y) \end{aligned} \tag{2.9}$$

where $u_{x_1}, u_{x_2} \cdots, u_{z_9}$ are the pure translational displacements, as the primary unknowns of the problem. In this case, $F_1, \cdots, F_9$ are the following quadratic Lagrange polynomials:

$$\begin{aligned} F_\tau &= \tfrac{1}{4}(r^2 + r\, r_\tau)(s^2 + s\, s_\tau), \qquad \tau = 1,3,5,7 \\ F_\tau &= \tfrac{1}{2}s_\tau^2(s^2 + s\, s_\tau)(1 - r^2) + \tfrac{1}{2}r_\tau^2(r^2 + r\, r_\tau)(1 - s^2), \qquad \tau = 2,4,6,8 \\ F_\tau &= (1 - r^2)(1 - s^2), \qquad \tau = 9 \end{aligned} \tag{2.10}$$

where r and s are reffered to the natural system of reference between -1 and $+1$, and r_τ and s_τ represent points locations of the nine-node Lagrange polynomial entity. Insights on LE models are in the original work by Carrera and Petrolo [94] and in [95]. In this thesis, LE models are exploited to build component-wise models of complex structures as described in Section 2.1.3, where more details about LE are exposed.

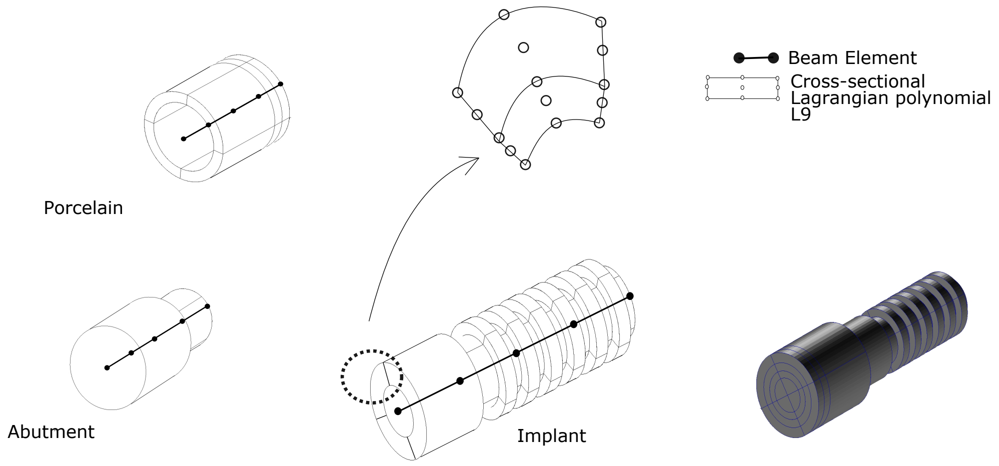

Fig. 2.5: Component-Wise approach applied to dental prosthesis.

2.1.3 The Component-Wise approach

Usually, the analysis of multi-component structures could be very challenging. These kind of structures infact, present a range of different components, which are often characterized by different scales and materials hard to handle in a single model. In the biomedical context, for example, bones, organs, arteries as well as the brain are just few examples of multi-component systems. Generally, the multi-component structures models take into account the coupling of various mathematical theories, even in finite element method framework. This ususally leads to involve artificial techniques to solve the kinematic inconsistency among, for example, 1D, 2D and 3D finite elements. This may add dicculties and uncertainties, especially in the case of adoption of higher-order models to build reduced models with low computational efforts.

In this domain, LE models, when coupled with FEM, present interesting capabilities for the analysis of multi-component structures. In other works in fact, it was demonstrated that LE-CUF models can be implemented in a *Component-Wise* (CW) sense to assembly complex structural models in an efficient and mathematical consistent manner, see Refs. [96, 97, 98, 99, 100]. Figure 2.5 presents the CW approach applied to a dental prosthesis. According to CW logic, each component of the structure (i.e., implant, abutment, porcelain, etc.), is modelled by higher-order LE beam elements. These models, approximating the kinematics of the beam by using Lagrange polynomials, make use of the physical elements in the description of the problem. In this manner, the geometries of the structure are exact, and fictitious integration domains (e.g., beam axis in the case of classical 1D finite elements) are no more used. Moreover, due to the same kinematics adopted on the modelling of the components, coupling is automatic and no artificial mathematical links (e.g. multi-point constraints) are utilized. The aforementioned capabilities of the CW technique can be achieved only using 3D finite elements models. However, adopting higher-order CUF, enhanced geometrically-consistent models with low computational costs can be formulated inherently.

2.2 Finite Element Method

In Ref. [101] are exposed the closed form analytical solutions of some typical structural engineering problems. Evidently, the exact solutions coming from *strong form* of the ODEs (or PDEs) underlying the structural mechanics problems are the optimum in terms of reliability and precision. However, the analytical solutions are only possible for a few particular cases which represent a simplified reality. Much more frequently it is necessary to resort to the *weak form* of the governing equations, which can be solved via different numerical methods.In particular, the Finite Element Method (FEM) is described in this section and the typical finite element matrices are computed according to Carrera Unified Formulation (CUF) introduced above.

The main idea of the displacement-based finite element method is to discretize the general displacement as the total nodal displacements by using of mathematical functions (also called *shape functions* N_i). In this thesis, isoparametric 1D FE are utilized to interpolate the displacement field through the nodal unknowns:

$$\mathbf{u}_\tau(y) = N_i(y)\mathbf{q}_{\tau i}, \qquad i = 1, 2, ..., N_n \tag{2.11}$$

where N_i stands for 1D shape functions and $\mathbf{q}_{\tau i}$ is the nodal displacement vector,

$$\mathbf{q}_{\tau i} = \left\{ \begin{array}{ccc} q_{u_{x_{\tau i}}} & q_{u_{y_{\tau i}}} & q_{u_{z_{\tau i}}} \end{array} \right\}^T \tag{2.12}$$

where repeated subscript i indicates summation based on Einstein s notation. Thus, summarizing, the general expression of the kinematics in the framework of CUF through the finite element method is

$$\mathbf{u}(x, y, z) = F_\tau(x, z)N_i(y)\mathbf{q}_{\tau i}, \qquad \tau = 1, 2, ..., M \quad i = 1, 2, ..., N_n \tag{2.13}$$

In this thesis 1D Lagrange shape functions are adopted and in particular, two-nodes linear $B2$, three-nodes quadratic $B3$ and four-nodes cubic $B4$ are employed to interpolate the unknown field along the $yaxis$. The first-class Lagrange polynomials based on two Lagrange points ($N_n = 2$) approximates linear displacements and the shape functions are:

$$N_1 = \tfrac{1}{2}(1 - r), \quad N_2 = \tfrac{1}{2}(1 + r), \quad \left\{ \begin{array}{l} r_1 = -1 \\ r_2 = +1 \end{array} \right. \tag{2.14}$$

where the natural coordinate, r, varies from -1 to $+1$ and r_i indicates the position of the node within the natural beam boundaries. In case of second-order

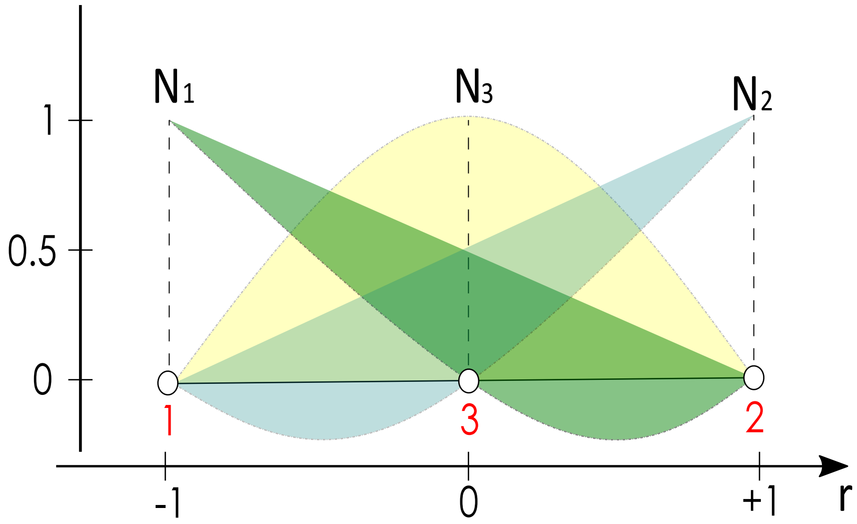

Fig. 2.6: 1D Lagrange polynomials as shape functions of B3 element

approximation ($N_n = 3$) one has:

$$N_1 = \tfrac{1}{2}r(r-1), \quad N_2 = \tfrac{1}{2}r(r+1), \quad N_3 = -(1+r)(1-r), \quad \begin{cases} r_1 = -1 \\ r_2 = +1 \\ r_3 = 0 \end{cases} \tag{2.15}$$

and the shape functions are depicted in Fig. 2.6. Finally, B4 shape functions hold

$$\begin{aligned} N_1 &= -\tfrac{9}{16}(r+\tfrac{1}{3})(r-\tfrac{1}{3})(r-1), \quad N_2 = \tfrac{9}{16}(r+\tfrac{1}{3})(r-\tfrac{1}{3})(r+1), \\ N_3 &= +\tfrac{27}{16}(r+1)(r-\tfrac{1}{3})(r-1), \quad N_4 = -\tfrac{27}{16}(r+1)(r+\tfrac{1}{3})(r-1), \end{aligned} \quad \begin{cases} r_1 = -1 \\ r_2 = +1 \\ r_3 = -\tfrac{1}{3} \\ r_4 = +\tfrac{1}{3} \end{cases} \tag{2.16}$$

For more details about 1D Lagrangian shape functions, interested readers are invited to refer to [102].

2.3 Principle of Virtual Displacements and Governing Equations

The Mimimum Potential Energy principle of classical elasticity states that the actual displacement solution $\mathbf{u}^*$ that satisfies the governing equations, is that which makes Π stationary:

$$\delta\Pi = \delta U - \delta W = 0, \qquad if\, \mathbf{u} = \mathbf{u}^* \tag{2.17}$$

where δU is the variation of the the total internal energy and δW is the variation of the external energy due to applied mechanical loads. The weak form of the Eq. 2.17 leads to the *Principle of Virtual Displacements* PVD, in which the virtual variation of the displacements are the weight function. According to the Principle of Virtual Displacements. the equilibrium of the continuum requires that for any admissible virtual displacements adducted on the body in its state of equilibrium, the internal virtual work is equal to the external virtual work, [102],

$$\delta L_{int} = \delta L_{ext} \tag{2.18}$$

where L_{int} is the internal work (also known as strain energy) and L_{ext} is the external work due to the applied loads. In addition to these terms, using the d Alembert principle, the inertia forces can be simply included as part of the body forces [102]. The contribution of virtual work of inertial loadings L_{ine} is thus taken into account in the external virtual work, and the Eq. 2.18 becomes:

$$\delta L_{int} = \delta L_{ext} = \delta L_{al} - \delta L_{ine} \tag{2.19}$$

where δL_{al} is the work of the applied loads. Each term of Eq. 2.19 participates to the governig equation of the problem according to the problem itself and to the type of analysis is required, as it will be explained in the following sections.

The FEM allow to obtain the expression of each term of the *Principle of Virtual Displacement* in elemental arrays.

In case of static analysis, the aforementioned principle states

$$\delta L_{\text{int}} = \delta L_{\text{ext}} \tag{2.20}$$

in which L_{int} is internal energy of deformation, as defined before, and L_{ext} stands for the work exercited by the external loadings. In the Finite Element Method, the virtual variation of the internal work is

$$\delta L_{\text{int}} = \delta \mathbf{q}^T \mathbf{K} \mathbf{q} \tag{2.21}$$

where $\mathbf{q}$ is the global vector containing the generalized nodal unknowns and $\mathbf{K}$ is the assembled global stiffness matrix. On the other hand, the virtual variation of the external work is

$$\delta L_{\text{ext}} = \delta \mathbf{q}^T \mathbf{P} \tag{2.22}$$

where $\mathbf{P}$ is the vector of the generalized nodal forces. By substituting Eqs. 2.22 and 2.21 into Eq. 2.20, the final algebraic system of equations is obtained

$$\mathbf{K}\mathbf{q} = \mathbf{P} \tag{2.23}$$

The Free-vibration analysis studies the equality between inertial and elastic forces. In this cases, the PVD is written as

$$\delta L_{\text{int}} = -\delta L_{\text{ine}} \tag{2.24}$$

According the FEM formulation, the virtual variation of inertial forces appears in the following form:

$$\delta L_{\mathrm{ine}} = \delta \mathbf{q}^T \mathbf{M} \ddot{\mathbf{q}} \tag{2.25}$$

where $\mathbf{M}$ is the global mass matrix and $\ddot{\mathbf{q}}$ are the nodal acceleration generalized. Introducing Eqs. 2.22 and 2.25 into Eq. 2.24, the equations of equilibrium become

$$\mathbf{K}\mathbf{q} + \mathbf{M}\ddot{\mathbf{q}} = 0 \tag{2.26}$$

Considering the solution $\mathbf{q}$ to be a harmonic with amplitude $\mathbf{Q}$ and angular frequency ω, Eq. 2.26 leads to classical eigenvalue problem

$$\left(\mathbf{K} - \omega^2 \mathbf{M}\right) \mathbf{Q} \mathrm{e}^{\mathrm{i}\omega t} = 0 \tag{2.27}$$

2.4 Matrices

The previous paragraphs have introduced the *stiffness matrix* $\mathbf{K}$, the *mass matrix* $\mathbf{M}$, and the *load vector* $\mathbf{P}$ on the basis of the Principle of Virtual Displacements and the finite element method. The expressions of the components of these nuclei are here explicitly computed for isotropic materials and then the procedure to build the finite element matrices and vectors is addressed.

For the clarity reasons, the virtual variation of the strain energy is reported here

$$\delta L_{\mathrm{int}} = \int_V \delta \boldsymbol{\epsilon}^T \boldsymbol{\sigma} \, \mathrm{d}V \tag{2.28}$$

The fundamental nucleus of the elemental structural stiffness matrix of the 1D CUF FE model is derived Substituting the constitutive laws (Eq. 2.5), the kinematic assumptions of Eq. 2.13 and the geometrical relations (Eq. 2.3), into Eq. 2.28, the fundamental nucleus of the stiffness matrix of the structural element can be obtained. One has

$$\delta L_{\mathrm{int}} = \delta \mathbf{q}_{\tau i}^T \mathbf{K}^{\tau s i j} \mathbf{q}_{s j} \tag{2.29}$$

However, the 3×3 fundamental nucleus of the stiffness matrix and its components are given here and they are referred to as $K_{(rc)}^{\tau s i j}$, where r is the row number

$(r = 1, 2, 3)$ and c is the column number $(c = 1, 2, 3)$.

$$
\begin{aligned}
K^{\tau sij}_{(11)} &= \left(E^{22}_{\tau_{,x}s_{,x}} + E^{44}_{\tau_{,z}s_{,z}}\right) J_{ij} + E^{26}_{\tau_{,x}s} J_{ij_{,y}} + E^{26}_{\tau s_{,x}} J_{i_{,y}j} + E^{66}_{\tau s} J_{i_{,y}j_{,y}} \\
K^{\tau sij}_{(12)} &= \left(E^{26}_{\tau_{,x}s_{,x}} + E^{45}_{\tau_{,z}s_{,z}}\right) J_{ij} + E^{23}_{\tau_{,x}s} J_{ij_{,y}} + E^{66}_{\tau s_{,x}} J_{i_{,y}j} + E^{36}_{\tau s} J_{i_{,y}j_{,y}} \\
K^{\tau sij}_{(13)} &= \left(E^{12}_{\tau_{,x}s_{,z}} + E^{44}_{\tau_{,z}s_{,x}}\right) J_{ij} + E^{45}_{\tau_{,z}s} J_{ij_{,y}} + E^{16}_{\tau s_{,z}} J_{i_{,y}j} \\
K^{\tau sij}_{(21)} &= \left(E^{26}_{\tau_{,x}s_{,x}} + E^{45}_{\tau_{,z}s_{,z}}\right) J_{ij} + E^{66}_{\tau_{,x}s} J_{ij_{,y}} + E^{23}_{\tau s_{,x}} J_{i_{,y}j} + E^{36}_{\tau s} J_{i_{,y}j_{,y}} \\
K^{\tau sij}_{(22)} &= \left(E^{66}_{\tau_{,x}s_{,x}} + E^{55}_{\tau_{,z}s_{,z}}\right) J_{ij} + E^{36}_{\tau_{,x}s} J_{ij_{,y}} + E^{36}_{\tau s_{,x}} J_{i_{,y}j} + E^{33}_{\tau s} J_{i_{,y}j_{,y}} \qquad (2.30) \\
K^{\tau sij}_{(23)} &= \left(E^{16}_{\tau_{,x}s_{,z}} + E^{45}_{\tau_{,z}s_{,x}}\right) J_{ij} + E^{55}_{\tau_{,z}s} J_{ij_{,y}} + E^{13}_{\tau s_{,z}} J_{i_{,y}j} \\
K^{\tau sij}_{(31)} &= \left(E^{44}_{\tau_{,x}s_{,z}} + E^{12}_{\tau_{,z}s_{,x}}\right) J_{ij} + E^{16}_{\tau_{,z}s} J_{ij_{,y}} + E^{45}_{\tau s_{,z}} J_{i_{,y}j} \\
K^{\tau sij}_{(32)} &= \left(E^{45}_{\tau_{,x}s_{,z}} + E^{16}_{\tau_{,z}s_{,x}}\right) J_{ij} + E^{13}_{\tau_{,z}s} J_{ij_{,y}} + E^{55}_{\tau s_{,z}} J_{i_{,y}j} \\
K^{\tau sij}_{(33)} &= \left(E^{44}_{\tau_{,x}s_{,x}} + E^{11}_{\tau_{,z}s_{,z}}\right) J_{ij} + E^{45}_{\tau_{,x}s} J_{ij_{,y}} + E^{45}_{\tau s_{,x}} J_{i_{,i}j} + E^{55}_{\tau s} J_{i_{,y}j_{,y}}
\end{aligned}
$$

where the generic term $E^{\alpha\beta}_{\tau_{,\theta}s_{,\zeta}}$ is a cross-sectional parameter related to the interpolation functions and material properties, whereas

$$
\begin{aligned}
J_{ij} &= \int_L N_i(y)\, N_j(y)\, \mathrm{d}y, & J_{i_{,y}j} &= \int_L N_{i_{,y}}(y)\, N_j(y)\, \mathrm{d}y \\
J_{ij_{,y}} &= \int_L N_i(y)\, N_{j_{,y}}(y)\, \mathrm{d}y, & J_{i_{,y}j_{,y}} &= \int_L N_{i_{,y}}(y)\, N_{j_{,y}}(y)\, \mathrm{d}y
\end{aligned}
\qquad (2.31)
$$

are the integrals of the product of shapes functions and related derivatives along the beam axis. These integrals are computed by using Gauss quadrature integration [103].

The fundamental nuclei in FEM are independent on the order of expansion and on the family of F_τ functions adopted. Thus, through the use of only few coding stetements, it is possible to implement from lower to higher-order theories. The assembly procedure of the global stiffness matrix in fact, is easily made by using four indexes τ, s, i, and j, which are opportunely reported into loop cycles in the coding statements. The construction of the singol elementa stiffness matrix is sketched in Fig. 2.7, whereas the Fig. 2.8 shows the assembly of the global arrays from the element matrices, common in all FEM schemes. At the end of the global matrix assembly, boundary conditions are imposed via the penalty method.

Accounting for the inertial works, their virtual variation can be expressed as

$$
\delta L_{\text{ine}} = \int_V \delta \mathbf{u}^T \rho\, \ddot{\mathbf{u}}_s\, \mathrm{d}V \qquad (2.32)
$$

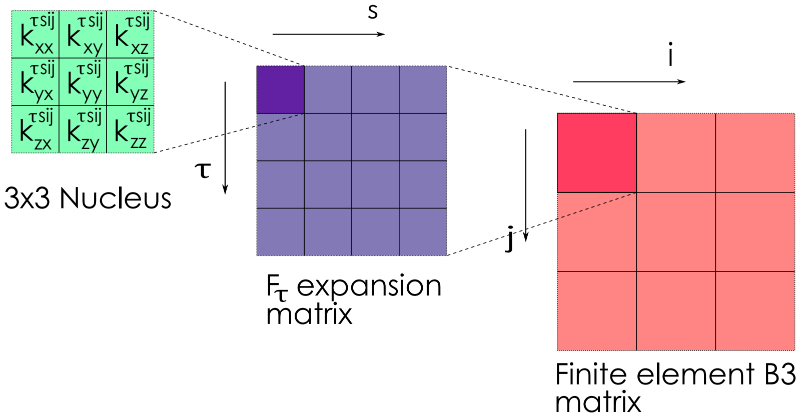
$K_{xx}^{\tau sij}$ $K_{xy}^{\tau sij}$ $K_{xz}^{\tau sij}$
$K_{yx}^{\tau sij}$ $K_{yy}^{\tau sij}$ $K_{yz}^{\tau sij}$
$K_{zx}^{\tau sij}$ $K_{zy}^{\tau sij}$ $K_{zz}^{\tau sij}$
3x3 Nucleus
s
τ
F_τ expansion matrix
i
j
Finite element B3 matrix

FIG. 2.7: Derivation of the element stiffness matrix from the fundamental nucleus. Example procedure for a B3 element and L4 Lagrange expansion function.

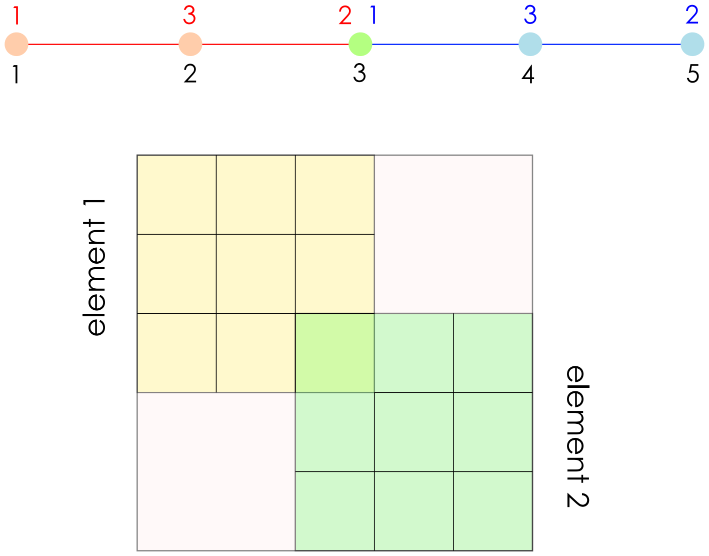
1
3
2
1
3
2
1
2
3
4
5
element 1
element 2

FIG. 2.8: Classical FEM assembly procedure of two B3 element matrices

Recalling the CUF-FE description of the displacement field (Eq. 2.13), it is possible to state that

$$\delta L_{\text{ine}} = \delta \mathbf{q}_{\tau i}^T \left(\int_L N_i N_j \, \mathrm{d}y \int_\Omega \rho F_\tau F_s \, \mathrm{d}\Omega \right) \ddot{\mathbf{q}}_{sj} = \delta \mathbf{q}_{\tau i}^T \big(E_{\tau s}^\rho J_{ij} \mathbf{I} \big) \ddot{\mathbf{q}}_{sj} \tag{2.33}$$

where $\mathbf{I}$ is a 3×3 identity matrix and $E_{\tau s}^\rho$ is the terms which take into account the expansions functions and the material density. The terms into brackets in Eq. 2.33

are the fundamental nucleus of the FE mass matrix $\mathbf{M}^{\tau sij}$.

$$\mathbf{M}^{\tau sij} = E^{\rho}_{\tau s} J_{ij} \mathbf{I} \tag{2.34}$$

The assembly of the global mass matrix is absolutely similar to the stiffness one described in the previous section.

In the case of a generic concentrated load $\mathbf{F}$ acting on the application point (x_p, y_p, z_p), the loadings vector can be derived as follows

$$\mathbf{F} = \left\{ \begin{array}{ccc} F_x & F_y & F_z \end{array} \right\}^T \tag{2.35}$$

Line and surface loads as well as other loadings, can be handled analogously. The virtual work due to $\mathbf{F}$ is

$$\delta L_{\text{ext}} = \delta \mathbf{u}^T \mathbf{F} \tag{2.36}$$

Due to Eq. 2.13, Eq. 2.36 becomes

$$\delta L_{\text{ext}} = \delta \mathbf{q}^T_{\tau i} F_\tau N_i \mathbf{F} = \delta \mathbf{q}^T_{\tau i} \mathbf{P}^{\tau i} \tag{2.37}$$

in which F_τ and N_i are computed in (x_p, z_p) and y_p, respectively. The last equation is related to the localization of the nucleus terms to load.

In the framework of CUF models, the loadings generated by the generic accelerations which take into account the 3D effect of the inertial loads, is described here. Let the accelerations vector considered:

$$\ddot{\mathbf{u}}_0(x, y, z) = \left\{ \begin{array}{ccc} \ddot{u}_{x_0} & \ddot{u}_{y_0} & \ddot{u}_{z_0} \end{array} \right\}^T \tag{2.38}$$

The virtual variation of the external work, δL_{ext}, due to the acceleration field $\ddot{\mathbf{u}}_0$ is provided by:

$$\delta L_{\text{ext}} = \int_V \delta \mathbf{u}^T \rho \, \ddot{\mathbf{u}}_0 \, \mathrm{d}V \tag{2.39}$$

Equation 2.13 is substituted into Eq. 2.39. It is:

$$\delta L_{\text{ext}} = \delta \mathbf{q}^T_{\tau i} \left(\int_L N_i N_j \, \mathrm{d}y \int_\Omega \rho F_\tau F_s \, \mathrm{d}\Omega \right) \ddot{\mathbf{q}}_{sj_0} \tag{2.40}$$

with the term between square brackets is the FN of the mass matrix $\mathbf{M}^{\tau sij}$. The virtual variation of the external work is therefore written as

$$\delta L_{\text{ext}} = \delta \mathbf{q}^T_{\tau i} \, \mathbf{M}^{\tau sij} \, \ddot{\mathbf{q}}_{sj_0} = \delta \mathbf{q}^T_{\tau i} \mathbf{P}^{\tau i}_{\text{ine}} \tag{2.41}$$

where $\mathbf{P}^{i\tau}_{\text{ine}}$ is the nucleus of the loading vector due to the given acceleration field.

2.5 FEM for Nonlinear Problems

The algenraic equilibrium equation obtained via FEM is in case of linear static analysis

$$\mathbf{Kq} = \mathbf{P} \tag{2.42}$$

This relation is linear until loading and displacement are proportional each other. Wheter they don't, the problem can be defined as *nonlinear*. The problem is nonlinear when:

- the elasticity matrix depends on the level of deformation, *physical nonlinearity*
- the relation between deformation and displacements depends on the amount of these last, *geometrical nonlinearity*
- the boundaries change during the application of the load, as in case of surfaces contact, *boundary nonlinearity*

In these cases, the Eq. 2.42 becomes

$$\mathbf{K(q)q} = \mathbf{P} \tag{2.43}$$

in which the structural stiffness matrix changes along the deformation. To face this situation, it is not possible to solve the system of equations directly, but rather, it is neccessary to resort to incremental and iterative schemes.

2.5.1 The Newton-Raphson Method

In the most simple case of one-dimensional problem, one can define the tangent to the load-displacement curve as follows:

$$\frac{\partial P}{\partial q} = \frac{\partial}{\partial q} K(q)q = (\frac{\partial}{\partial q} K(q))q + K(q) \tag{2.44}$$

and the right-hand side is defined as *tangent stiffness matrix* $\mathbf{K_T}$, and, in the case of material nonlinearities with small strain assumption, it corresponds to the material tangent matrix. The Newton-Raphson method is an iterative procedure used to detect the displacement field through the update of the tangent stiffness matrix. According to the Fig. 2.9, $K_{t,1}$ is the tangent matrix of the initial condition, and it is possible to compute the value of the displacement u_2 at the end of first iteration, assuming such matrix as constant,

$$u_2 = u_1 + \frac{p_1 - p}{K_{t,1}} \tag{2.45}$$

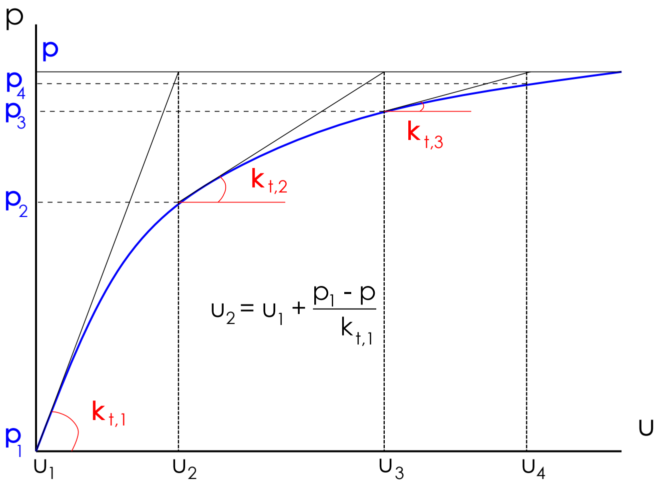

FIG. 2.9: Load-displacemnt: application of the NR method for 1-DOF system

At this value of displacement, the resultant of the forces equilibrating the system is not p, but only the reaction of the stucture at that level of deformation, p_2. It means that the applied loads are not equilibrated by the internal forces of the structure. The scheme approach the exact solution when the internal forces balance the applied load, $p_i - p \leq e$, where e is a tolerance value. Until this value is not accomplished, it needs to repeat the iterations. At each iteration the tangent stiffness matrix is updated and it could be very time consuming. This problem can be avoided by the *modified* Newton-Raphson method, which uses for all the iterations the initial value of the tangent matrix. In this case the convergence needs a larger number of cicles, but it is possible to save time by avoiding the inversion of the matrix at each iteration. The iterative N-R method is often coupled to a load-controlled scheme. In this cases, the external load is applied stepwise and and the equilibrium condition is accomplished step-by-step.

2.5.2 The Nonlinear Plasticity

In this thesis, the von Mises fialure criterion has been taken into account for materials with elasto-plastic behavior. The von Mises theory states that the material yields when the J_2 deviatoric stress achieves a threshold value. In case of isotropic hardening, this condition is described by the following equation

$$f = q(\boldsymbol{\sigma}) - \sigma_y(\bar{\epsilon}_p) \tag{2.46}$$

with

$$q(\boldsymbol{\sigma}) = \sqrt{-3J_2} = \sqrt{\frac{1}{2}\left[(\sigma_{xx}-\sigma_{yy})^2 + (\sigma_{yy}-\sigma_{zz})^2 + (\sigma_{zz}-\sigma_{xx})^2 + 6(\sigma_{xy}^2+\sigma_{xz}^2+\sigma_{yz}^2)\right]} \tag{2.47}$$

in which f is the von Mises yield function, $q(\boldsymbol{\sigma})$ is the von Mises stress, σ_y is the elastic stress limit, J_2 is the second invariant of deviatoric stress and $\bar{\epsilon}_p$ is a parameter linked to the hardening rule. The Prandtl-Reuss equation is considered for the flow rule, and the flow vector holds:

$$\mathbf{N} = \frac{\partial f}{\partial \boldsymbol{\sigma}} = \sqrt{\frac{3}{2}}\frac{\mathbf{s}}{||\mathbf{s}||} \tag{2.48}$$

where $\mathbf{s}$ is the tensor of deviatoric stress. In this context, only isotropic hardening is considered. The hardening is a physical aspect of plastic failure which links the yielding point to the history of plastic deformations. The formulation considers the yield stress as a function of accumulated plastic strain as given in Eq. 2.46 and is the derivation of the uniform expansion of initial yield locus. If the flow rule is taken into account, the rate evolution equation can be written as

$$\bar{\epsilon} = \sqrt{\frac{2}{3}}||\boldsymbol{\epsilon_p}|| \tag{2.49}$$

The constitutive model is implemented following the Ref. [104].

2.6 The Carrera Unified Formulation for nonlinear problems

In case of nonlinear problems, the principle of virtual displacements in Eq. 2.18 of the Section 2.3 leads to an incremental equilibrium equation. The control of the iterations is realized by the parametrization of the external load vector according to the parameter λ. The equilibrium equation can be therefore rewritten as

$$\mathbf{r}(\mathbf{u}) - \lambda_n \mathbf{p} = 0 \quad n \in [0, NT] \tag{2.50}$$

where λ is introduced step-by-step to discretize the scheme, n is the step index and NT is the total number of steps. $\mathbf{r}$ is the internal force at the equilibrium state n and $\mathbf{u}$ is the displacement vector. As stated before, the Newton-Raphson scheme is adopted to accomplish the step-wise numerical solution of the equilibrium point, see the Fig. 2.9. The Taylor polynomial series of the reaction vector consequent to the solution vector $\mathbf{u}_{n+1}^k$ is given by

$$\mathbf{r}(\mathbf{u}_{n+1}^{k+1}) = \mathbf{r}(\mathbf{u}_{n+1}^{k}) + \frac{\partial \mathbf{r}(\mathbf{u}_{n+1}^{k})}{\partial \mathbf{u}_{n+1}^{k}}(\mathbf{u}_{n+1}^{k+1} - \mathbf{u}_{n+1}^{k}) + \frac{1}{2}\frac{\partial^2 \mathbf{r}(\mathbf{u}_{n+1}^{k})}{\partial \mathbf{u}_{n+1}^{k\,2}}(\mathbf{u}_{n+1}^{k+1} - \mathbf{u}_{n+1}^{k})^2 + ... \tag{2.51}$$

where k is for the index of iteration along the load step. The NR system is based on the truncation of the Taylor series at the first term:

$$\mathbf{r}(\mathbf{u}_{n+1}^{k+1}) = \mathbf{r}(\mathbf{u}_{n+1}^{k}) + \frac{\partial \mathbf{r}(\mathbf{u}_{n+1}^{k})}{\partial \mathbf{u}_{n+1}^{k}} \Delta \mathbf{u} \qquad \Delta \mathbf{u} = \mathbf{u}_{n+1}^{k+1} - \mathbf{u}_{n+1}^{k} \tag{2.52}$$

The partial derivative of the current internal vector force with respect to the actual solution state $\mathbf{u}_{n+1}^{k}$ is termed as the tangent stiffness matrix $\mathbf{K}^T$, as in the previous section. Therefore, Eq. 2.52 can be written as

$$\mathbf{r}(\mathbf{u}_{n+1}^{k+1}) = \mathbf{r}(\mathbf{u}_{n+1}^{k}) = \mathbf{K}^T(\mathbf{u}_{n+1}^{k}) \Delta \mathbf{u} \qquad \Delta \mathbf{u} = \mathbf{u}_{n+1}^{k+1} - \mathbf{u}_{n+1}^{k} \tag{2.53}$$

As stated before, we are in the framework of small strain assumptions, and therefore the calculus of $\mathbf{K}^T$ corresponds in obtaining the material tangent matrix $\mathbf{C}^T$. The implementation of the flow rule adopted in this context is not reported here for the sake of brevity, but is given in detail in [105] and in [106]. At each iteration the stiffness tangent matrix is computed to update the nonlinear fundamental nucleus Eq. 2.54 of the FE scheme.

$$\mathbf{k}_{\tau sij}^{T} = \int_L \int_\Omega \mathbf{D}^T(N_i(y)F_\tau(x,z))\mathbf{C}^T\mathbf{D}(N_j(y)F_s(x,z))\mathrm{d}\Omega\mathrm{d}l \tag{2.54}$$

The formulation adopt a set of data points to describe the nonlinear hardening curve, and linear interpolation is used to approximate among the input data. This permits the use of arbitrarly curves directly into the code.

Chapter 3

Carrera Unified Formulation for Fluid-Dynamics

The river bed or a blood vessel can be considered as typical examples of flow with a prominent direction. This fundamental feature of many flows in nature, and in engineering as well, influences many researchers working of fluid-dynamics modeling to derive one-dimensional models to reduce the high computational costs usually present in CFD analysis. In this section, a higher-order 1D model for the resolution of the Stokes equations is presented. This model is developed in the framework of CUF, in which the generalized unknown of the problem, velocity and pressure, are approximated through generic polynomial expansion functions. The resolution of the Galerkin formulation via FEM is discussed and the application of boundary conditions is presented in the end.

3.1 Stokes equations and Galerkin approximation

The domain, considered fixed, is assumed in a Cartesian coordinate system such as the one depicted in Fig. 3.1. Ω indicates the computational domain. The domain is limited, and the boundary surface is called $\partial\Omega$, whereas Γ is used to indicate a transversal surface in the domain. The unit vector ortogonal to the boundaries $\partial\Omega$ is indicated with $\mathbf{n}$.

Let consider the *Navier-Stokes* set of equations. In the complete form, they comprehend the conservation of mass, i.e *continuity equation*, the conservation of *linear momentum* and the conservation of *energy*. These equations are based on the assumption that the fluid is a continuum not made of discrete particles, and the solution is not straightforward due to the presence of the non-linear convective term. However, there are some cases in which it is possible to neglect this contribute as in the case we are dealing with. Let the *Reynolds* number *Re* to be

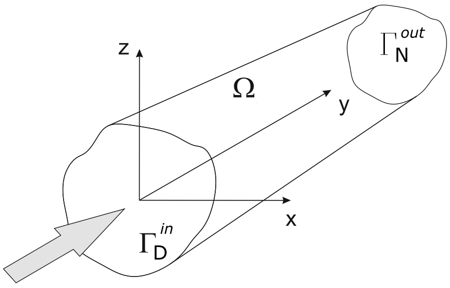

FIG. 3.1: Computational domain Ω.

defined as follow:

$$Re = \frac{|\mathbf{U}|\ \mathcal{D}}{\nu} \tag{3.1}$$

where $\mathcal{D}$ is a dimension representative of the domain Ω, **U** is the representative velocity and ν is the kinematic viscosity in $[m^2/s]$. Generally, in the case of highly viscous fluids, the Reynolds number can be small ($Re \ll 1$) and the contribution of the non-linear convective term can be neglected. In these cases, the Navier-Stokes set of equations for incompressible flow can be reduced to the so-called *Stokes equations*, which hold:

$$\begin{cases} -\,\nu\,\Delta\mathbf{u} + \nabla p = \mathbf{f} & \text{in } \Omega \\ \nabla\cdot\mathbf{u} = 0 & \text{in } \Omega \\ \mathbf{u} = \mathbf{g^D} & \text{on } \Gamma_D \\ \nu\,\dfrac{\partial\mathbf{u}}{\partial\mathbf{n}} - p\,\mathbf{n} = \mathbf{t^N} & \text{on } \Gamma_N \end{cases} \tag{3.2}$$

where the first equation represents the momentum conservation while the second is the continuity equation. **u** represents the velocity in $[m/s]$, p is the pressure in $[m^2/s^2]$ and **f** is the vector of body forces acting in Ω. The last two equations represent the boundary conditions applied to the system; in particular, the first one describes a general non-homogeneous Dirichlet boundary condition at the *inlet* cross section while the second represents the Neumann boundary condition applied at the *outlet* cross-section, see Fig. 3.1. It is remarked that, since we are taking into account a steady flow, all the derivatives in time are neglected.

The *weak* form of Stokes equations is formally obtained By multiplying the momentum equations with a vector function **v** (called *test function*) coming from an adequate functional space V (*test function space*), integrating over the computational volume Ω and using the Green integration relation, one can obtain the *weak* form of Stokes equations. Analogously, the mass conservation equation is multiplied by a *scalar test function* q belonging to a suitable *test functional space* Q and integrated over the computational domain Ω. The weak form of the momentum conservation for the Stokes problem, thus, read as follows:

$$\int_\Omega \Big[-\,\nu\,\Delta\mathbf{u}\cdot\mathbf{v} + \nabla p\cdot\mathbf{v} \Big]\, \mathrm{d}\Omega = \int_\Omega \mathbf{f}\cdot\mathbf{v}\, \mathrm{d}\Omega \tag{3.3}$$

The Green formula is used for the Laplacian operator and for the divergence operator, while considering ν constant for the fluid considered, Eq. 3.3 becomes

$$\int_{\Omega} \nu\, \nabla\mathbf{u} : \nabla\mathbf{v}\, \mathrm{d}\Omega - \int_{\Omega} p\, \nabla\cdot\mathbf{v}\, \mathrm{d}\Omega = \int_{\partial\Omega} \left(\nu\, \frac{\partial \mathbf{u}}{\partial \mathbf{n}} - p\, \mathbf{n} \right) \cdot \mathbf{v}\, \mathrm{d}\Gamma + \int_{\Omega} \mathbf{f} \cdot \mathbf{v}\, \mathrm{d}\Omega \quad (3.4)$$

$\forall\, \mathbf{v} \in V$. The term $\nabla\mathbf{u} : \nabla\mathbf{v}$ in Eq. 3.4 is

$$\nabla\mathbf{u} : \nabla\mathbf{v} = \mathrm{tr} \left(\nabla\mathbf{u}^T\, \nabla\mathbf{v} \right) \quad (3.5)$$

where tr is for the trace of a square matrix. The continuity equation of the Stokes system (second expression in Eq. 3.2) states:

$$- \int_{\Omega} q\, \nabla \cdot \mathbf{u}\, \mathrm{d}\Omega = 0 \quad (3.6)$$

$\forall\, q \in Q$. The negative sign in Eq. 3.6 has been introduced only for the sake of convenience.

3.1.1 Boundary conditions

In a broad sense, mixed Dirichlet−Neumann non-homogeneous boundary conditions are:

$$\begin{cases} \mathbf{u} = \mathbf{g}^D & \text{on } \Gamma_D \\ \nu\, \dfrac{\partial \mathbf{u}}{\partial \mathbf{n}} - p\, \mathbf{n} = \mathbf{t}^N & \text{on } \Gamma_N \end{cases} \quad (3.7)$$

the weak form of the Stokes equations is

$$\begin{cases} \displaystyle\int_{\Omega} \nu\, \nabla\mathbf{u} : \nabla\mathbf{v}\, \mathrm{d}\Omega - \int_{\Omega} p\, \nabla\cdot\mathbf{v}\, \mathrm{d}\Omega = \int_{\partial\Omega} \left(\nu\, \frac{\partial \mathbf{u}}{\partial \mathbf{n}} - p\, \mathbf{n} \right) \cdot \mathbf{v}\, \mathrm{d}\Gamma + \\ \qquad\qquad\qquad\qquad\qquad\qquad \displaystyle\int_{\Omega} \mathbf{f} \cdot \mathbf{v}\, \mathrm{d}\Omega \qquad \forall\, \mathbf{v} \in V \\ \displaystyle - \int_{\Omega} q\, \nabla \cdot \mathbf{u}\, \mathrm{d}\Omega = 0 \qquad \forall\, q \in Q \end{cases} \quad (3.8)$$

where the integral term over $\partial\Omega$ has to be evaluated according to the boundary conditions chosen on $\partial\Omega$. In the case of mixed Dirichlet−Neumann homogeneous boundary conditions, Stokes problem can be significantly simplified. In fact, it is possible to split the integral on the boundary $\partial\Omega$ in Eq. 3.4 on a sum of two integrals over Γ_D and Γ_N. On the other hand, the test functions $\mathbf{v}$ vanish over Γ_D due to the choice of test functions space V. Therefore, in the case of homogeneous boundary conditions, it is straightforward to demonstrate that

$$\int_{\partial\Omega} \left(\nu \frac{\partial \mathbf{u}}{\partial \mathbf{n}} - p\,\mathbf{n} \right) \cdot \mathbf{v}\, \mathrm{d}\Gamma = 0 \tag{3.9}$$

Hence, the weak form of the Stokes problem with mixed Dirichlet−Neumann homogeneous boundary conditions in Eq. 3.2 is

$$\text{Find } \mathbf{u} \in V = \left[\mathrm{H}^1_{\Gamma_D}(\Omega)\right]^3, \; p \in Q = \mathrm{L}^2(\Omega) \; \text{ such that}$$

$$\begin{cases} \displaystyle\int_\Omega \nu\, \nabla\mathbf{u} : \nabla\mathbf{v}\, \mathrm{d}\Omega - \int_\Omega p\, \nabla \cdot \mathbf{v}\, \mathrm{d}\Omega = \int_\Omega \mathbf{f} \cdot \mathbf{v}\, \mathrm{d}\Omega & \forall\, \mathbf{v} \in V \\ \displaystyle -\int_\Omega q\, \nabla \cdot \mathbf{u}\, \mathrm{d}\Omega = 0 & \forall\, q \in Q \end{cases} \tag{3.10}$$

where $L^2(\Omega)$ is the space of square-integrable functions on $\Omega \subset R$ and H^3 is the *Sobolev space* formed by the totality of functions $L^2(\Omega)$ such that all their derivatives up to order 3 belong to $L^2(\Omega)$.

3.1.2 Galerkin approximation

The Galerkin approximation of the Stokes problem with homogeneous boundary conditions as in Eq. 3.10 has the following form:

$$\text{Find } \mathbf{u}_h \in V_h, \; p_h \in Q_h \text{ such that}$$

$$\begin{cases} \displaystyle\int_\Omega \nu\, \nabla\mathbf{u}_h : \nabla\mathbf{v}_h\, \mathrm{d}\Omega - \int_\Omega p_h\, \nabla \cdot \mathbf{v}_h\, \mathrm{d}\Omega = \int_\Omega \mathbf{f} \cdot \mathbf{v}_h\, \mathrm{d}\Omega & \forall\, \mathbf{v}_h \in V_h \\ \displaystyle -\int_\Omega q_h\, \nabla \cdot \mathbf{u}_h\, \mathrm{d}\Omega = 0 & \forall\, q_h \in Q_h \end{cases} \tag{3.11}$$

The terms u_h and p_h in Eqs. 3.11 are the discrete solutions of the Stokes problem in weak form (Eq. 3.10). Let the bilinear forms $a : V \times V \to \mathbb{R}$ and $b : V \times Q \to \mathbb{R}$ to be defined as follows:

$$a(\mathbf{u}, \mathbf{v}) = \int_\Omega \nu\, \nabla\mathbf{u} : \nabla\mathbf{v}\, \mathrm{d}\Omega \tag{3.12}$$

$$b(\mathbf{u}, q) = -\int_\Omega q\, \nabla \cdot \mathbf{u}\, \mathrm{d}\Omega \tag{3.13}$$

With this notation, the Galerkin approximation of the Stokes equation reads

$$\text{Find } \mathbf{u}_h \in V_h,\ p_h \in Q_h \text{ such that}$$

$$\begin{cases} a\left(\mathbf{u}_h,\, \mathbf{v}_h\right) + b\left(\mathbf{v}_h,\, p_h\right) = \left(\mathbf{f},\, \mathbf{v}_h\right) & \forall\, \mathbf{v}_h \in V_h \\ b\left(\mathbf{u}_h,\, q_h\right) = 0 & \forall\, q_h \in Q_h \end{cases} \tag{3.14}$$

where $V_h \subset V$ and $Q_h \subset Q$ represent two families of finite dimensional subspaces depending on a real positive discretization parameter h.

3.2 One-dimensional Carrera Unified Formulation models for Stokes flows

The prominent direction of many flows is an important feature in the view of approximation via 1D models. In this context, many reduced models have been proposed even if the description of higher-order phenomena is not alway accomplished. The one-dimensional Carrera Unified Formulation (CUF) is here used along with FEM to approximate the Galerkin formulation of the Stokes equations.

According to CUF, the velocity field $\mathbf{u}_h$ and the pressure field p_h are expressed, in a unified manner, as a generic expansion of the generalized unknowns through arbitrary functions of the cross-section domain coordinates:

$$\mathbf{u}_h(x, y, z) = F_\tau^U(x, z)\mathbf{u}_\tau(y), \qquad \tau = 1, 2, \cdots, M^U \tag{3.15}$$

$$p_h(x, y, z) = F_m^P(x, z)p_m(y), \qquad m = 1, 2, \cdots, M^P \tag{3.16}$$

where $\mathbf{u}_\tau(y)$ is the vector describing the velocity field and $p_m(y)$ is the scalar pressure, function of the pipe axis y. According to CUF, τ and m indicate summations. F_τ^U or F_m^P are the interpolation functions spread over the section Γ, which lies in the Cartesian plane xz, and M^U and M^P indicate the terms involved in the expansion, for velocity and pressure respectively. These terms are strictly connected with the expansion order adopted in the description of the velocity and pressure fields, and, indeed, with the accuracy of the model. A brief introduction of the cross-sectional functions that have been adopted in the framework of CUF-CFD can be found in Section 2.1.2.

3.3 Finite Element formulation

The main advantage of CUF is that it allows to write the governing equations in a unified manner. The class of expanding functions (e.g., TE, LE) and the polynomial order of the theory become arbitrary inputs of the model. In the case of FE discretization of the tube axis, the generalized velocities $\mathbf{u}_\tau\left(y\right)$ and

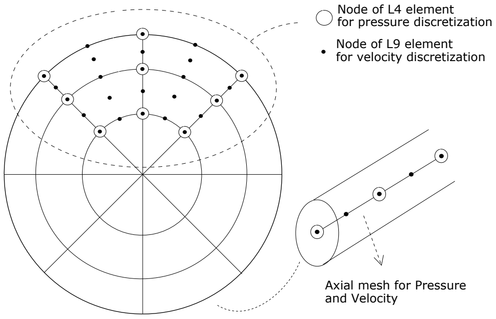

Fig. 3.2: CUF LE model discretizations of pressure and velocity fields.

pressures $p_m(y)$ are described as a function of the unknown nodal vectors, $\mathbf{u}_{\tau i}$ and p_{mt} , and the 1D shape functions, N_i and N_t , as follows

$$\mathbf{u}_\tau(y) = N_i^U(y)\,\mathbf{u}_{\tau i}, \qquad i = 1, \ldots, N_n^U \tag{3.17}$$

$$p_m(y) = N_t^P(y)\,p_{mt}, \qquad i = 1, \ldots, N_n^P \tag{3.18}$$

where i and t stand for summation. N_n^P and N_n^U indicate the order of the shape functions adopted along the FEM for pressure and velocity, respectively. The 1D shape functions N_i^U and N_t^P can be arbitrary and, usually, different in order.

Linking the FE formulation in Eqs. 3.17 and 3.18 with CUF (Eqs. 3.16) the final expressions for the description of the unknown fields are

$$\mathbf{u}_h(x, y, z) = F_\tau^U(x, z)\,N_i^U(y)\,\mathbf{u}_{\tau i}, \qquad \tau = 1, \ldots, M^U \quad i = 1, \ldots, N_n^U \tag{3.19}$$

$$p_h(x, y, z) = F_m^P(x, z)\,N_t^P(y)\,p_{mt}, \qquad m = 1, \ldots, M^P \quad t = 1, \ldots, N_n^P \tag{3.20}$$

3.3.1 The fundamental nuclei for Computational Fluid Dynamics

Under the 1D CUF point of view, the test functions $\mathbf{v}_h \in V_h$ and $q_h \in Q_h$ are described in an analog way to Eqs. 3.19 and 3.20. According to Refs. [107, 108], the Galerkin approximation in Eq. 3.11 is verified for every function of the basis of V_h and Q_h, since all the functions belonging to V_h and Q_h are a linear combination of the basis functions. Hence, in the framework of CUF, the solution of the Galerkin approximation is provided by the following system of equations:

Find $\mathbf{u}_h \in V_h,\ p_h \in Q_h$ such that

$$\begin{cases} a(\mathbf{u}_h, \boldsymbol{\varphi}_{\tau ie}) + b(\boldsymbol{\varphi}_{\tau ie}, p_h) = (\mathbf{f}, \boldsymbol{\varphi}_{\tau ie}) & \forall\tau,\ \forall i,\ \forall e \\ b(\mathbf{u}_h, \phi_{mt}) = 0 & \forall m,\ \forall t \end{cases} \tag{3.21}$$

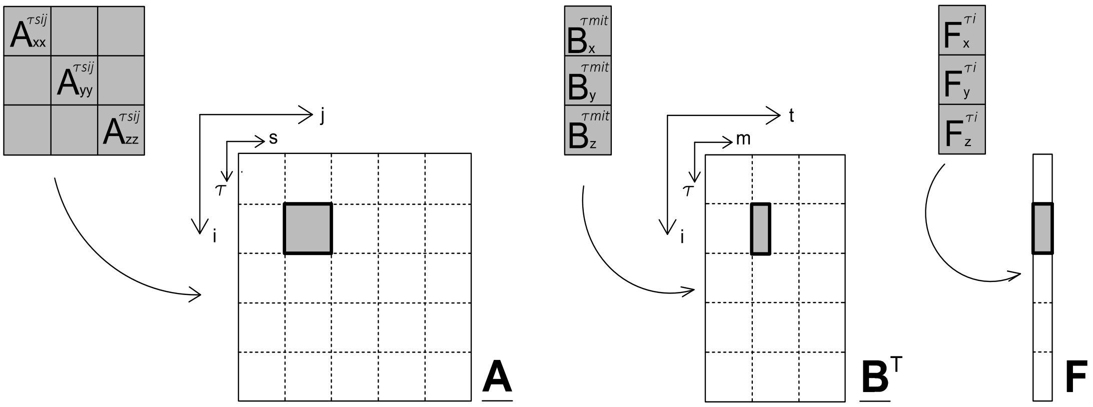

FIG. 3.3: Procedure to build the finite element matrices and vectors expanding the fundamental nuclei. Scheme for *momentum* conservation equation.

with $\tau = 1, \ldots, M^U$, $i = 1, \ldots, N_n^U$, $e = 1, \ldots, 3$, $m = 1, \ldots, M^P$, $t = 1, \ldots, N_n^P$. The index e refers to the three components of the velocity field, and

$$\boldsymbol{\varphi}_{\tau i e}(x,\, y,\, z) \;=\; \left\{ \begin{array}{c} \delta_{1e}\, F_\tau^U(x,\, z)\, N_i^U(y) \\ \delta_{2e}\, F_\tau^U(x,\, z)\, N_i^U(y) \\ \delta_{3e}\, F_\tau^U(x,\, z)\, N_i^U(y) \end{array} \right\} \tag{3.22}$$

are the bases of the space V_h due to the 1D CUF approximation and $\delta_{\mathsf{ke}} = 1$ if $e = \mathsf{k}$, 0 otherwise. Similarly,

$$\phi_{mt}(x,\, y,\, z) \;=\; F_m^P(x,\, z)\, N_t^P(y) \tag{3.23}$$

For the sake of clarity, indices s (instead of τ) and j (instead of i) are introduced into Eq. 3.21 for the CUF approximation of the discrete solution $\mathbf{u}_h$ (see Eq. 3.19). Due to long mathematical transformations (see [84]), Eq. 3.21 becomes the following system of algebraic equations:

$$\left\{ \begin{array}{ll} \mathbf{A}^{\tau sij}\, \mathbf{q}_{sj} + \mathbf{B}^{\tau mit^T}\, p_{mt} \;=\; \mathbf{F}^{\tau i} & \quad \forall\, \tau,\;\; \forall\, i \\ \mathbf{B}^{mstj}\, \mathbf{q}_{sj} \;=\; \mathbf{0} & \quad \forall\, m,\;\; \forall\, t \end{array} \right. \tag{3.24}$$

where $\mathbf{A}^{\tau sij}$ is the *fundamental nucleus* related to the bilinear form $a(\mathbf{u}_h,\, \boldsymbol{\varphi}_{\tau i e})$ of the 1D CUF model;

$$
\begin{aligned}
\mathbf{A}^{\tau s i j} = & \left[\nu \int_L N_i^U \, N_j^U \, \mathrm{d}y \int_{\Gamma_S} F_{\tau,x}^U \, F_{s,x}^U \, \mathrm{d}\Gamma + \nu \int_L N_{i,y}^U \, N_{j,y}^U \, \mathrm{d}y \int_{\Gamma_S} F_\tau^U \, F_s^U \, \mathrm{d}\Gamma + \right. \\
& \left. \nu \int_L N_i^U \, N_j^U \, \mathrm{d}y \int_{\Gamma_S} F_{\tau,z}^U \, F_{s,z}^U \, \mathrm{d}\Gamma \right] \mathbf{I}
\end{aligned}
\tag{3.25}
$$

$\mathbf{B}^{\tau m i t^T}$ is the *fundamental nucleus* related to the bilinear form $b\,(\boldsymbol{\varphi}_{\tau i e},\, p_h)$;

$$
\mathbf{B}^{\tau m i t^T} = \left\{ \begin{array}{l}
- \displaystyle\int_L N_i^U \, N_t^P \, \mathrm{d}y \int_{\Gamma_S} F_{\tau,x}^U \, F_m^P \, \mathrm{d}\Gamma \\
- \displaystyle\int_L N_{i,y}^U \, N_t^P \, \mathrm{d}y \int_{\Gamma_S} F_\tau^U \, F_m^P \, \mathrm{d}\Gamma \\
- \displaystyle\int_L N_i^U \, N_t^P \, \mathrm{d}y \int_{\Gamma_S} F_{\tau,z}^U \, F_m^P \, \mathrm{d}\Gamma
\end{array} \right\}
\tag{3.26}
$$

$\mathbf{B}^{m s t j}$ is the *fundamental nucleus* corrisponding to the bilinear form $b\,(\mathbf{u}_h,\, \phi_{m t})$;

$$
\mathbf{B}^{m s t j} = \left\{ \begin{array}{l}
- \displaystyle\int_L N_t^P \, N_j^U \, \mathrm{d}y \int_{\Gamma_S} F_m^P \, F_{s,x}^U \, \mathrm{d}\Gamma \\
- \displaystyle\int_L N_t^P \, N_{j,y}^U \, \mathrm{d}y \int_{\Gamma_S} F_m^P \, F_s^U \, \mathrm{d}\Gamma \\
- \displaystyle\int_L N_t^P \, N_j^U \, \mathrm{d}y \int_{\Gamma_S} F_m^P \, F_{s,z}^U \, \mathrm{d}\Gamma
\end{array} \right\}^T
\tag{3.27}
$$

and $\mathbf{F}^{\tau i}$ is the *fundamental nucleus* related to the term $(\mathbf{f},\, \boldsymbol{\varphi}_{\tau i e})$.

$$
\mathbf{F}^{\tau i} = \int_\Omega F_\tau^U \, N_i^U \, \mathbf{f} \, \mathrm{d}\Omega
\tag{3.28}
$$

In Eq. 3.25, $\mathbf{I}$ is the 3×3 identity matrix.

Like in other applications of CUF, the fundamental nuclei are formally independent of the theory orders (N^U and N^P) and on the FEM shape functions (N_n^U and N_n^P). These nuclei have to be expanded against the indices τ, s, m, i, j, and t. For a detailed description of the derivation of the fundamental nuclei, interested readers are referred to [109], where structural problems are mainly presented. This expansion leads to the formulation of the elemental FE arrays associated to the Galerkin approximation of the Stokes equations. The expansion is processed according to a scheme depicted in Fig. 3.3. At the end of the assembly of all FEs, the final system of equations reads

$$
\left\{ \begin{array}{l}
\mathbf{A}\,\mathbf{q} + \mathbf{B}^T \mathbf{p} = \mathbf{F} \\
\mathbf{B}\,\mathbf{q} = \mathbf{0}
\end{array} \right.
\tag{3.29}
$$

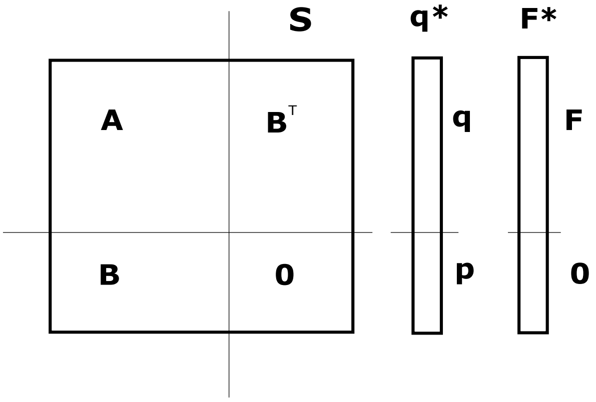

Fig. 3.4: Condensed problem in FE scheme.

It is important to note the following relation between the nuclei of the matrices $\mathbf{B}^T$ and $\mathbf{B}$:

$$\mathbf{B}^{mstj^T} = \mathbf{B}^{\tau mit} \tag{3.30}$$

which is essentially true except from the use of different indices.

The system of Eq. 3.29 can be written collecting matrices $\mathbf{A}$, $\mathbf{B^T}$, $\mathbf{B}$ and a zero matrix $\mathbf{0}$ in a single symmetrical matrix $\mathbf{S}$, collecting the unknowns $\mathbf{q}$ and $\mathbf{p}$ in a single vector of unknowns $\mathbf{q}^\star$, and collecting the column vectors $\mathbf{F}$ and $\mathbf{0}$ in a single column vector $\mathbf{F}^\star$ following the scheme in Fig. 3.4.

$$\mathbf{S}\mathbf{q}^\star = \mathbf{F}^\star \tag{3.31}$$

3.4 Boundary conditions

Figure 3.5 presents the typical problem taken into account in this thesis, in which the boundary walls $\partial\Omega$ of the pipe are divided into inlet, outlet and lateral surfaces, called $\partial\Omega = \Gamma^{\text{in}} \cup \Gamma^{\text{out}} \cup \Gamma^{\text{l}}$. Subscripts in Fig. 3.5 stand for Dirichlet (D) and Neumann (N) boundary conditions. Considering only homogeneous Neumann boundary conditions, the solution of the problem in Eq. 3.29 implicitly verifys this condition. By the contrast, the application of Dirichlet boundary conditions needs the use of some mathematical procedures. Briefly, let consider the generic Dirichlet boundary condition as:

$$\mathbf{u}|_{\Gamma_D} = \mathbf{g}^D \tag{3.32}$$

where $\mathbf{g}^D$ is a random known function and Γ_D is also a generic cross-section of the pipe (e.g. Γ_D^{in}) or the lateral walls Γ_D^{l}. Equation 3.32 is imposed by formulating

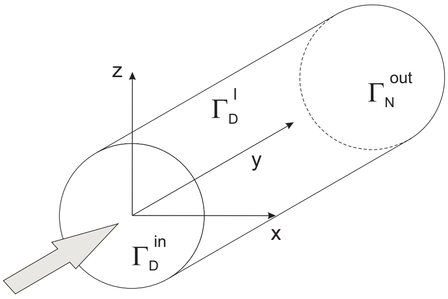

FIG. 3.5: Pipe with circular cross-section

the correspondent Galerkin approximation; i.e.,

$$\text{Find } \mathbf{u}_h \in V_h \text{ such that}$$
$$\int_{\Gamma_D} \mathbf{u}_h \cdot \mathbf{v}_h \, \mathrm{d}\Gamma = \int_{\Gamma_D} \mathbf{g}^D \cdot \mathbf{v}_h \, \mathrm{d}\Gamma \qquad \forall\, \mathbf{v}_h \in V_h \tag{3.33}$$

By recalling CUF and FEM approximation as seen previously, the application of the Dirichlet boundary condition is expressed in terms of fundamental nuclei in the linear system as follows:

$$\mathbf{A}_{BC}^{\tau sij}\, \mathbf{q}_{sj} = \mathbf{F}_{BC}^{\tau i} \tag{3.34}$$

In the case of orthogonal BCs (on the cross-section i.e.), the fundamental nuclei are

$$\mathbf{A}_{BC}^{\tau sij} = \left[N_i^U(y_g)\, N_j^U(y_g) \int_{\Gamma_D} F_\tau^U\, F_s^U\, \mathrm{d}\Gamma \right] \mathbf{I} \tag{3.35}$$

$$\mathbf{F}_{BC}^{\tau i} = N_i^U(y_g) \int_{\Gamma_D} F_\tau^U\, \mathbf{g}^D\, \mathrm{d}\Gamma \tag{3.36}$$

where y_g is the coordinate along the y-axis of the pipe where the condition is applied. Whereas, in the case of BC imposed on Γ_D^1, the fundamental nuclei are

$$\mathbf{A}_{BC}^{\tau sij} = \left[\int_L N_i^U\, N_j^U\, \mathrm{d}y \int_{\gamma_S} F_\tau^U\, F_s^U\, \mathrm{d}\gamma \right] \mathbf{I} \tag{3.37}$$

$$\mathbf{F}_{BC}^{\tau i} = \int_{\Gamma_D} N_i^U\, F_\tau^U\, \mathbf{g}^D\, \mathrm{d}\Gamma \tag{3.38}$$

where γ_S is the contour of the cross-section.

The FN of the Dirichlet boundary conditions have to be expanded according to the indexes, summed to the others, and then applied to Eq. 3.29 by penalization method; i.e.,

$$\begin{cases} [\mathbf{A} + \alpha\, \mathbf{A}_{BC}]\, \mathbf{q} + \mathbf{B}^T \mathbf{p} = [\mathbf{F} + \alpha\, \mathbf{F}_{BC}] \\ \mathbf{B}\, \mathbf{q} = \mathbf{0} \end{cases} \tag{3.39}$$

where α is a the penalty number. Equation 3.39 is the final algebraic system of equations to be calculated. For a detailed description of the CUF derivation of the Stokes problem, the reader is referred to [84].

Chapter 4

Computational Fluid Dynamics and Carrera Unified Formulation with Node-Dependent Kinematics

The perspective of simulating very complex fluid-dynamic systems, together with the growing necessity to decrease the computational times, influences the researchers to develop models and designs able to satisfy these requirements. The development of accurate but straightforward models does not represent an easy challenge, and often it requires the involvement of strong assumptions. This chapter extends the use of one-dimensional elements with node-dependent kinematics NDK to the analysis of Stokes flows. The novel implementation exposed in this chapter allows to increase the accuracy of the model only in the areas of the domain where it is required, i.e. particular boundary condition, barriers or sudden expansion. Refined one-dimensional models based on Taylor and Lagrange expansions are used to interpolate the unknowns fields according to the CUF. For the sake of clarity, the dissertation moves from a node-dependent kinematic model for a generic unknown field and then pass to the specific node-dependent kinematic model for fluid-dynamics problems.

4.1 One-dimensional fluid-dynamics models with Node-Dependent Kinematics

The perspective of simulating very complex fluid-dynamic systems, together with the growing necessity to decrease the computational times, influences the researchers to develop mathematical theories and numerical methods able to satisfy these requirements. The development of accurate but straightforward models does not represent an easy challenge, and often it requires the involvement of strong assumptions. Modern Computational Fluid-Dynamics (CFD), in which even a simple 3D analysis requires a considerable computational power, is well-suited to

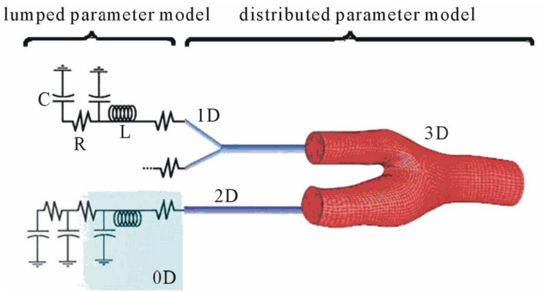

FIG. 4.1: A scheme of three different level of accuracy on the description of circulatory system. Image taken from [1]

this cause, at least for flows with a prominent direction. The first reduced description of a fluid-dynamic network dates back in the 1960s and was a model with lumped parameters. In this context, the flow parameters were expressed by algebraic equations that *lump* everything in a relatively small number of parameters, similarly to electrical circuits, [110, 111]. Over time, some progress was made due to the introduction of the *transversally averaged* flows. In this case, the pressure and the flow rate are averaged in each transversal cross-section, neglecting the other components of the motion. This method allows obtaining relatively simple equations, even if it suffers the more complicated topology, [112]. Recently, these limitations have been overcome locally due to the advent of one-dimensional (1D) models for the resolution of Navier-Stokes equations. In this framework, the axial flow parameters are spread on the cross-section through different mathematical methods. Karnidakis and Sherwin [113] developed the idea of a 1D finite element model coupled to spectral/hp function; these preliminary results incouraged Pontaza and Reddy [114] to implement them with a least-square method, and Smith *et al.* to develop a finite difference scheme, [78]. More recently, an iso-geometric analysis with spectral functions has been proposed by Guzzetti *et al.* in [115].

Although the significant achievements, the problem of providing an efficient modelling methodology to describe entire networks of 1D flows (e.g., cardiocirculatory system) is still open. As an example, a detailed analysis of an artery branch cannot neglect the interaction with the rest of the cardiocirculatory system, but, at the same time, it is unthinkable to model the whole system with the same accuracy all over the problem support. Because the use of three-dimensional models for the analysis of the complete domain could lead to huge computational costs, several attempts have been done to use reduced refined models only in a small region and reduced models elsewhere. A preliminary analysis of this argument has been conducted by Formaggia *et al.* [116], whereas a multi-scale model for the coupling of one-dimensional with 2D/3D models has been proposed in Ref. [76]. The models with variable kinematics (*node-dependent kinematics*, NDK) have been proposed, for structural mechanics, by Carrera and Zappino [117], in the framework of the Carrera Unified Formulation (CUF). The node-dependent kinematic approach, as used in Ref. [118, 66, 119], allows to change the kinematic assumptions node-by-node, as in Fig. 4.2. In this manner, by using the scalable properties of CUF

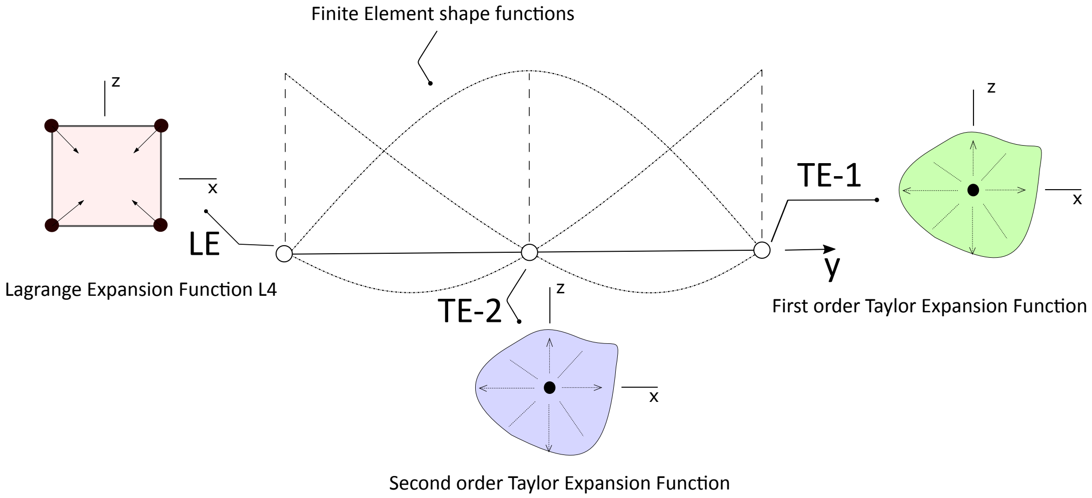
Finite Element shape functions
z
x
LE
Lagrange Expansion Function L4
TE-1
z
x
y
First order Taylor Expansion Function
TE-2
z
x
Second order Taylor Expansion Function

Fig. 4.2: A three-node 1D finite element with node-dependent kinematics.

and the finite element shape functions, the analyst can gradually increase the accuracy of the solution in determined zones of interest, without introducing any mathematical aartificies. In other words, low-order models can be combined with higher-order models with 3D accuracy without any accuracy loss if CUF-NDK methodology is used.

4.2 The NDK model for Fluid-Dynamics

A higher-order approximation allows to the one-dimensional models to solve complicated problems, even if the complexity is limited only to some regions of the domain. Particular inlet velocity profiles as well as pipe with non conventional geometries are examples of local problems in which is suitable a node-dependent kinematics scheme. In the CUF framework, it means to be able to adopt different interpolating functions at each node, different in terms of accuracy and family (TE/LE).

Taking into account, for instance, the fluid domain in Fig. 4.3, a different kinematics has been assigned at each of the FEM nodes, both for velocity and pressure. In this figure, a quadratic and a linear FE were used for the description of the velocity and pressure respectively. The expansion of the indexes in the figure depends on the kinematics assigned to each node, which determines the dimension of the elemental FE arrays associated to the Galerkin approximation of the Stokes problem in Eq. 3.24. In particular, the velocity field of the Fig. 4.3, can be written at the first node as:

$$\mathbf{u}^1 = F^1_\tau \mathbf{u}_{1\tau}, \qquad \tau = 1, 2, \cdots, M^U_1 \tag{4.1}$$

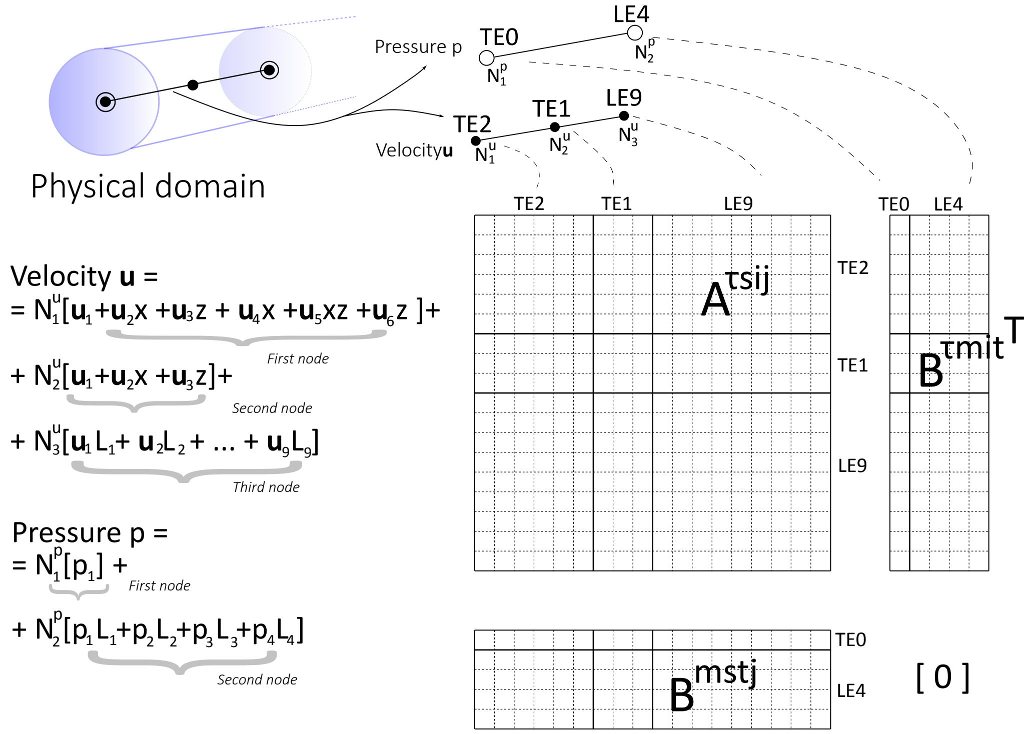
Pressure p
TE0
LE4
N_1^p
N_2^p
TE2
TE1
LE9
Velocity **u**
N_1^u
N_2^u
N_3^u
Physical domain
Velocity **u** =
= N_1^u[$\mathbf{u}_1$+$\mathbf{u}_2$x +$\mathbf{u}_3$z + $\mathbf{u}_4$x +$\mathbf{u}_5$xz +$\mathbf{u}_6$z]+
First node
+ N_2^u[$\mathbf{u}_1$+$\mathbf{u}_2$x +$\mathbf{u}_3$z]+
Second node
+ N_3^u[$\mathbf{u}_1$L$_1$+ $\mathbf{u}_2$L$_2$ + ... + $\mathbf{u}_9$L$_9$]
Third node
Pressure p =
= N_1^p[p$_1$] +
First node
+ N_2^p[p$_1$L$_1$+p$_2$L$_2$+p$_3$L$_3$+p$_4$L$_4$]
Second node
TE2
TE1
LE9
TE0
LE4
$A^{\tau sij}$
TE2
TE1
LE9
$B^{\tau mit^T}$
TE0
LE4
B^{mstj}
[0]

FIG. 4.3: FEM model of fluid-dynamics model using node-dependent kinematics. The expansion of the velocity and of the pressure fields change node-by-node and this determines the dimension of the matrices.

at the second node, the velocity field is:

$$\mathbf{u}^2 = F_\tau^2 \mathbf{u}_{2\tau}, \qquad \tau = 1, 2, \cdots, M_2^U \tag{4.2}$$

while at the third one is:

$$\mathbf{u}^3 = F_\tau^3 \mathbf{u}_{3\tau}, \qquad \tau = 1, 2, \cdots, M_3^U \tag{4.3}$$

The expansion functions F_τ^1, F_τ^2 and F_τ^3 can be chosen arbitrarily in each node. At node 1 a second-order TE model has been used, a first-order TE model has been employed at node 2 while a quadratic LE expansion has been imposed at node 3. As a result, the expression of the three-dimensional velocity field for the whole element is:

$$\mathbf{u} = F_\tau^1 N_1 \mathbf{u}_{1\tau} + F_\tau^2 N_2 \mathbf{u}_{2\tau} + F_\tau^3 N_3 \mathbf{u}_{3\tau}, \qquad \tau = 1, 2, \cdots, M_i^U \tag{4.4}$$

An analogue procedure is valid for the pressure field. The different expansions communicate one to each other through the FE shape functions N_i along the element length, in order to obtain a smooth transition of the unknown field among the three nodes. In this way, the continuity of the solution is ensured at each point. To summarize, the node-dependent feature means that:

$$F_\tau(x,z) \longrightarrow F^i_\tau(x,z) \tag{4.5}$$

$$M \longrightarrow M_i \tag{4.6}$$

where the Eq. 4.5 defines the expansion function as property of the nodes and not of the element, and the number of terms in the expansion, M, can be different at each node, as in Eq. 4.6 and the i underlines this aspect. Finally, the general equations of the variable fields are:

$$\mathbf{u} = F^i_\tau N_i \mathbf{u}_{i\tau}, \qquad \tau = 1,2,\cdots,M^U_i; \qquad i = 1,\cdots,N^U_n \tag{4.7}$$

$$p = F^t_m N_t p_{tm}, \qquad m = 1,2,\cdots,M^P_t; \qquad t = 1,\cdots,N^P_n. \tag{4.8}$$

This feature allows to control the dimension of the matrices to save computational costs. For further detailes about the CUF-NDK, see Ref. [65, 117, 120], where this methodology has been employed for the analysis of elastic structures.

Chapter 5

Numerical Results

In this chapter, different analyses and results are discussed. In the first part, the proposed CUF models for structural analysis are presented. Results from both static and free vibrations of biostructures in linear and nonlinear framework are provided. In the second part, the application of CUF for fluid-dynamic typical problems, and the extension to the results coming from the NDK formulation are then discussed. The attention is focused on the capability of the proposed methodology to carry out enhanced analyses of complex problems with very low computational efforts

5.1 Structural Mechanics - Linear Materials

In this section the capabilities of one-dimensional CUF models for the mechanical response of bio-structures in linear regime are assessed. The examples presented hereinafter are the direct application of the metodology introduced in Chapter 2, which is largely explained in [109]. In particular, the static and the free vibration analysis of an atherosclerotic plaque and a dental prosthesis are here performed. The results take into account the comparison among different one-dimensional models and then the verification of these with one coming from solid FE tools.

5.1.1 Atherosclerotic Plaque

The first example considered on the demonstration of the efficiency of 1D CUF models for structural analysis is that about a human external iliac arterial branch with a severe atherosclerotic plaque. In particular, a portion of an artery with an important lumen reduction is here taken into account. Published works states that, due to the images obtained by hrMRI (high resolution magnetic resonance imaging) and from histological results, it is possible to recognize the variuos component of the plaque [121, 122]. In this manner, six different materials are identified for this pathology (see Fig. 5.25): the adventititia (A), the calcification (C), the lipid

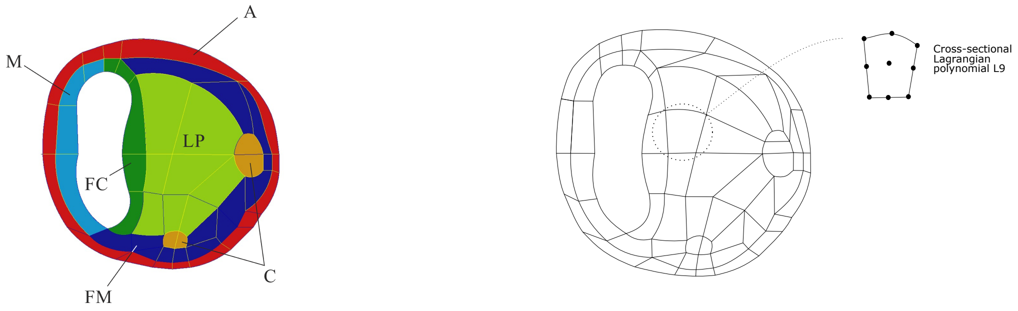

(a) Different Materials

(b) LE9 Subdivision

FIG. 5.1: Atherosclerotic plaque. Materials subdivision (a) and LE9 subdivision (b)

Tissue	E [MPa]	ν
Calcification	12	0.33
Lipid Pool	0.1	0.33
Fibrous Cap	2.4	0.33
Media	1	0.33
Fibrotic Media	5	0.33
Adventitia	2.5	0.33

TABLE 5.1: Materials properties of the atherosclerotic plaque.

pool (LP), the fibrous cap (FC), the non-diseased media (M), and the fibrotic media (FM), which is in fact the sum of fibrotic intima and diseased fibrotic media. For illustration reasons, the cross-section width and height are approximately 15 mm, and the length is 40 mm. For the static analysis, we consider two different situations of loads and BCs. Iniatially, the portion of artery is considered clamped at both extremities ($y = 0$ and $y = L$) and undergoes an 180 mmHg of blood phsiological pressure. In the othe situation, an non-symmetric longitudinal load is enforced and one extrmity is left free in order to analyze the bending response of the biostructure. 3D solid models are developed in NASTRAN commercial tool, to make the comparisons. These models are made by 382700 HEX elements (398041 nodes) and 1194123 DOFs. These 3D models are compared to 1D CUF models. The beam models are discretized in 10 B4 (cubic) FEs along the main axis, and different order of polynomial functions (TE) are adopted for the description of the cross-section. On the other hand, the LE models, employed 59 L9 and 2 L6 polynomials, collecting 270 nodes. The discretization used in LE models is visible in Fig. 5.1(b).

Isotropic linear constitutive relations are here considered for the description of the materials. The isotropic feature of this tissues come from literature, [121, 123], and are exposed in Table 5.1.

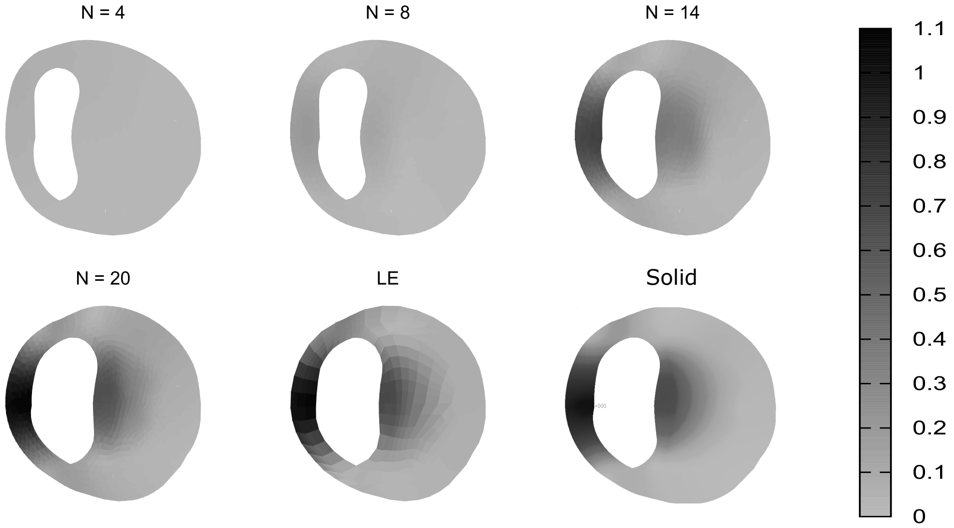

Fig. 5.2: Horizontal displacement component u_x on the mid-span cross-section. Comparison between TE ($N = 4$ to $N = 20$), LE, and 3D NASTRAN Solid model. Values in mm.

5.1.1.1 Static Analysis

The analysis of the dispalcement field obtained from the first load case is shown Fig. 5.2, in which the on-section displacements distribution for different models, 1D and 3D, is shown The proposed refined models can describe with accuracy the response of the multi-material structure, and lipid pool as well as the fibrous cap undergo larger deformation. On the other hand, this effect is less evident in the calcified area, due to the different level of stiffness. As expected, 1D models with higher-order kinematics are required to predict the complex stress/strain field, but 3D-like solution can be obtained from them. To reinforce this thesis, Table 5.2 enlists the maximum displacements value of media (M), adventitia (A) and the fibrous cap (FC) for the various models addressed. Additionnaly, the total numbers of DOFs for each model employed are shown in the same table.

Conversely, Table 5.3, collects static computational test results regarding the stress. In particular, the different materials values of normal and shear stress, σ_{xx} and σ_{xz}, are shown in Table 5.3, compueted at mid-span cross-section.

Some remarks can be summarize as follows:

- Classical and low-order TE models cannot describe correctly the displacement and the stress values.

Model	u^{M}_{max}	u^{A}_{max}	u^{FC}_{max}	DOFs
EBBT	0.0041	0.0041	0.0041	93
TBT	0.0093	0.0093	0.0093	155
N=1	0.5666	0.6210	0.3496	279
N=4	0.0538	0.0539	0.0262	1395
N=8	0.2019	0.1933	0.1232	4185
N=10	0.3088	0.2877	0.1710	6138
N=14	0.7065	0.6662	0.3862	11160
N=18	0.9213	0.8929	0.5552	17670
N=20	1.0294	1.0035	0.6211	21483
LE	1.0153	0.9581	0.7209	26730
Solid	1.0587	1.0488	0.7209	1194123

TABLE 5.2: Maximum horizontal displacement component, u_x (mm), of the atherosclerotic plaque subjected to internal pressure.

Model	σ_{xx}	σ_{xz}	σ_{xx}	σ_{xz}	σ_{xx}	σ_{xz}	σ_{xx}	σ_{xz}	σ_{xx}	σ_{xz}	σ_{xx}	σ_{xz}
	FM		M		LP		A		FC		C	
N=4	2.683	0.101	1.379	0.000	0.011	0.000	-0.010	-0.225	3.984	0.045	1.077	1.522
N=8	0.279	-0.011	2.772	-0.185	-0.280	0.017	2.012	0.032	1.658	0.259	-2.607	1.252
N=10	-6.965	-0.203	-1.788	-0.181	0.164	0.059	1.720	-0.683	-1.120	0.088	2.866	0.379
N=14	-2.345	-0.057	-9.435	-0.098	-2.066	0.070	2.534	-1.726	-9.756	-0.408	1.936	0.709
N=18	-1.382	-0.232	-9.188	-0.160	-0.857	0.120	5.820	-1.441	-5.981	-0.482	3.985	-0.708
N=20	1.132	0.140	-4.668	-0.187	-1.150	0.118	4.870	-1.919	-4.424	-0.276	6.786	-1.332
LE	-0.052	-0.025	-3.670	-0.546	-1.310	0.105	4.550	-1.750	-5.290	0.072	3.370	0.920
Solid	-0.186	-0.014	-1.907	-0.246	-1.458	0.137	4.649	-1.635	-1.926	0.119	3.206	0.860

TABLE 5.3: In-plane normal, σ_{xx}, and shear, σ_{xz}, stress components (10^2 MPa) on each material of the atherosclerotic plaque at mid-span cross-section subjected to internal pressure.

- The accuracy increases with the order of TE models, till approaching that of 3D analyses.
- LE model are capable to reproduce the 3D results with lower computational effort.

In the second loadind condition, clamped-free boundary conditions is enforced to the structure. The load is applied asymmetrically and parallel to the main axis, along the fibrous cap and the media length, to simulate the bending caused by viscous forces. As a result, Fig. 5.3 presents the σ_{yy} axial stress field on the orthogonal section of the vessel. Furthermore, these stress values are collected in Table 5.4 together with the values of maximum displacements in the horizontal direction.

The following comments can be resumed:

- Due to their intrinsic hypotheses, the classical beam model are not able to predict the displacement field for each material over the cross-section.

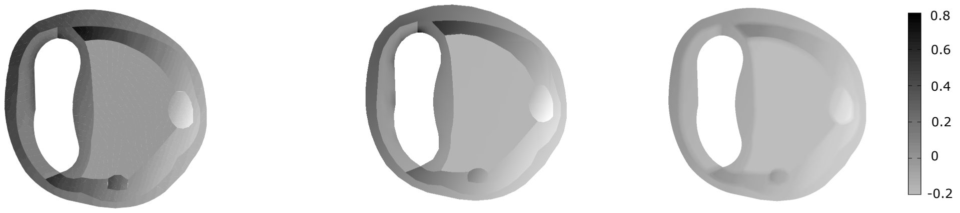

(a) $N = 20$ (b) LE (c) Solid

FIG. 5.3: Axial stress σ_{yy} MPa distribution on the mid-span cross-section of the atherosclerotic plaque subjected to clamped-free boundary conditions and forces along y.

Model	σ_{yy} at (0,0)	σ_{yy} at (15,0)	u^M_{max}	u^{FC}_{max}
EBBT	0.345	-0.090	12.574	12.574
TBT	0.345	-0.090	12.574	12.574
N=1	0.345	-0.090	12.574	12.574
N=4	0.322	-0.098	12.117	12.113
N=8	0.345	-0.089	11.983	12.149
N=10	0.331	-0.094	11.795	11.992
N=14	0.333	-0.084	11.447	11.848
N=18	0.327	-0.086	11.339	11.865
N=20	0.353	-0.088	11.304	11.862
LE	0.324	-0.080	11.245	11.704
Solid	0.340	-0.087	10.955	11.707

TABLE 5.4: Values of σ_{yy} MPa and u_x mm for different points and materials of the section.

- Taking into account the bending loading condition, higher-order 1D CUF models seems to be very accurate and in accordance to 3D results. In addition, these models demonstrate high computational efficiency as well.

5.1.1.2 Free Vibration Analysis

The analysis of free-vibrations of the artery clamped in both ends is now considered as last case. Table 5.5 illustrates the first 20 natural frequencies, and results coming from 1D models are compared to those from 3D FE analyses.

Accordingly to the test, two modal shapes obtained via 1D LE-CW (Component-Wise) model are illustrated in Fig. 5.4. In the end, the MAC (modal assurance criterion) test between the 1D-CW proposed model and the 3D-solid one is depicted in Fig. 5.5, to further underline the correcteness of the analysis. The MAC is usually employed to represent the degree of consistency (linearity) between two different modal vectors (see [124, 125]), and it reads:

$$\mathrm{MAC}_{ij} = \frac{|\{\phi_{A_i}\}^T\{\phi_{B_j}\}|^2}{\{\phi_{A_i}\}^T\{\phi_{A_i}\}\{\phi_{B_j}\}\{\phi_{B_j}\}^T} \tag{5.1}$$

Mode	Solid	LE	EBBT	TBT	N=1	N=4	N=8	N=10
1	133.63	134.12	246.26	170.22	164.04	155.92	141.34	139.44
2	138.06	138.85	259.15	174.24	170.15	147.86	146.53	144.32
3	235.41	236.73	-	-	251.93	249.43	244.67	243.45
4	247.65	258.78	-	-	-	-	-	331.14
5	256.51	258.83	598.93	349.94	339.49	316.54	285.33	278.51
6	270.22	272.26	633.59	361.64	351.67	301.34	295.71	290.05
7	309.85	310.97	-	-	373.61	368.84	356.66	349.72
8	311.76	325.77	-	-	-	-	-	-
9	319.54	329.08	-	-	-	611.04	478.45	462.58
10	340.83	348.22	-	-	-	-	-	-
11	342.64	354.95	-	-	-	617.55	501.94	478.91
12	385.71	390.33	-	-	-	644.86	434.66	414.72
13	387.44	396.67	-	-	-	-	-	-
14	393.04	397.51	-	-		-	-	-
15	400.98	409.27	-	-	-	-	585.31	547.56
16	425.57	440.64	-	-	-	-	-	-
17	432.91	438.87	-	-	-	493.22	478.35	478.92
18	434.25	443.75	-	-	-	711.92	566.41	510.85
19	441.07	451.96	-	-	-	-	-	-
20	442.76	448.23	-	-	-	-	-	535.37

Table 5.5: Natural frequencies (Hz) of the clamped-clamped atherosclerotic plaque.

(a) Mode 1

(b) Mode 6

Fig. 5.4: Representative mode shapes of the atherosclerotic plaque; CW model.

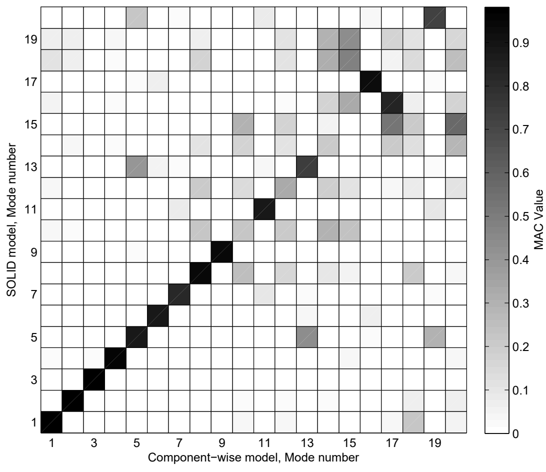

Fig. 5.5: Modal Assurance Criterion (MAC) between 3D FEM solution and LE model.

Material	Young Modulus E, GPa	Poisson ratio ν
Ti-6Al-4V	110.00	0.32
Cobalt-Chromium alloy	220.00	0.30
Feldsphatic Porcelain	61.20	0.19
Gingiva	19.60×10^{-3}	0.30
Bone	14.70	0.30

Table 5.6: Mechanical properties of the materials used in the study of the dental implant.

where $\{\phi_{A_i}\}$ is the i^{th} eigenvector of model A, while $\{\phi_{B_j}\}$ is the j^{th} eigenvector of model B. This criterion considers values from zero (for no consistent correspondence), to one (for a consistent correspondence). According to results obtained, the following comments can be pointed out:

- Even if classical and lower-order TE models are able to predict the bending frequnecies, these can't manage with modal shapes includind section deformations.
- Conversely, the LE-CW model is suitable on reproducing 3D-like results, concerning both vibration modes and natural frequencies. Some slight differencies (approximately 10 Hz) of frequencies are visible at high-frequency levels, as shown in Table 5.5, however this is balanced by the strong computational efficiency of CUF with respect to 3D models.

5.1.2 Dental Prosthesis

Dental prostheses have been deeply studied in literature since many years. These works firstly proposed guidelines and standards for robust and life-long implant, thanks to the analyses on materials and loads. In this section, instead, will be provided and assessed, novel models, from the mechanical point of view, for the static and free vibration response of this fundamental biostructure.

A transversal section of the considered model is exposed in Fig. 5.6(a), in which the main dimensions are given. The properties of the materials of the implant are collected in Table 5.6. Namely, Ti-6Al-4V alloy is commonly used for implant fixture and abutment, cobalt-chromium alloy for metal framework and feldsphatic porcelain for occlusal part. Table 5.6 also defines the mechanical features of the gingiva and bone, which will be consider for a second case.

Figure 5.6 shows the model taken into account. Concerning the load condition, a masticatory force of 118.2 N in the angle of approximately 75° to the occlusal plane has been considered, according to other published works.

As done for the atherosclerotic plaque, classical and refined TE and LE beam theories are employed for static and free vibration analyses. Namely, Euler-Bernoulli Beam Theory (EBBT), Timoshenko Beam Theory (TBT) and CUF till to the

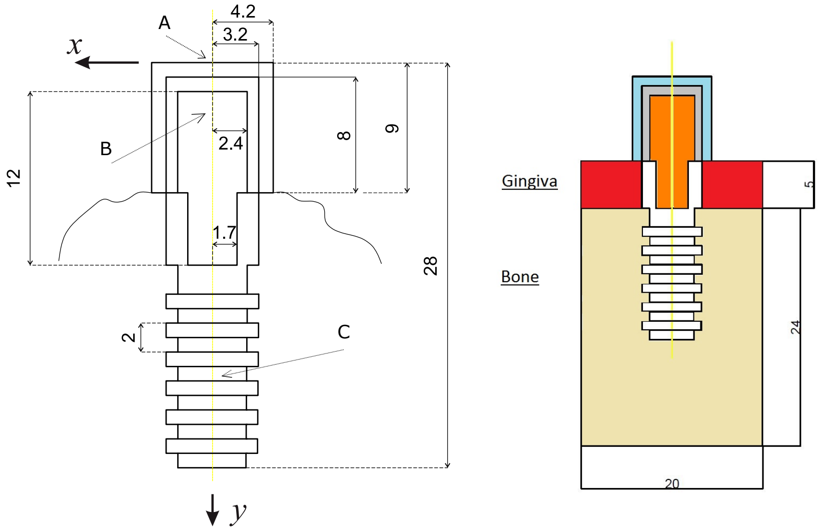

(a) Dental Prosthesis Geometry (b) Prosthesis and Gingiva

FIG. 5.6: Dental Implant. Geometry (a) and implant in gingiva (b)

16th-order refined TE models are adopted; LE models, instead, make use of the Lagrange functions to describe the cross-section kinematics, within the CW framework. Every CUF models include 24 cubic 1D FEs along the y-axis, to provide convergent results. The 3D solid FE models are developed within the NASTRAN commercial software.

5.1.2.1 Static Analysis

The initial situation takes into account the cantilever boundary condition (the base is fixed) and only the implant, without human bone and gingiva, is considered. Table 5.7 presents the values of axial and transverse, u_y and u_z, displacement components of the prosthesis under the masticatory load. The numerical values are exposed for various locations over the implant domain, and these are indicated by letters A, B, and C.As shown in Fig. 5.6(a), the point A is corresponds to the loading point and belongs to the porcelain region; points B and C are located at $y = 3.75$ mm and $y = 22$ mm and are in correspondance of the metal framework and of the implant fixture, respectively. The same table also shows the total number of degrees of freedom (DOFs) for each model employed. Here, special attention is paid to the potentiality of LE, that make use of a CW description of the kinematics, with 16 or 36 L9 polynomials, and to higher-order TE models for accurate results of displacement field. Figure 5.7 highlights this aspect, by illustrating the comparison of the 1D and 3D models deformed configuration. The stress vector is also analyzed in terms of the accuracy of the solution. In particular, compression and shear stresses, respectively σ_{yy} and σ_{yz}, are computed in two locations along the implant domain (points B and C as yet mentioned) and enlisted in Table 5.8. By these tests, it is possible to state that EBBT, TBT and lower-order TE models cannot predict accurately the displacement/stress field of the

Model	$u_y^A \times 10^2$	$u_y^B \times 10^3$	$u_y^C \times 10^3$	$u_z^A \times 10^2$	$u_z^B \times 10^2$	$u_z^C \times 10^3$	DOFs
Classical beam models							
EBBT	-0.797	0.910	-0.590	-4.760	-3.892	-3.410	219
TBT	-0.797	0.910	-0.590	-4.825	-3.953	-3.590	365
Refined TE beam models							
N=1	-0.797	0.910	-0.590	-4.825	-3.953	-3.590	657
N=4	-0.978	1.010	-0.780	-5.827	-4.780	-4.190	3285
N=8	-1.016	1.030	-0.780	-6.045	-4.955	-4.330	9855
N=12	-1.027	1.030	-0.800	-6.134	-5.029	-4.390	19929
N=16	-1.035	1.040	-0.820	-6.172	-5.061	-4.410	33507
Component-wise LE models							
16LE	-1.442	1.040	-0.440	-6.219	-5.099	-4.430	9903
36LE	-1.028	1.030	-0.800	-6.127	-5.022	-4.370	26595
3D NASTRAN model							
Solid	-1.064	1.040	-0.830	-6.330	-5.190	-4.470	118368

TABLE 5.7: Displacements components mm measured at three different points of the cantilever implant.

(a) CW model

(b) 3D NASTRAN model

FIG. 5.7: Deformed states of the cantilever implant subjected to the masticatory force.

biostructure considered. As a further case study, the human jawbone, made of bone and gingiva, is additioned to the previous model as depicted in Fig. 5.6(b). As before, the masticatory force insists on the implant and the bottom section is clamped. Only LE-CW models are employed among the CUF models for two main reasons: i) LE describe better the kinematics and the geometry complex structures as this; ii) LE allows to impose paricular boundary conditions. Stress results are collected in Table 5.9. In particular, point D is located in the titanium abutment at $y = 5.5$ mm; E is related to a position in the gingiva at $y = 11.5$ mm; and F regards a point of the bone at $y = 30.5$ mm. Table 5.9 shows representative stress values according to the CUF-based beam model and the 3D FEM model. Figure 5.8 shows the deformed configuration of the total model. Moreover, Fig. 5.9 exposes the axial stress field in correspondence to the bone region, and at the midspan length, in which the connection between the prosthesis and the jawbone is evident.

The static analysis here carried out suggests:

Model	σ_{yy}^B	σ_{yy}^C	σ_{yz}^B	σ_{yz}^C
Classical beam models				
EBBT	-3.8742	-6.3379	-0.0010	-0.0016
TBT	-3.8742	-6.3379	-0.9647	-1.6027
Refined TE beam models				
N=1	-3.8742	-6.3379	-0.9647	-1.6027
N=4	-3.0357	-6.1978	-1.1452	-3.6212
N=8	-3.0178	-6.8915	-1.1334	-2.1038
Component-wise LE models				
36LE	-2.9558	-5.9619	-1.1363	-2.0221
3D NASTRAN model				
Solid	-3.0031	-7.0980	-1.1514	-2.2007

TABLE 5.8: Stress components, in MPa, measured at two different points of the cantilever implant.

Model	σ_{yy}^D	$\sigma_{yy}^E \times 10^3$	σ_{yy}^F	σ_{yz}^D	$\sigma_{yz}^E \times 10^3$	$\sigma_{yz}^F \times 10^3$
52LE	-2.02	-2.01	-0.42	-0.59	-2.26	5.81
Solid	-1.97	-1.92	-0.42	-0.64	-2.19	5.46

TABLE 5.9: Stress components (in MPa) measured at three different points of the dental implant with gingiva and bone.

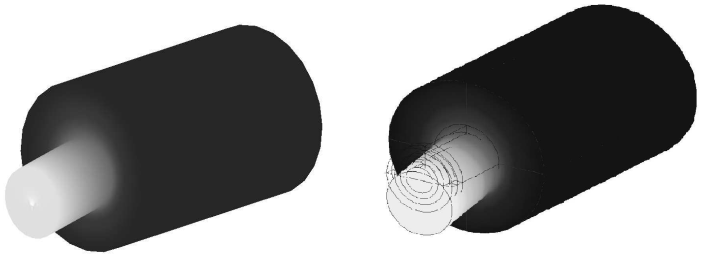

(a) CW model (b) 3D NASTRAN model

FIG. 5.8: Deformed states of the dental implant with gingiva and bone.

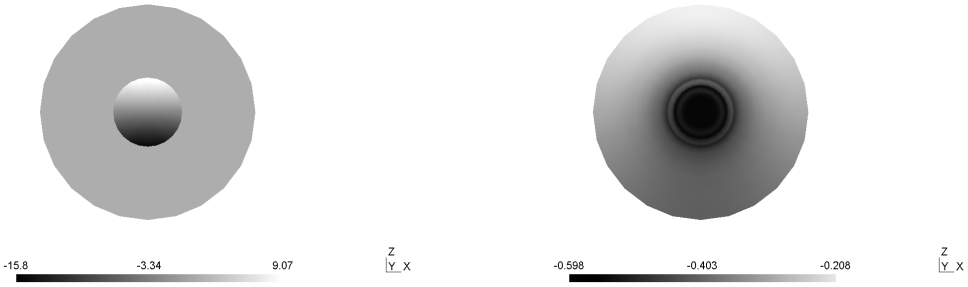

(a) $y = 11.5$ mm (b) $y = 30.5$ mm

FIG. 5.9: Cross-sectional stress distribution (σ_{yy}, MPa) at the implant/bone (a) and bone (b) regions of the dental implant; CW model.

	Classical models		Refined TE			Component-wise LE		3D NASTRAN
Mode	EBBT	TBT	N=4	N=8	N=12	16LE	36LE	Solid
1	3965.15	3923.86	3568.11	3504.73	3478.72	3475.14	3481.85	3425.49
2	3965.15	3923.86	3568.11	3504.73	3478.74	3475.14	3481.85	3425.49
3	32433.55	29938.09	16410.06	16121.71	16047.48	16036.42	16029.23	16110.40
4	32433.55	29938.09	27761.70	27345.98	27205.19	27188.46	27213.56	27057.82
5	42529.07	42529.07	27761.71	27345.99	27205.19	27188.46	27213.57	27057.84
6	103394.59	85576.67	40171.04	39745.53	39588.58	39614.69	39609.81	39358.11
7	103394.59	85576.67	80168.17	79180.83	78856.99	78768.19	78795.07	78669.59
8	171762.92	148591.54	80168.20	79180.86	78857.01	78768.19	78795.38	78669.62
9	188578.58	148591.55	91871.75	90542.57	90221.70	90141.91	90100.98	90526.15
10	188578.59	171762.92	138344.74	136721.92	136164.44	135990.48	135974.07	135398.00
11	286659.60	216227.25	138344.78	136721.97	136164.49	135990.48	135976.33	135398.00
12	288447.87	216227.26	161735.77	160105.42	159683.80	159503.76	159446.00	159640.60
13	288447.88	283319.15	164241.16	162841.80	162352.75	162369.15	162322.57	162038.70
14	373792.71	283319.15	199983.86	197202.74	196317.07	196338.53	196177.06	195249.20
15	488979.41	286659.60	207556.83	204387.10	203717.14	196338.53	196185.05	195249.20

Table 5.10: Natural frequencies (Hz) of the cantilever dental implant (see Fig. 5.7).

- Solutions obtained through one-dimensional models regarding the stress and the displacements are in accordance with those coming from 3D FE models.
- Due to the non-local properties of LE, it is possible to deal with particular boundary conditions and multi-material structures.
- The CW models are able to describe efficiently, the mechanical behaviour of complex dental systems including prostheses, gingiva, and bone.
- The higher-order 1D models can be considered as an interesting tool to substitute more popular tools as 3D FEM, for a better understanding of these complex biostructures.

5.1.2.2 Free Vibration Analysis

In addition to the staic test explained above, free-vibration analysis is performed and discussed hereinafter. Table 5.10 assembles the first 15 natural frequencies obtained through various 1D CUF models. Again, the 3D FE model is used to reference solution.

For clarity purpose, the natural frequencies computed are presented in the histogram in Fig. 5.10. Additionally, some representative modal shapes are shown in Fig. 5.11. Namely, two flexural modes (Mode 1 and Mode 10) and two axial modes (Mode 3 and Mode 9) are represented in this figure. Finally, for a quantitative verification of modal shapes obtained via CUF beam models and those captured through 3D FEM analysis, the Modal Assurance Criterion (MAC) is used and illustrated in Fig. 5.12. The modal analysis allows to formulate some comments, resumed as follows:

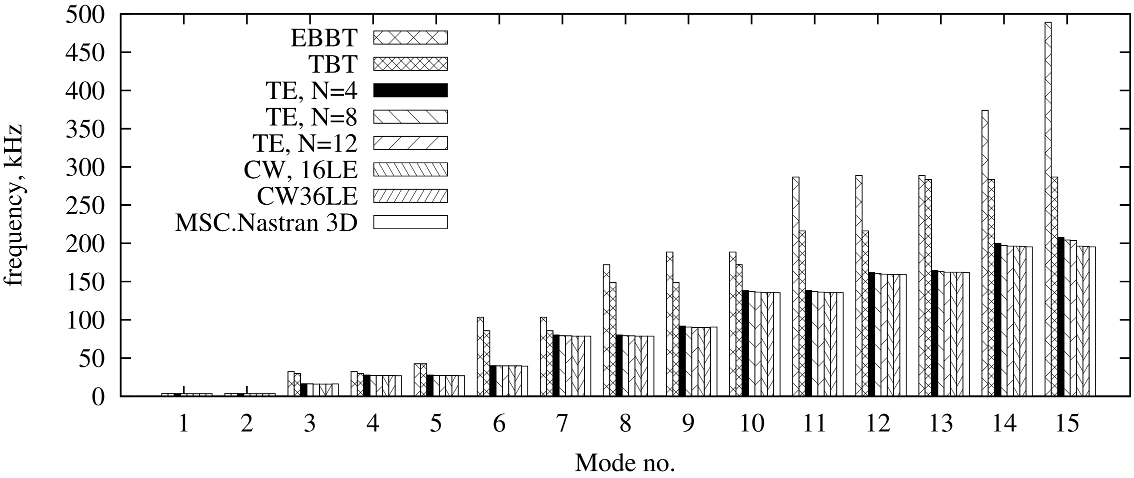

FIG. 5.10: Natural frequencies of the dental implant vs. numerical model adopted.

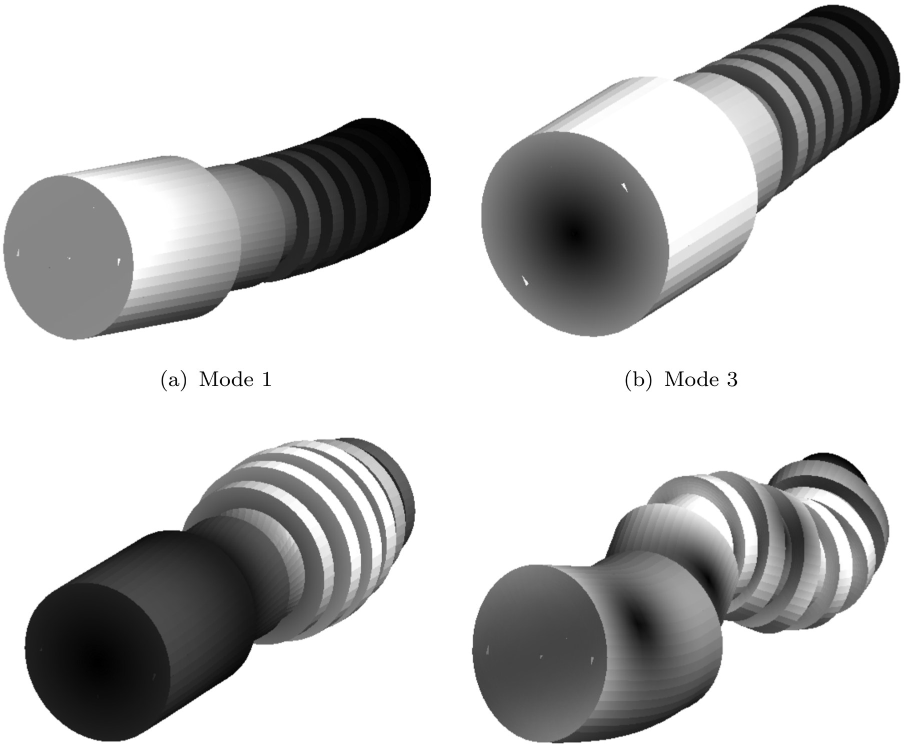

(a) Mode 1

(b) Mode 3

(c) Mode 9

(d) Mode 10

FIG. 5.11: Representative mode shapes of the dental implant; CW model.

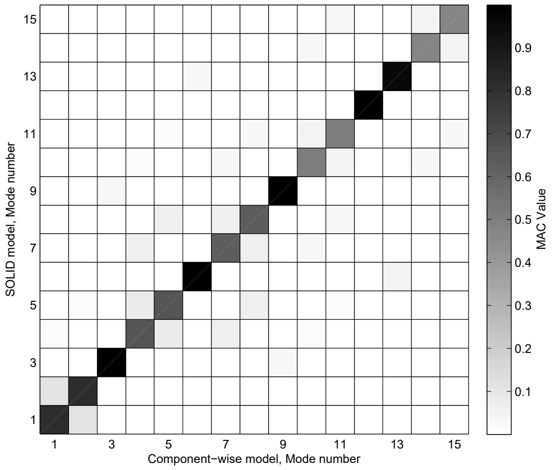

FIG. 5.12: MAC matrix of the eigenvectors from traditional 3D FEM solution and 36LE CW model.

- All beam models, can detect correctly the first bending mode, including classical and lower-order. Nonetheless, when high frequencies are taken into account, these models provide inexact results as evident in Fig. 5.10,
- By the contrast, higher-order TE models and LE beam models are able to predict very precisely the modal features of the dental prostesis, approaching to more complex 3D solid solutions.
- In particular, as demonstrated also by the MAC test (Fig. 5.12), CW models show a enhanced capabilities with a reasonable computational effort.

5.2 Structural Mechanics, Physical Nonlinearity

In this section, the extension to nonlinear problems of 1D CUF eplained in Section 2.5 is assessed through some numerical examples. Namely, a lumbar vertebra, an Achille's tendon and portions of arteries are taken into account as typical bio-application with physical nonlinearities. Nonlinear static computational tests are here performed for the description of the mechanical properties of these structures, and, the results coming from various 1D models and are verified by the comparison with commercial softwares.

5.2.1 Static Analysis: Lumbar Vertebra

The first numerical example of this section is related to the investigation of the nonlinear mechanic behavior of a lumbar vertebra. The spine is an anatomic structure composed by 24 articulated vertebrae. Each of these, includes the Vertebral Body, the Intervertebral Disc and the Facet Joint. The loads are supported by the vertebral bodys, and these are the subject of this example. Vertebral fractures are the most common type of osteoporotic fracture, [126], and are associated with increased morbidity and excess mortality. A vast literature has been developed over the last years for a better understanding of the frecture risk. The fundamentals of the biomechanics of the lumbar spine were described by Koreska et al. [127] and a poroelastic FE model has been presented by Wu and Chen [128]. Currently, one of the most popular method to analyze the vertebral strenght is the combination of FEA and Quantitative Computed Tomography (QCT) scan and different works based on this methodology have been proposed recently [129, 130, 131]. Studies have found that QCT-based FEA can provide good predictions of vertebral stiffness and strength, however, other values as deformation field or failure progression are less clear and the method needs to be adjusted by the measure of the Bone Mineral Density (BMD) [132, 133]. This method provides good results but, however, requires long procedures and expensive computational efforts, above all when particular costitutive models are assumed.

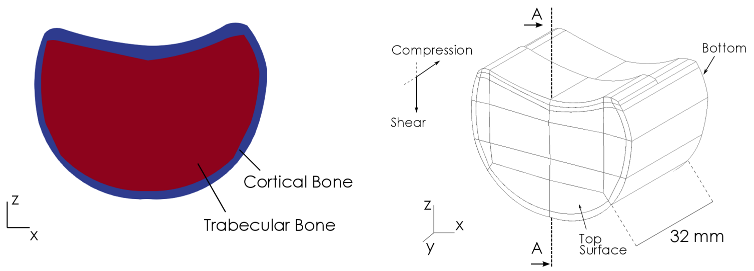

(a) Different Materials (b) Geometry

Fig. 5.13: Lumbar vertebra. Materials subdivision (a) and geometry (b)

Tissue	E	ν
Cortical Shell	330	0.25
Trabecular Core	17.5	0.25

Table 5.11: Materials properties of the lumbar vertebra. The Young's modulus is expressed in MPa.

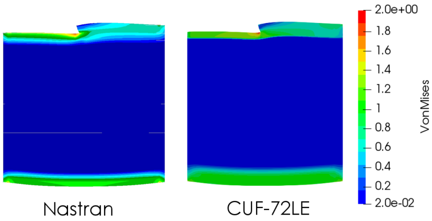

Fig. 5.14: Von Mises stress comparison between 72LE-20B4 CUF model and 3D NASTRAN model, in MPa. Linear compression analysis. A-A cross-section.

The purpose of this analysis is to propose a new approach to handle material nonlinearities of biostructures trough the use of the CUF. In particular, the mechanical behaviour of a lumbar vertebral body under nonlinear regime is investigated, from a qualitative standpoint. Two different load conditions are taken into account (axial compression and shear), and different results coming from the proposed methodology are compared to those obtained via the commercial 3D tool NASTRAN. The isotropic material properties in Table 5.11 and the overall geometries in Fig. 5.13 are taken from [128]. The cross-section of the model has been discretised using different set of Lagrange elements (nLE), while concerning for the FE scheme, cubic lagrangian B4 finite elements have been employed.

The compression analysis has been setted by imposing a displacement equal to 0.1 mm on the top surfaces of the vertebra. Results coming from linear compression analysis are summarised in Table 5.12. The stress values obtained by CUF are in agreement with those coming from 3D solution, as confirmed also in Fig. 5.14.

Model	σ_{vM}	$\sigma_{xx} \times 10$	$-\sigma_{yy}$	NDOF
NASTRAN				
3D Solid-1	2.15	4.08	2.27	151830
10-B4 Elements				
48LE	1.80	3.60	2.00	18465
72LE	1.90	3.70	2.20	27591
20-B4 Elements				
48LE	2.00	4.10	2.20	36285
72LE	2.00	4.10	2.20	54231

Table 5.12: Linear compression analysis. Results from 1D CUF models and 3D solution in section A-A. Values are in MPa.

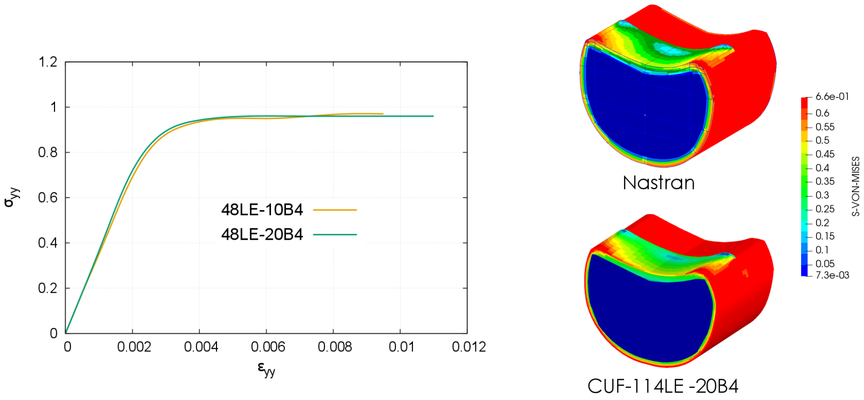

(a) Stress-Strain Curves (b) von Mises Stress

Fig. 5.15: Nonlinear compression analysis. Stress-strain curves comparison between two 1D CUF models (a) von Mises stress contour plots comparison between best 1D model and solid model (b). Values are in MPa.

In order to take into account the material nonlinearities of the bones, the elastic-perfect plastic von Mises failure criterion can be assigned to the bones, [128, 134, 135, 136]. In this case, the same displacement has been imposed and the post-yelding behaviour has been investigated. The equilibrium paths of two different CUF models is illustrated in Fig. 5.15(a), and the contour plot of the von Mises stress obtained at the end of the analysis is shown in Fig. 5.15(b). By increasing the mesh along the beam axis, a greater value of deformation is obtained and as expected, the solution is more stable. The results from the nonlinear static analysis are resumed in Table 5.13, in which values of axial stress σ_{yy}, transversal stress σ_{xx} and plastic equivalent strain $PEEQ$ are reported. In the Table 5.13, the 1D results approach those coming from 3D solid solution, although the discrepancy in terms of the DOFs. The quality of the solution increases with the axial discretization, as reported also in the convergence plot shown in Fig. 5.16. The plastic behaviour of

Model	$\sigma_{xx} \times 10$	$-\sigma_{yy} \times 10$	PEEQ$\times 10^3$	NDOF
NASTRAN				
3D Solid-1	3.46	9.10	9.12	151830
3D Solid-2	3.56	9.06	10.30	419343
10-B4 Elements				
48LE	3.40	9.70	7.90	18465
72LE	3.40	9.70	7.80	27591
114LE	3.40	9.70	7.80	43413
20-B4 Elements				
48LE	3.80	9.60	9.40	36285
72LE	3.80	9.70	9.30	54231
114LE	3.80	9.60	9.30	85353

Table 5.13: Nonlinear compression analysis. Results from 1D CUF models and 3D solution in section A-A. Values of stresses are in MPa.

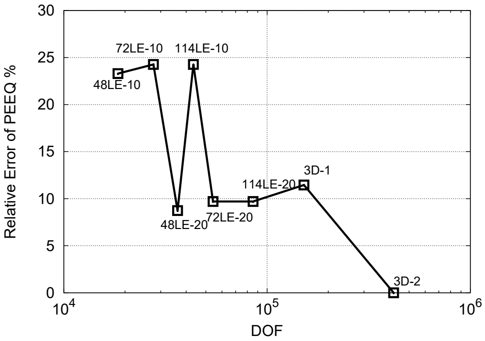

FIG. 5.16: Relative error of the plastic equivalent strain. Numbers 10 and 20 indicate the number of finite elements used along the beam axis.

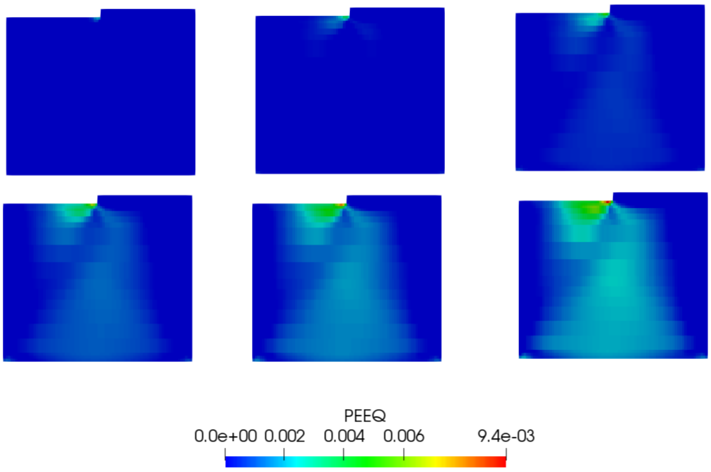

FIG. 5.17: Propagation of the equivalent plastic strain along the A-A cross-section. The top-left image represents the 50 % of load. Nonlinear compression analysis.

the lumbar vertebra is exposed in Fig. 5.29, in which the trend of the equivalent plastic strain is reported. As expected, the plastification starts at 40/50 % of the total stress and then propagate all allong the vertebral body.

Shear test The second load case is based on the displacement of the top surface along the z direction. As before, the displacement imposed is equal to 0.1 mm and the bottom surface is clamped. The solution was accomplished stepwise, through the adoption of Newton-Raphson numerical scheme. The von Mises equivalent stresses obtained from 1D and 3D models are in Fig. 5.18. In this case, the shear stress σ_{yz} was also evaluated and the results obtained by the different models are shown in Table 5.14. As for the compression load case, the value of stresses obtained via CUF models in Table 5.14 present accurate results. Although the dramatic reduction in term of degrees of freedom, even the less refined model shows reasonable results. By the contrast to the previous load case, models with more Lagrange elements on the cross-section provide better results compared to those refined along the beam axis. This is also confirmed by the convergence plot exposed

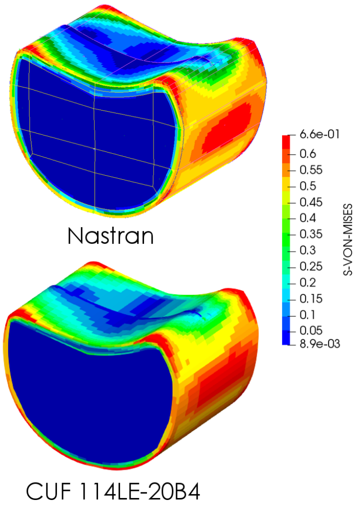

Fig. 5.18: Nonlinear shear analysis. Von Mises stress contour (in MPa) plots comparison between most refinied 1D model and solid 3D solution.

Model	$\sigma_{xx} \times 10$	$-\sigma_{yz} \times 10$	PEEQ $\times 10^3$	NDOF
NASTRAN				
3D Solid-1	2.07	3.75	3.07	151830
3D Solid-2	2.20	3.75	3.40	419343
10-B4 Elements				
48LE	2.40	3.80	2.00	18465
72LE	2.30	3.80	2.10	27591
114LE	2.30	3.80	3.40	43413
20-B4 Elements				
48LE	2.50	3.80	2.70	36285
72LE	2.40	3.80	2.70	54231
114LE	2.40	3.80	3.30	85353

Table 5.14: Nonlinear shear analysis. Results from 1D CUF models and 3D solution in section A-A. Values of stresses are in MPa.

in Fig. 5.19. The computational approach here exposed in the description of the mechanical nonlinear behaviour of a lumbar vertebra presents some advatages can be resumed as follows:

- The 1D CUF models are able to describe accurately the stress and the strain fields in linear and nonlinear regime, when compared to 3D solution.
- The present approach allows to handle multi-material nonlinear components with ease and provide accurate results with a reasonable computational cost.

5.2.2 Static Analysis: Achilles Tendon

An Achille's tendon portion under monoaxial load has been considered as a second numerical example of this section. The tendons work under axial tension, and they

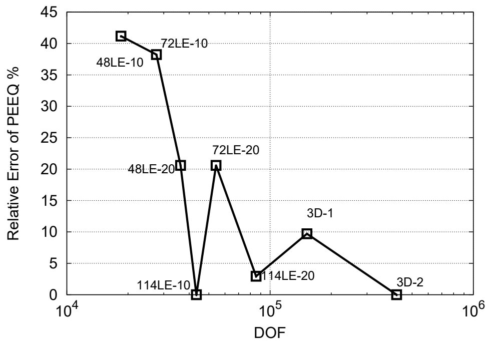

Fig. 5.19: Relative error of the plastic equivalent strain. Numbers 10 and 20 indicate the number of finite elements used along the beam axis. Nonlinear shear analysis.

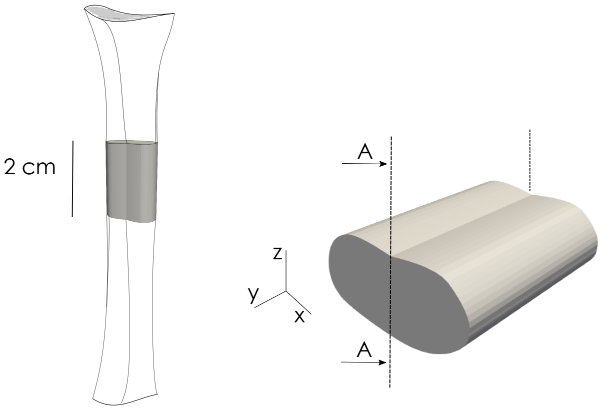

Fig. 5.20: The Achille's Tendon geometry

can resist to a high level of load; the human tendons usually present a stress-strain curve divided ideally into three parts, the toe, the linear and the plastic region. In this work the attention has been focused on the plastification zone of the tendons (see Fig. 5.20(a)), that is suitable within the nonlinear CUF framework presented in Section 2.6. It is important to underline that the von Mises failure criterion implemented along the CUF, is not usually used for soft tissues like this. The aim of the example hereinafter, is, indeed, to demonstrate the computational efficiency of the technique, paying less attention on the physical aspects of the problem. A portion 2 cm long of the tendon, that can be considered with a uniform cross-section, has been taken into account, as in Fig. 5.20(b). The material presents an elastic modulus E=800 MPa, a Poisson coefficient ν=0.33, and an isotropic hardening has been considered as post-yield behavior. Information about the loads and geometries come from the work of Shim et al. [137]. Other experimental works as [138, 139, 140], confirm how the tendon starts to fail when the equivalent von Mises stress is close to 100 MPa. In this example, a displacement controlled nonlinear analysis has been carried out to predict the mechanical behaviour of the tendon. Different Lagrange models (LE) have been employed for the analysis, using 10 or 20 cubic finite elements were used for the axial mesh. The results of this analysis are enlisted in Table 5.15, in which the 1D CUF model is compared

% Load	$\sigma_{vM} \times 10^{-7}$ Pa	PEEQ $\times 10^{2}$	$\sigma_{xx} \times 10^{-7}$	$\sigma_{yy} \times 10^{-8}$	DOF
CUF-10 B4					
56 LE	9.21	2.42	6.14	1.26	23157
124 LE	8.93	1.86	6.24	1.28	49941
CUF-20 B4					
56 LE	9.38	2.75	6.84	1.31	45567
124 LE	9.56	3.11	7.24	1.37	98271
3D NASTRAN					
3D-1	9.06	1.56	4.43	1.14	82623
3D-2	9.25	2.16	5.09	1.20	354474
3D-3	9.47	2.79	5.70	1.28	627003

TABLE 5.15: Nonlinear static analysis of the Achille's Tendon: values of different 1D CUF and 3D NASTRAN models. Values are in MPa

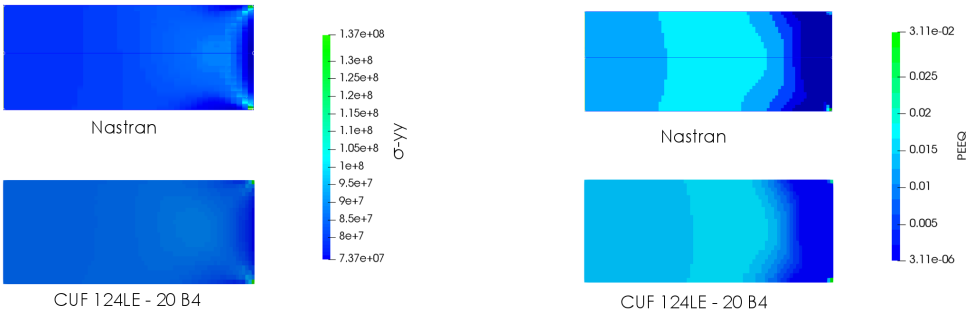

(a) Longitudinal σ_{yy}

(b) Equivalent Plastic Strain PEEQ

FIG. 5.21: The Achille's Tendon nonlinear analysis: Comparison between 1D CUF and 3D NASTRAN models of σ_{yy} (in MPA) and PEEQ, at longitudinal cross-section A-A.

to a full 3D Solid FE solution obtained via NASTRAN commercial tool. The stress/strain field obtained through both models are comparable, as eveident in Fig. 5.21, in which the equivalent plastic strain (PEEQ) and the σ_{yy} are plotted. At σ_{vM}=85 MPa the plastification starts, and the trend of the PEEQ (inelastic equivalent strain) is plotted in Fig. 5.22(a). The axial displacement is also shown in the same figure, whereas the Fig. 5.22(b) illustrates a 3D sketch of the Achille's tendon elongation at the end of the computational test.

Figure 5.23 represents the convergence analysis of the relative error of σ_{vM} and PEEQ of the various model respect to the reference solution (3D-3). The figure shows how the increasing of the longitudinal mesh improves the 1D solution better than increasing the number of LE elements on the cross-section. In addition, the higher-order CUF models show results closer to reference solution than the less refined 3D models.

Let now consider a second Achille's tendon with different cross-section geometry (Type 2). Table 5.16 shows the comparison of σ_{vM}, σ_{yy} and PEEQ between Type 1 and Type 2. The stress values are quantitatively similar, even increasing the

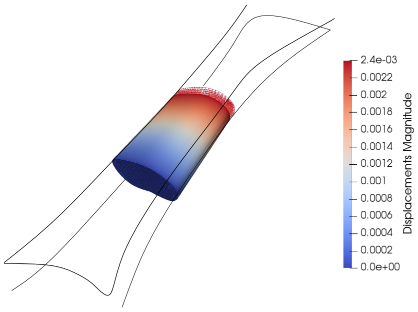

(b) 3D-Sketch

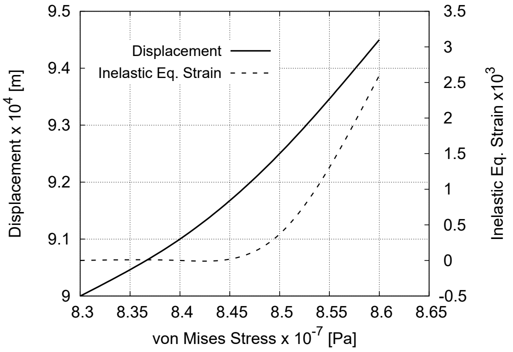

(a) Plastic Strain and Displacement trends

Fig. 5.22: The Achille's Tendon nonlinear analysis: trends of displacements and inelastic eq. strain (a); 3D sketch of the model at the end of the analysis. The displacement values are in [mm].

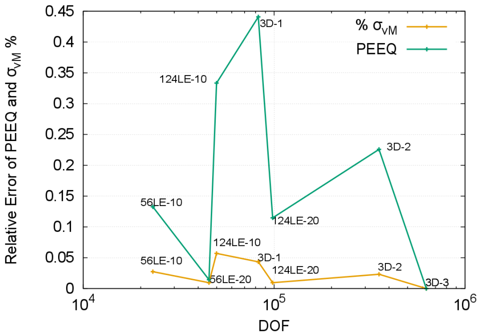

Fig. 5.23: Relative error of the plastic equivalent strain and von Mises stress. Nonlinear shear analysis.

discretization.

However, the geometrical differences influnce the yielding location, as in Fig. 5.24. In particular, Type 1 fails on the top, while Type 2 fails on the bottom. This figure represents the moment in which the plastification appears, at $\sigma_{vM} \approx 85$ MPa.

5.2.3 Static Analysis: Artery, healty and diseased

The capabilities of the nonlinear CUF framework have been also tested in a case of multi-material application with a very particular geometry, as the atherosclerotic plaque seen in Section 5.1.1. As known, the tissues around the lumen, Media (M) and Fibrous Cap (FC), are more solicited in case of severe stenosis, [141],

TABLE 5.16: Comparison between two Achille's tendons with different geometries. Values of Von Mises stress, longitudinal stress and plastic equivalent strain.

	Type 1			Type 2		
Iteration	$\sigma_{vM} \times 10^{-7}$ Pa	$\sigma_{yy} \times 10^{-8}$	PEEQ $\times 10^2$	$\sigma_{vM} \times 10^{-7}$ Pa	$\sigma_{yy} \times 10^{-8}$	PEEQ $\times 10^2$
10 BE	9.21	1.26	2.42	8.93	1.17	1.87
20 BE	9.38	1.31	2.75	8.96	1.22	1.92

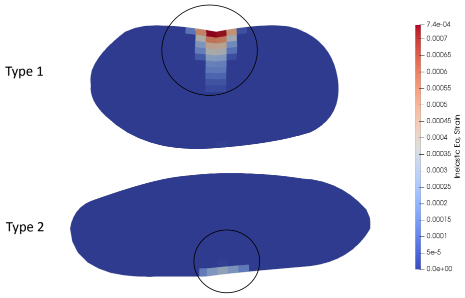

FIG. 5.24: Plastification starting point of Achille's tendons with different cross-section geometry.

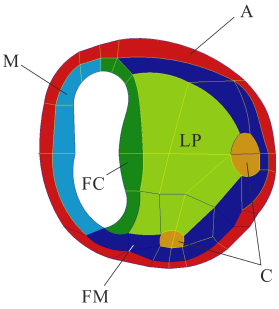

FIG. 5.25: The atherosclerotic plaque and its materials.

and therefore, were chosen to be modeled as nonlinear, as the examples above. For these materials, an ideal elasto-perfect plastic constitutive model is adopted, according to the theory exposed in Section 2.6. Likely the tendon case, the purpose of this analysis is only to verificate the efficiency of the methodology, since other constitutive models should be accounted for this kind of tisssues. The other components of the arteria are the Adventitia layer (A), the Fibrotic Media (FM), the calcified parts (C) and the Lipid Pool (LP), [121], as it is depicted in Fig. 5.25, and are modeled as linear isotropic. The portion of artery considered has a length of 40 mm along the y-axis, is clamped in both extremities, and is subjected to an internal pressure of 180 mmHg [123]. All the refined models were modeled using 10 B4 elements for the axial discretization, and the numerical model has been implemented in FORTRAN environment. Table 5.17 enlists the values of von Mises stress and principal stress obtained from the full linear (L) and nonlinear (NL) models; as expected, the NL model shows more relevant stress values with respect to the L model, under the same pressure load, as evident in Fig. 5.26. The solutions obtained by 1D models were compared to ones coming from NASTRAN commercial tool, and these are enlisted in the Table 5.18. Figure 5.27 shows the

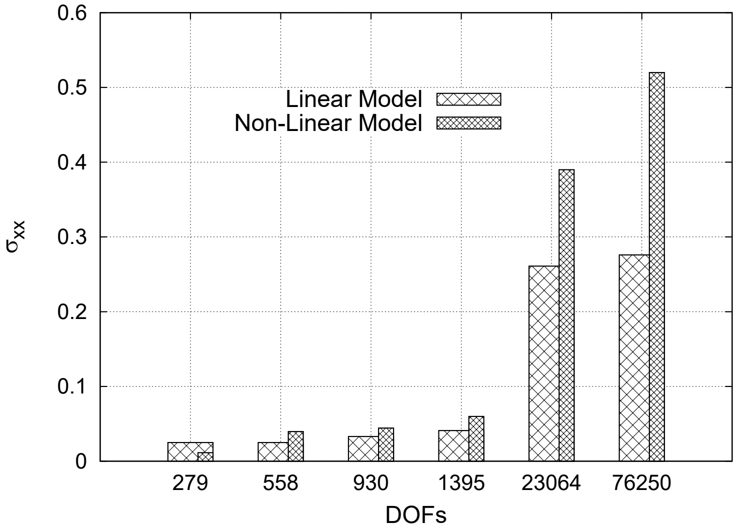

Fig. 5.26: Principal stress along x direction. Comparison between linear and nonlinear models.

Table 5.17: Comparison between linear and nonlinear models. Values of σ_{xx} and von Mises stress.

	Linear Models		NonLinear Models		
Model	$\sigma_{xx} \times 10^2$	$\sigma_{vM} \times 10^2$	$\sigma_{xx} \times 10^2$	$\sigma_{vM} \times 10^2$	DOF
	MPa	MPa	MPa	MPa	
TE					
N = 1	2.50	0.91	1.14	2.24	279
N = 2	2.50	0.99	3.97	3.20	558
N = 3	3.30	1.50	4.43	4.33	930
N = 4	4.10	2.70	5.90	4.69	1395
LE					
LE 55	26.10	30.20	39.00	4.80	23064
LE 191	27.60	28.00	52.00	4.80	76250

convergence analysis of the CUF models in compared to the 3D solution, according to the Eq. 5.2:

$$Error = \frac{|value_{3D} - value_{1D}|}{value_{3D}}\% \tag{5.2}$$

The maximum effort is located around the lumen, and this effect is well visible in Fig. 5.29 which plots the comparison of the inelastic equivalent strain obtained from CUF and 3D models. The results of this numerical application allow to observe the capabilities of one-dimensional CUF models in dealing with nonlinear materials. In particular, the refined models can predict the 3D-like effects and the stress/strain field of the biostructure and, moreover, they can reach a high level of accuracy with a drastic reduction of computational effort.

Diseased and Non-Diseased Artery

TABLE 5.18: Comparison between linear and nonlinear models. Values of von Mises stress of 1D CUF and 3D NASTRAN models.

Model	$\sigma_{vM} \times 10^2$ - L	$\sigma_{vM} \times 10^2$ - NL	DOF
	MPa	MPa	
TE			
N = 1	0.91	2.24	279
N = 2	0.99	3.20	558
N = 3	1.50	4.32	930
N = 4	2.70	4.69	1395
LE			
LE 55	30.20	4.80	23064
LE 191	28.00	4.80	76250
NASTRAN			
3D - 1	20.60	4.80	158178
3D - 2	25.70	4.80	748056

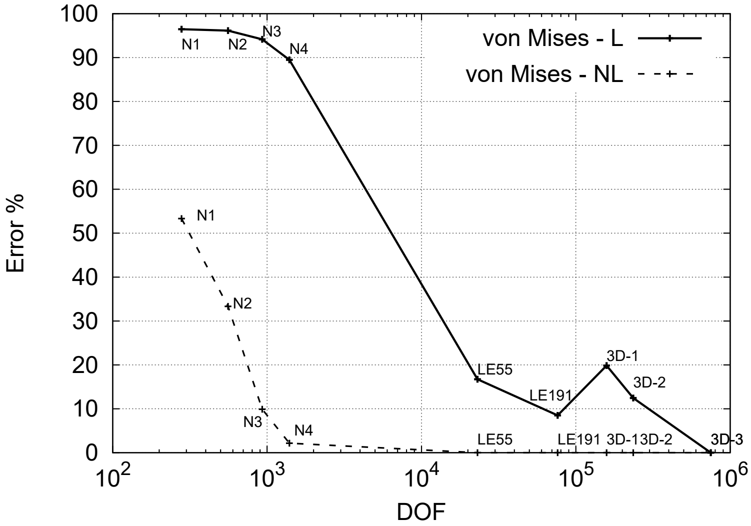

FIG. 5.27: Convergence analysis of von Mises stress for linear and nonlinear models respect to NASTRAN 3D solutions.

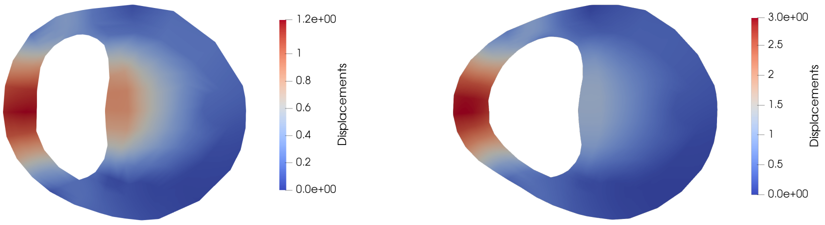
1.2e+00
1
0.8
0.6
0.4
0.2
0.0e+00
Displacements
3.0e+00
2.5
2
1.5
1
0.5
0.0e+00
Displacements

(a) Linear

(b) Non Linear

FIG. 5.28: Displacement ditribution, in mm, on the midspan cross-section: linear model (a) nonlinear model (b). LE55 models.

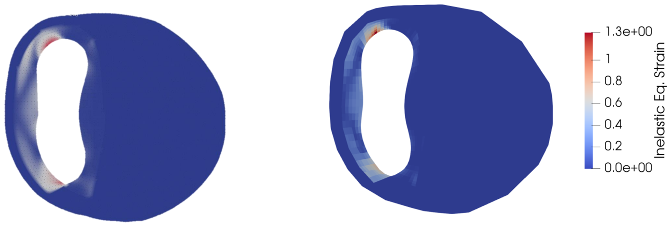

(a) 3D NASTRAN (b) LE191

Fig. 5.29: Measure of inelastic equivalent strain of CUF models. 3D NASTRAN (a) and 1D CUF model (b).

	Diseased		Healthy	
% Load	**u** mm	PEEQ	**u** $\times 10^2$ [mm]	PEEQ
20%	0.27	0.04	0.49	-
40%	0.72	0.16	0.98	-
60%	1.40	0.31	1.50	-
80%	2.20	0.46	2.00	-
100%	3.00	0.61	2.50	-

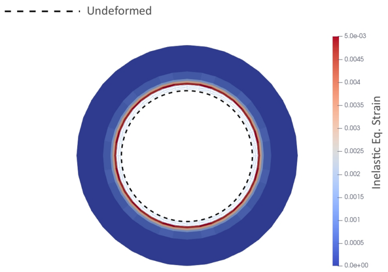

Fig. 5.30: Comparison between diseased and non-diseased artery portion. Values of displacement in mm, **u**, and PEEQ on the left; on the right, the cross-section of the deformed non-diseased case with a blood pressure five times greater than nominal.

To make the results closer to the biomedical reality, the artery affected by severe stenosis previously analyzed is compared to a non-diseased vessel in this section. Just to remind, the formation of the atherosclerotic plaque is due to the accumulation of lipid and to the growth of calcified parts inside the vessel; without any pathology, the healthy portion of the artery presents only three layers of materials, the Adventitia (A), the Media (M) and the Intima (I). According to the CUF nonlinear framework, the inner layers have been modeled as isotropic ideal elasto-plastic. By applying the nominal blood pressure of 180 mmHg, the values of displacement and equivalent strain PEEQ were computed for the arteries, and these are enlisted in Table 5.30. 55 Lagrange elements (LE55) describe the cross-section geometry of the diseased artery, as in the previous example. As shown in Table 5.30, under a nominal level of blood pressure, the healthy artery does not present any plastic strain, and the values of displacement are significantly lower than ones related to the diseased vessel. This result helps us to point out how the inner materials are not solicited in case of the normal condition of blood pressure.

By increasing five times the pressure (ideally), the artery without any pathology present plastic strain as well, and this effect is shown in Fig. 5.30.

5.3 Computational Fluid Dynamics

The one-dimensional CUF for fluid-dynamics as described in Section 3 is assessed in this section. A number of refined models are compared with analytical solutions, whenever possible, or with finite volume results obtained with commercial software tool. The first case study consists in the evaluation of fluid parameters in the case of Poiseuille flow in a cylindrical pipe. The second numerical assessment confirms the validity of the technique in presence of different boundary conditions, whereas the third subsection deals with the study of Stokes flow in a square-section cylindrical pipe.

The length of the pipes considered is $L = 6$ m and the radius is $r = 1$ m in the case of the circular section. In case of square cross-section, the side is $s = 2$ m, if not differently specified. All the subsequent analyses present a homogeneous Dirichlet boundary condition on the lateral surface Γ_D^{Lat} (no-slip condition), and a homogeneous Neumann boundary condition on the outlet section Γ_N^{Out}. Conversely, the inlet section Γ_D^{In} presents, according to each case study considered, different nonhomogeneous Dirichlet boundary conditions. No body forces are applied to the fluid and thus $\mathbf{f} = \mathbf{0}$ is taken into account in the Stokes equations. The fluid has a viscosity ν equal to $10^{-2} m^2/s$ satisfying the condition of $Re \ll 1$ for the velocity profiles introduced afterwards. If not differently specified, CUF models are discretized with 10 1D FEM elements, which ensure convergent results. For the sake of clarity, the following nomenclature has been used to denote models with different kinematic assumptions:

- $nLt^U - nLt^P$: Model with uniform Lagrange Expansion; n is the numeber of elements used for the cross-section description and t is the type of elements used for velocity and pressure, i.e. four-nodes L4 or nine-nodes L9 elements.
- $N^U - N^P$: Taylor models with order N^U and N^P for the velocity and pressure fields respectively.

As an example, with $N^U 4 - N^P 2$ it is denoted a Taylor model with a fourt order expansion for the velocity field and a second order expansion for the pressure distribution; on the other hand, with $5L9^U - 5L4^P$ is denoted a model with five L9 for the description of the velocity and five L4 for the pressure field.

5.3.1 The Poiseuille Flow

The first case analyzed is the Poiseuille flow in the cylindrical pipe considered. The Poiseuille flow is the condition achieved by a flow in cylindrical pipe when the Reynold number is very small. For this kind of flows, the analytical solution exists and, represents a good benchmark to assess the 1D CUF theory for fluid-dynamics.

In the Poiseuille flow, the velocity $\mathbf{u}$ does not change along the centerline y. In particular, the axial velocity component u_y traces a paraboloidal distribution where

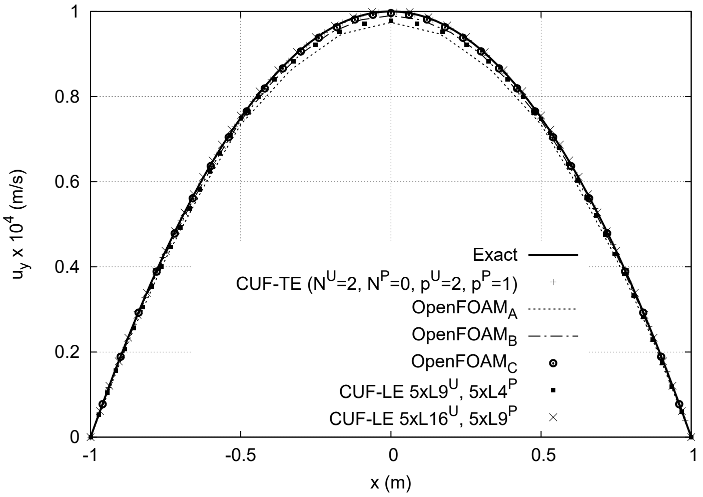

FIG. 5.31: Poiseuille flow velocity profile at $y = 3$ m, $z = 0$.

the pick value $u_{y_{max}}$ ocoincide with the centre of the cross-section. To reproduce this kind of sitiation, the following non-homogeneous Dirichlet boundary condition is imposed at the inlet cross-section Γ_D^{in}:

$$\begin{cases} u_x = 0 \\ u_y = 10^{-4}\left(1 - x^2 - z^2\right) \qquad \text{on } \Gamma_D^{\text{in}} \\ u_z = 0 \end{cases} \tag{5.3}$$

According to the Poiseuille analytic solution [142], the paraboloidal inlet velocity profile, which is depicted in Fig. 5.31, should remain constant over the pipe axis. As visible in Fig. 5.31, where the Poiseuille profiles coming from different models are shown, an approximation of second-order for $\mathbf{u}$ and a zero-order for p are sufficient to detect the right solution in the case of TE. On the other hand, LE models need 5 cubic cross-section subdomains for velocity and 5 quadratic polynomials for the pressure to predict a good solution, as listed in Table 5.19.

The finite volume models are built in OpenFoam [143] and they present three different meshing. Namely, the model OpenFOAM_A was modeled with 2640 finite volumes (132x20 mesh, where 132 stands for the number of volumes on the cross-section and 20 is the discretization along the y-axis), OpenFOAM_B has 13600 (340 x 40)elements, and OpenFOAM_C present 108800 (1368 x 80) elements.

The pressure inside the pipe decreases constatly along the tube and does not depend on the cross-section coordinates. In addition, one can notice that the outlet value is equal to zero, exactly as demonstrated by the Poiseuille analytical theory, see Fig. 5.32.

Quadratic to cubic Finite Elements (i.e., B3 and B4) were employed for the FE mesh along the y axis. The adoption of the family of expansion is importantant for the analysis stability. In particular, equal polynomial degree finite elements, for both velocity and pressure, are in most of the cases unstable, providing spurious

Model	$e_p(\%)$	$e_{u_y}(\%)$	$DOFs$
OpenFOAM			
OpenFOAM$_A$	-0.72	-2.56	10560
OpenFOAM$_B$	-0.25	-0.97	54400
OpenFOAM$_C$	0.21	-0.39	435520
CUF - TE			
N^U2, N^P0	-0.05	-0.05	389
CUF - LE			
$5L9^U, 5L4^P$	+1.83	-2.19	2493
$5L16^U, 5L9^P$	-0.03	+0.24	5361

TABLE 5.19: Inlet pressure and maximum axial velocity at y=3 in terms of percentage errors versus analytical solution for the Poiseuille flow. Comparison of OpenFOAM results with CUF results.

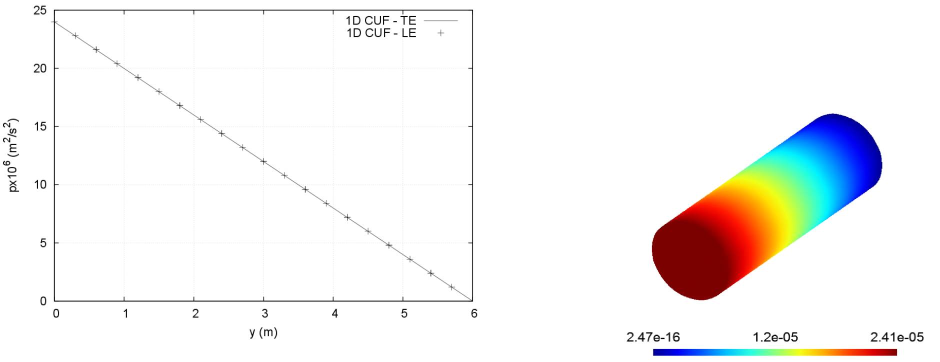

(a) Comparison between CUF-1D models

(b) 3D scheme of pressure trend in circular pipe

FIG. 5.32: Pressure trend comparison between LE and TE models along the longitudinal axis y (a), 3D scheme of the pressure trend of the Lagrange model $5L16^U$ - $5L9^P$, results are in m^2/s^2 (b). Poiseuille flow.

pressure modes. For the sake of completeness, a convergence analysis is provided; in particular, an investigation on the L^2 norm of relative error was performed. The convergence was first compared between TE and LE models, by varying the order of expansion over the section, see Fig. 5.33(a) . Then, as presented in Fig. 5.33(b), two specific LE models were considered, and the relative error by varying the FE meshes along the longitudinal axis was evaluated.

As Fig. 5.33(a) suggests, in the case of Poiseuille flow in circular pipes, the TE models are able to detect the correct solution without increasing the order of expansion, in contrast with LE ones. Regarding Fig. 5.33(b), a stability problem, and a consequent increasing of the error, is evident whenever the 1D elements for FE discretization of the y axis are the same for both the pressure and velocity.

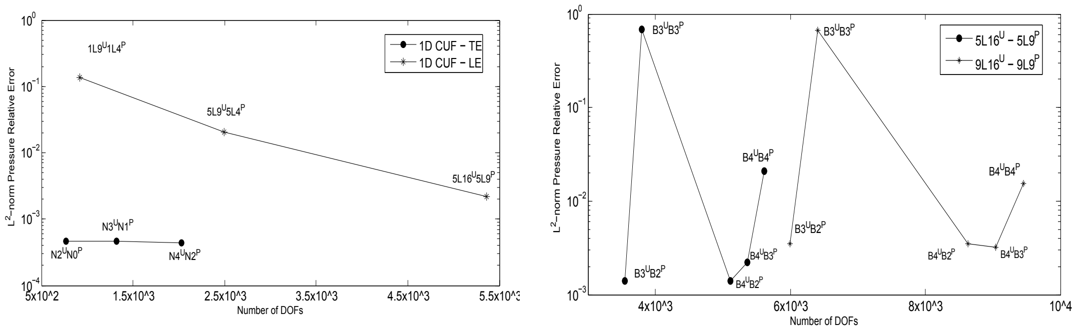

(a) Convergence analysis of TE and LE models (b) Convergence analysis of two specific LE models

FIG. 5.33: Trend of L^2 norm of pressure relative error. Convergence analysis of TE and LE models (a) and of two different Lagrange models (b).

5.3.2 Different Velocity Profiles at Inlet

The Poiseuille flow has been used to assess the 1D CUF models for Stokes fluid-dynamics; it is the most simple flow in a pipe, and the condition of a constant pressure over the section is commonly used by classical one-dimensional models for fluid-dynamics. In this section, the capabilities of the 1D CUF models are presented in the description of more complex flow. Thus, fourth-order and fifth-order velocity profiles are hereinafter introduced at the inlet cross-section and the results from 1D CUF models are compared with those obtained via OpenFoam. As first case, the following fourth-order velocity profile is enforced at the inlet cross-section Γ_D^{in}:

$$\begin{cases} u_x = 0 \\ u_y = 10^{-4}\left(1 - x^2 - z^2\right)^2 \qquad \text{on } \Gamma_D^{\text{in}} \\ u_z = 0 \end{cases} \tag{5.4}$$

Note that the flow is still axisymmetric and that the other boundary conditions remain the same as in the previous section. According to the considerations done before, the longitudinal mesh is kept different between velocity and pressure: 10 cubic B4 Lagrange elements for velocity and 10 quadratic B3 for pressure are employed.

Table 5.20 shows the maximum value of the pressure at the inlet and the maximum value of the axial velocity in the middle of the pipe. TE model with N^U6 and N^P4 provides convergent results, whereas LE model needs 9 cubic elements for velocity and 9 quadratic ones for pressure.

It is clear from Table 5.20 that both one-dimensional models, TE and LE, can approach the finite volume solution with a drastic reduction of degrees of freedom.

In the case of the fourth-order velocity inlet profile, u_y is still axisymmetric, but, it changes along the longitudinal axis y, as depicted in Fig. 5.34(a). In particular,

Model		$p \times 10^5 (m^2/s^2)$	$u_y \times 10^5 (m/s)$	$DOFs$
		OpenFOAM		
OpenFOAM$_A$		1.70	6.50	10560
OpenFOAM$_B$		1.79	6.53	54400
OpenFOAM$_C$		1.87	6.36	435520
		CUF-TE		
N^U	N^P			
8	7	1.86	6.66	6651
8	6	1.86	6.66	6403
6	5	1.86	6.66	4095
6	4	1.86	6.66	3909
4	3	1.79	6.66	2155
4	2	1.79	6.66	2031
		CUF-LE		
$5L9^U$	$5L4^P$	1.75	6.53	2493
$5L16^U$	$5L9^P$	1.82	6.67	5361
$9L16^U$	$9L9^P$	1.84	6.66	9045

TABLE 5.20: Maximum inlet pressure and maximum axial velocity at $y = 3$m. Comparison of OpenFOAM results with CUF results, fourth-order inlet velocity profile.

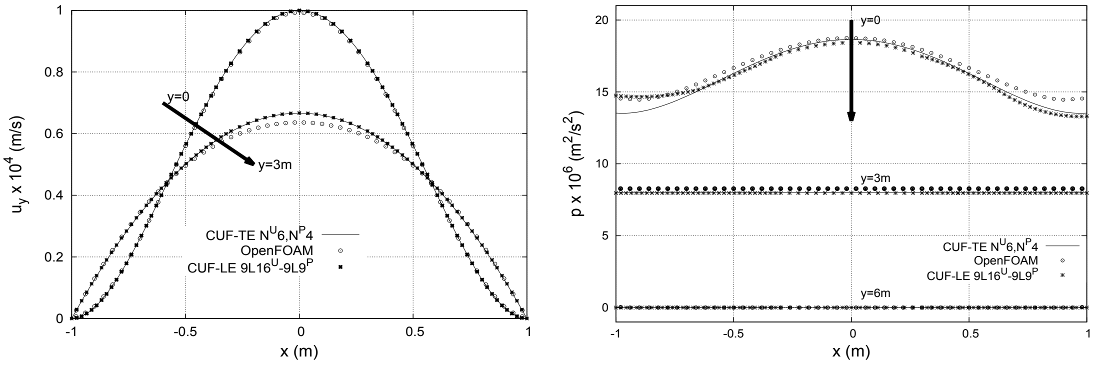

(a) Axial velocity variation over the different sections

(b) Pressure variations over the different sections

FIG. 5.34: Fourth-order inlet boundary condition. The profile for axial velocity u_y (a), and for pressure (b). Comparison of OpenFOAM results with CUF reuslts.

the velocity presents a *transition* area in which the profile moves from a 4^{th}-order to a 2^{nd}-order Poiseuille flow.

The behaviour of the pressure across the section is drawn in Fig. 5.34(b). Due to the inlet boundary condition, also the pressure trend presents a variation along the longitudinal axis; as expected, the pressure has an axisymmetric behaviour at the beginning of the pipe, and then tends to become constant over the section, approximately at 1/10 of the length of the cylinder.

As the fifth-order inlet velocity profile concerns, it is not axisymmetric. It means that the following Dirichlet non-homogeneous boundary condition was imposed on

Model		$p \times 10^6 (m^2/s^2)$	$u_y \times 10^5 (m/s)$	$DOFs$
		OpenFOAM		
OpenFOAM$_A$		7.20	2.43	10560
OpenFOAM$_B$		8.17	2.44	54400
OpenFOAM$_C$		9.08	2.35	435520
		CUF-TE		
N^U	N^P			
10	9	9.52	2.50	9823
8	7	9.48	2.50	6651
8	6	9.57	2.50	6403
6	5	9.23	2.50	4095
6	4	10.72	2.50	3909
5	4	10.80	2.50	3048
		CUF-LE		
$9L16^U$	$9L9^P$	9.19	2.50	9045
$20L16^U$	$20L9^P$	9.36	2.50	19818

Table 5.21: Maximum inlet pressure and maximum axial velocity at $y = 3$m. Comparison of OpenFOAM results with CUF results, fifth-order inlet velocity profile.

the first section of the pipe:

$$\begin{cases} u_x = 0 \\ u_y = 10^{-4}\left(1 - x^2 - z^2\right)\left(1/4 + xz + x^3\right) & \text{on } \Gamma_D^{\text{in}} \\ u_z = 0 \end{cases} \tag{5.5}$$

The meshes along the y-axis remain unvaried, as well as the other boundary conditions. As a consequence, the flow obtained through the first sections is no more axisymmetric and it is requested a higher-order expansion, as it is possible to verify in Table 5.21, which gives the maximum inlet pressure value and maximum axial velocity at mid-span.

The axial velocity profiles at various cross-sections till the mid-span (where the flow is fully developed) are depicted in Fig. 5.36. In this case the transition area is longer than the previous one faced for the fourth-order profile, as drown in Fig. 5.35. Nonetheless, the behaviour of velocity u_y gradually tends to the more natural condition of axial-symmetry, due to the outlet and lateral boundary conditions.

As expected, the pressure is not constant across the sections at the beginning of the pipe; it approaches gradually the constant profile typical of Poiseuille flow. First it becomes flat, then decreases linearly up to the outlet.

The following comments arise from these analyses:

- The different orders of velocity inlet profile represent an important assessment for the 1D CUF theory for fluid-mechanics due to its capability to predict the evolution of complex flows also when they are not axisymmetric.

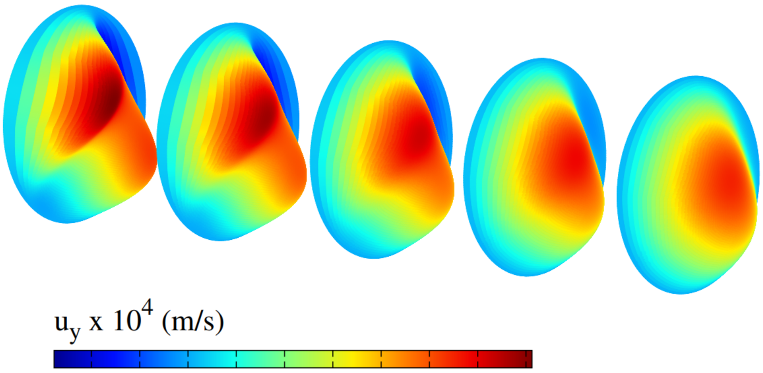

Fig. 5.35: 3D plot of axial velocity profile through the transition area in [m/s]. Fifth-order inlet boundary condition, TE model, $N^U = 6, N^P = 5$.

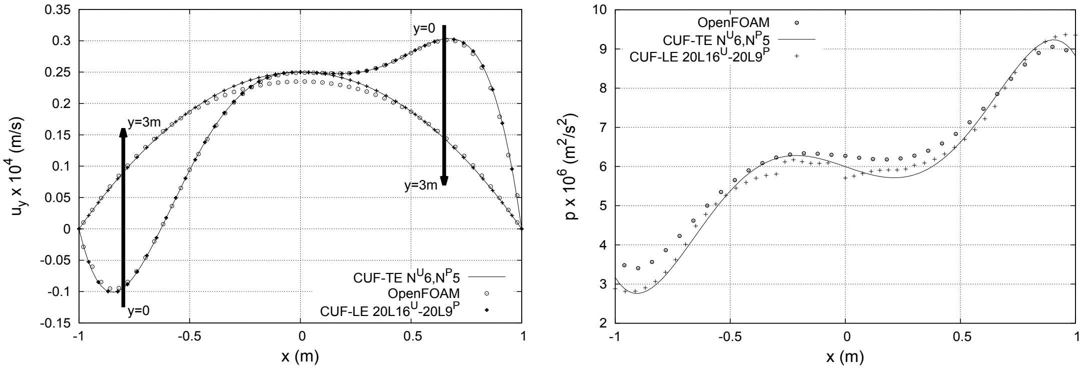

(a) Axial velocity variation over the different sections

(b) Pressure shapes across the inlet section

Fig. 5.36: Fifth-order inlet boundary condition. Transition of u_y axial velocity (a); pressure shapes across the inlet section(b). Comparison of OpenFOAM results with CUF results.

- In the case of high-order flows, as suggested by Tables 5.20 and 5.21, appropriate accuracy of LE would require more DOFs than comparable TE models for the considered analysis cases.
- As it is possible to verify in the Table 5.21, one-dimensional models allow for detecting the solution with a drastic reduction of the computational efforts, compared to finite volume solutions.

5.3.3 Square-section Pipes

Another numerical assessment aims at demonstrating the capabilities of LE CUF models to deal with complex and unconventional computational domains with ease. In particular, the flow through a square-section pipe have been evaluated, using LE one-dimensional models. The flow considered keeps the viscosity of the previous cases as well as the boundary conditions on the outlet and lateral surfaces. At the inlet section, a second-order velocity profile is enforced, the same used for the Poiseuille flow in the cylindrical pipe.

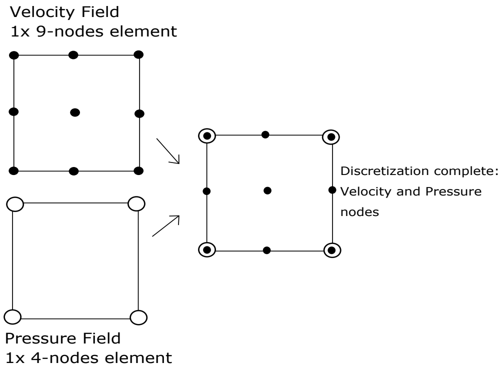

Fig. 5.37: Example of Lagrange elements across the section. 1xL9 for Velocity and 1xL4 for Pressure.

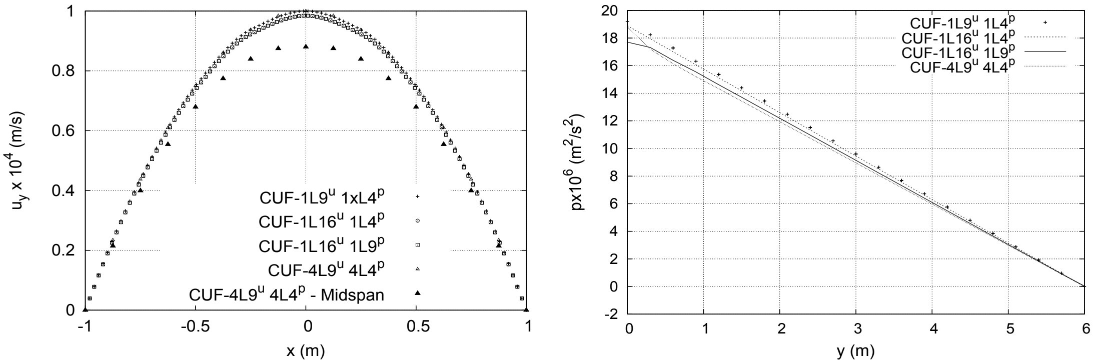

(a) Axial component of Velocity u_y of different models (b) Pressure behaviour across the longitudinal axis y

Fig. 5.38: Second-order flow in a square-section pipe. Parabolic behaviour of the axial velocity (a); decreasing pressure along the conduct (b).

As in other fluid-dynamics problems, velocity and pressure fields are described by different order polynomials; commonly, the pressure order is smaller than the velocity one, as shown in Fig. 5.37, which gives an example of LE modelling for the case under consideration. The first analysis consists of a comparison among schemes with different polynomial orders. Subsequently, some results about using the same order for pressure and velocity are presented.

According to Fig. 5.38(a), in which the axial component of velocity u_y is depicted, some aspects about the order of polynomials and the boundary effects are relevant. In fact, the case $1L16^U$ is not able to detect the maximum value of 10^{-4} imposed, probably due to its cubic nature. At the same time, the $1L9^U$ case can find the maximum imposed, but does not perceive the decrease of axial velocity detected by the $4L9^U$ model. This question is evident in Fig. 5.39(a,b,c), where u_y is drawn on yz plane. According to the this figure, the model with 4 Lagrange sub-domains is the only one presenting a decrease between inlet and midspan sections. As seen for the velocity, the pressure response depicted in Fig. 5.38(b) is affected by the boundary effects close to the inlet cross-section; nevertheless, each model presents a uniform decay along the conduct. While the order chosen for the velocity does

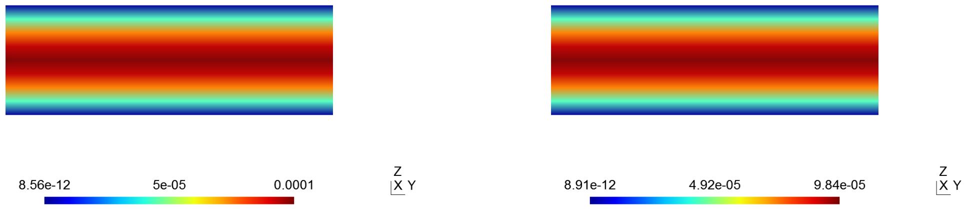

(a) $1L9^U$ - $1L4^P$ (b) $1L16^U$ - $1L4^P$

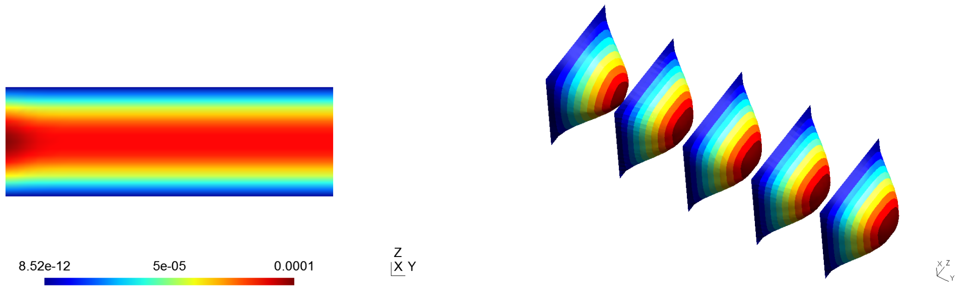

(c) $4L9^U$ - $4L4^P$ (d) $4L9^U$ - $4L4^P$ - 3D Plot

FIG. 5.39: Axial velocity u_y in square-section pipe. Comparison of three different models (a),(b),(c), values are in [m/s]; 3D plot of u_y of $4L9^U 4L4^P$ model (d).

not affect considerably the results, this is not true for the pressure field. For this reason, it is important to underline the necessity of keeping the pressure order smaller than the velocity one. When this condition is not satisfied, one can observe some stability problems concerning the pressure trend, see Fig. 5.40.

5.3.3.1 Instability

While the order chosen for the velocity does not affect considerably the results, this is not true for the pressure field. For this reason, it is important to underline the necessity of keeping the pressure order smaller than the velocity one. When this condition is not satisfied, one can observe some stability problems concerning the pressure trend, see Fig. 5.40.

As suggested by this figure, the choice of the expansion order across the section (Fig. 5.40(b)) and, of course, along the longitudinal axis (Fig. 5.40(a)), is an important parameter in fluid-dynamic analyses.

Due to this last section, we can confirm 1D CUF as an efficient and alternative tool for computational fluid-dynamics also in case of the non-circular section. This formulation allows to impose different velocity profile with ease, and offers a simple way to manage the boundary.

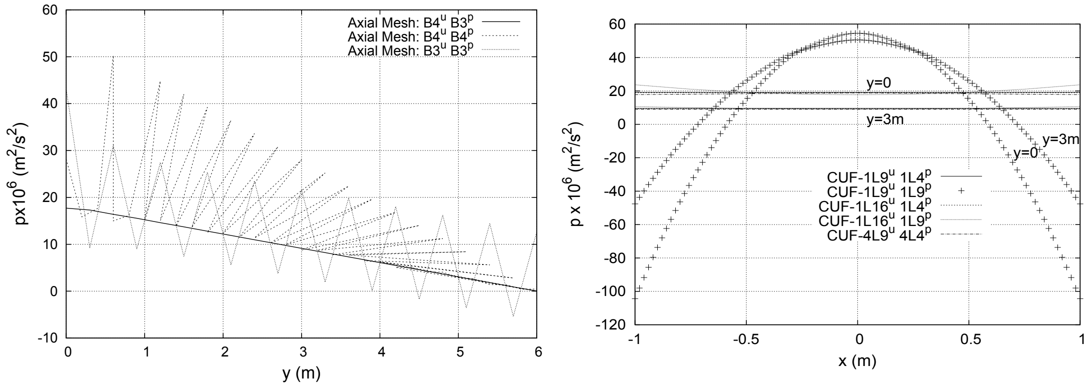

(a) Pressure trend along y-axis (b) Pressure trend across the section

FIG. 5.40: Pressure trend comparison: models with different FE order of the y-axis (a); models with different order of expansion across the section (b).

Input Data	Value	
Cross-section Inlet Area	8	m^2
Length Pipe	6	m
Kinematic Viscosity	0.01	m^2/s
Inlet Costant Velocity	0.0001	m/s

TABLE 5.22: Flow and geometry data.

5.3.4 Change section pipes

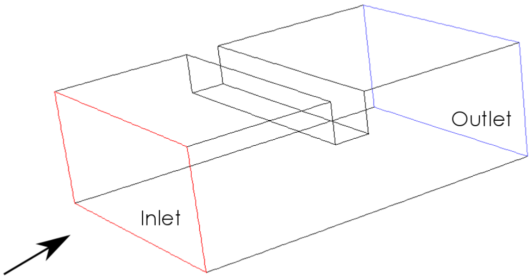

FIG. 5.41: Transversal narrowing conduct geometry.

In the framework of pipes with non-conventional geometries, this numerical example takes into account a rectangular cross-section pipe. In particular, a flow through a transversal narrowing conduct as in Fig. 5.41 has been considered. The flow keeps the kinematic viscosity of the previous examples, and the no-slip boundary condition is imposed at lateral walls. At the inlet cross-section is enforced a costant velocity, and the main data are resumed in Table 5.22. As in the other examples, the order of the Lagrange functions adopted for the description of the

Model	$P \times 10^2 [Pa]$	$u_y \times 10^4 [m/s]$	$DOFs$
	$10B4^U - B3^P$		
$12LE^{9,4}$	5.02	2.27	6166
$48LE^{9,4}$	5.78	2.49	21450
	$20B4^U - B3^P$		
$48LE^{9,4}$	5.81	2.48	41952
3D-FLUENT	5.96	2.46	1482240

TABLE 5.23: Maximum inlet pressure and axial velocity at $y = 3.0$m and $z = 0$m . Comparison of FLUENT results with CUF results, constant inlet velocity profile.

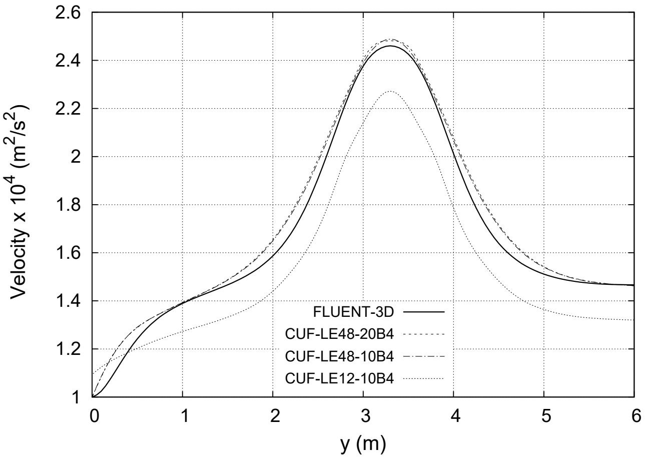

FIG. 5.42: Longitudinal velocity trends along the centerline of the pipe.

velocity and pressure field is different; in particular quadratic L9 and linear L4 have been employed respectively. Table 5.23 presents the results of the fluid-dynamic analysis coming from different models. In particular, the values of pressure at inlet and axial velocity at mid-span cross-section obtained via CUF models are compared to those obtained via 3D finite volume model designed in FLUENT. By increasing the number of Lagrange elements on the cross-section, it is possible to enhance the solution of the 1D models and to make them closer to the reference solution, as shown also in Fig. 5.42. In this figure, the axial components of the velocity along the centerline are shown. Among the 1D models, the more accurate result cames from the model with 20 B4 finite elements along the axis, although the difference with result obtained from the model with 10 B4 is not substantial. The quality of the results is shown in Fig. 5.43 where the velocty field distribution is depicted through the transversal and longitudinal plane, whereas in Fig. 5.44 the pressure field distribution is presented through the longitudinal plane. As expected, the velocity value increase as the narrowing gets coloser while the pressure decrease contemporanealy. These figure demonstrates how it is possible to obtain 3D-like accurate solution with a large computational cost saving.

CUF has been used for the analysis of incompressible, laminar and viscous fluids in rigid pipes. In particular, some higher-order 1D models for Stokes flows have been proposed. According to CUF, the primary variables of the flow (i.e. velocity and pressure) are expressed as arbitrary expansion of the generalized unknowns.

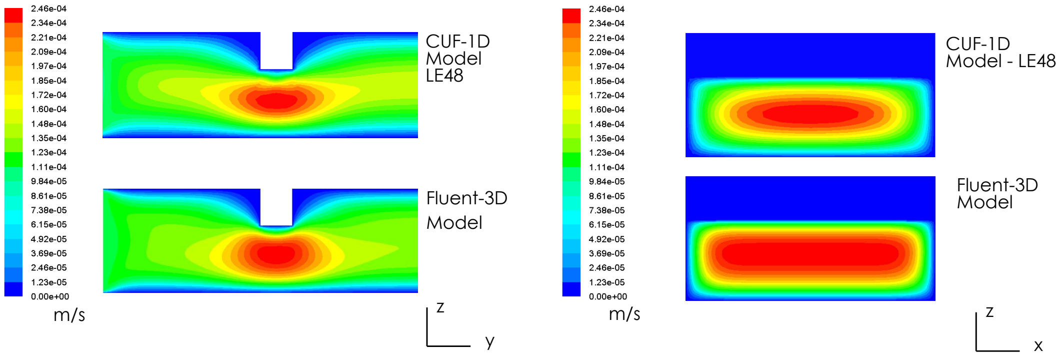

(a) Velocity distribution on yz-plane (b) Velocity distribution on xz-plane

FIG. 5.43: Comparison between the $48LE^{U,P}$ one-dimensional model with finite volume model. Longitudinal trend (a) and transversal distribution (b).

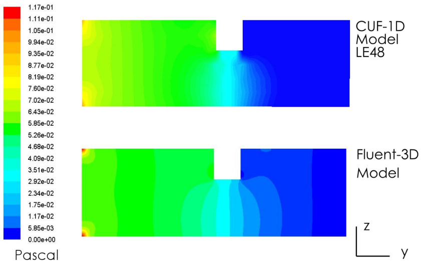

FIG. 5.44: Longitudinal pressure distribution on yz-plane. Comparison between the $48LE^{U,P}$ one-dimensional model with finite volume model.

By using these expanding functions on the cross-sectional plane, a unified finite element method has been developed straightforwardly. The case of Poiseuille flow has been taken into account as numerical assessment, and then more complex flows have been analyzed. In particular, Taylor expansion (TE) and Lagrange (LE) 1D models have been employed for the description of the flow in both circular and square section conduct. The results obtained from these 1D models have been compared with the analytical solution and with 3D numerical approximations obtained via finite volume software OpenFOAM.

The analysis here performed clearly underlines:

- LE and TE models based on CUF provide accurate results of velocity and pressure with respect to analytical solution.
- 1D models allow to obtain efficient results with lower computational costs compared with those obtained via 3D finite volume software.
- CUF represents an alternative tool to investigate the Stokes flow also in non-circular section tubes.

These promising preliminary results can be considered as a first step toward more advanced applications, like complex fluids and fluid-structure interaction.

5.4 Computational Fluid Dynamics with Node-dependent Kinematics

The section hereinafter shows the efficiency of the method explained in the Section 4, through some numerical examples. The refined models proposed are compared with the analytical solution whenever possible, or with solutions obtained by finite volumes tools. The first example aims to assess the NDK approach in the case of the Poiseuille flow in a cylindrical pipe. The present models have been than used to study flows with different inlet velocities distributions whereas the last example tests the node-dependent kinematics formulation in the case of square-section pipes.

All the examples consider a pipe with a length L of $6m$, a radius $r = 1m$ and, in case of square section, a side of $s = 2m$; the pipe always presents a homogeneous Dirichlet boundary condition at lateral walls and a homogeneous Neumann boundary condition at the outlet section. The inlet section presents some non-homogeneous Dirichlet boundary conditions, that have been specified for each case. No body forces are applied and the fluid has a viscosity, ν, equal to $10^{-2}m^2/s$ to satisfy the condition of $RE \ll 1$. All the cases hold a discretization of ten one-dimensional elements along the main axis, B3 for pressure and B4 for velocity. All the one-dimensional models considered hereinafter are implemented and solved in FORTRAN environment. The nomenclature adopted could result complicated, and it is slightly different from that used in previous section. Therefore, for the sake of clarity, the following nomenclature has been used to denote models with different kinematic assumptions:

- nLE^{t^U,t^P}: Model with uniform Lagrange Expansion; n is the numeber of elements used for the cross-section description and t is the type of elements used for velocity and pressure, i.e. four-nodes LE4 or nine-nodes LE9 elements.
- TE^{N^U,N^P}: Taylor models with order N^U and N^P for the velocity and pressure fields respectively.
- $TE/LE/TE$: NDK scheme with Taylor and Lagrange Expansions.

As an example, with $TE^{4,2}$ it is denoted a Taylor model with a fourt order expansion for the velocity field and a second order expansion for the pressure distribution. On the other hand, with $4LE^{9,4}/TE^{3,1}$ is denoted a model with a LE kinematics in a part of the domain, and a $TE^{3,1}$ models elsewhere.

5.4.1 Poiseuille flow analysis

The first numerical assessment takes into account the Poiseuille flow in a cylinder. Since the analytical solution is available, this simple application has been used to assess the NDK approach proposed in the present paper. In particular the results

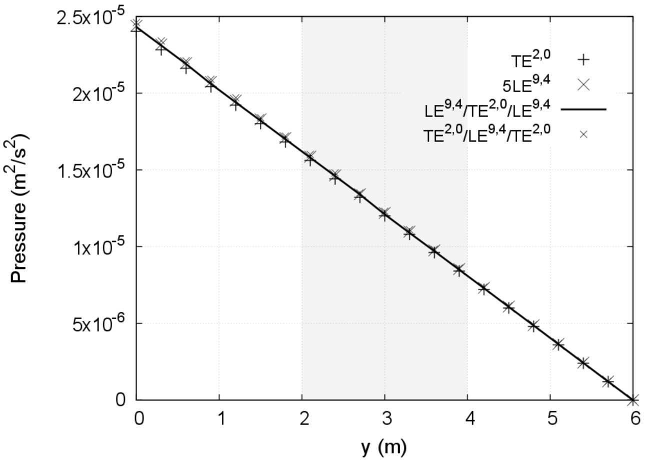

FIG. 5.45: Pressure trends of the Poiseuille flow. Comparison between constant and node-dependent kinematic one-diemnsional models. The gray part defines the region of domain in which NDK models change the kinematics.

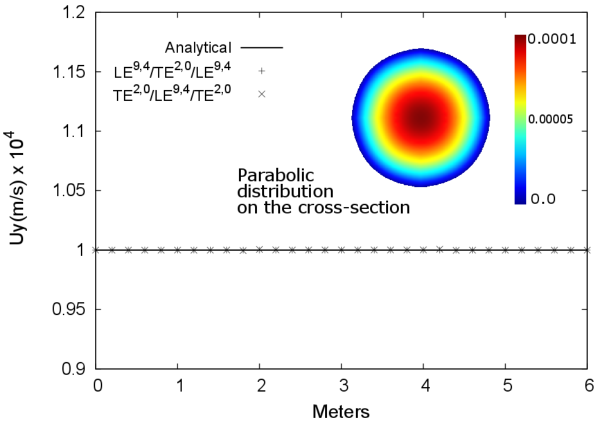

FIG. 5.46: Velocity trends of the Poiseuille flow. Comparison between constant and node-dependent kinematic one-diemnsional models.

obtained with the node-dependet kienmatic one-dimensional models have been compared with those obtained with constant kienmatic models and the analysical solution, [85, 142]. A parabolic distribution of velocity was enforced at the inlet, with $u_y = 10^{-4}$ m/s at the center of the section. Figure 5.45 presents the pressure behavior in the axis got from various onedimensional models, whereas in Fig. 5.46 one can see the 1D node-dependent kinematics model and the Poiseuille analytical model comparison with respect to the centerline velocity. The results clearly show that, even if the kinematic is modified along the duct, the 1D models predict very accurately the Poiseuille fsolution. In particular, as the Fig. 5.46 proposes, the models show the parabolic behavior of the u_y along the cross-section and can mantain it constant in the whole pipe, accordingly to the Poiseuille solution.

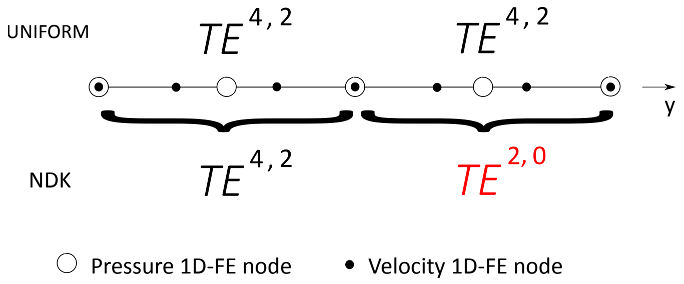

FIG. 5.47: Node-dependent kinematics scheme of fourth-order inlet velocity case. Changing of expansion order for velocity N^U and pressure N^P node-by-node.

5.4.2 Analysis of flow with complex inlet velocity profiles

The Poiseulle flow has been used to assess the one -dimensional node-dependent kinematics models. The natural decreasing of the pressure, as well as the parabolic distribution of the velocity, was not affected by the change of the kinematics along the duct. In this section, the advantages of the NDK method have been exploited to investigate flow with complex velocity profiles at the inlet cross-section.

The first example considered is a flow in a cylindrical pipe with a fourth-order Dirichlet boundary condition at the inlet. Equation 5.6 shows the three components of the velocity imposed at the inlet section, where u_y is the component parallel to the pipe axis.

$$\begin{cases} u_x = 0 \\ u_y = 10^{-4}\left(1 - x^2 - z^2\right)^2 \qquad \text{on } \Gamma_D^{\text{in}} \\ u_z = 0 \end{cases} \tag{5.6}$$

As seen in Ref. [85], it is necessary at least a $TE^{4,2}$ model to detect the distribution of the velocity across the inlet section. Since the flow tends to become parabolic moving away from the inlet section, it could be possible to decrease the expansion orders, as in Fig. 5.47, saving computational effort. Differently from the Poiseuille flow case, the pressure has not a complete linear decrease along the duct, that is the $N^P = 0$ is not sufficient in the area closest the inlet cross-section, as is evident in Table 5.24. Neverthless, the possibility to have more refined kinematic in the inlet area, allows to describe the pressure trend correctly as evident in Fig. 5.48, decreasing the computational effort as well. Figure 5.49 shows how the distribution of the axial velocity changes along the duct. In particular, the velocity moves from a 4^{th}-order curve to a 2^{nd}-order one (Poiseuille-like), and, due to this, it is not necessary to keep the expansion order $N^U = 4$ for the entire pipe. It is possible to decrease the expansion order from 4 to 2, without

Table 5.24: Values of pressure at inlet and midspan sections. Comparison of CUF-1D results. Fourth-order inlet velocity profile.

Model	$p(m^2/s^2)$ - Inlet	$p(m^2/s^2)$ - Midspan
$TE^{4,2}$	$1.79e-5$	$8.0080e-6$
$TE^{4,2}$ / $TE^{2,0}$	$1.78e-5$	$8.0079e-6$
$TE^{2,0}$	-510536	70.4931

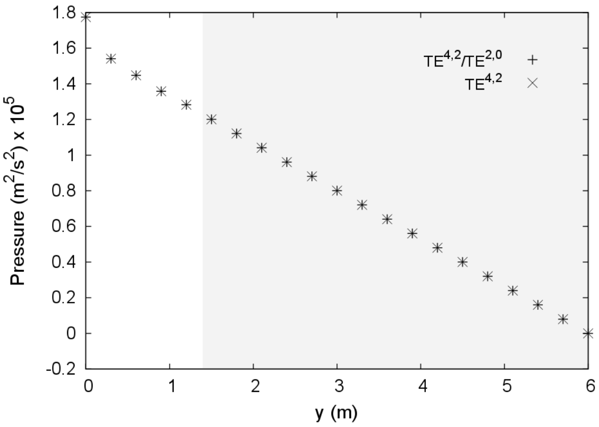

Fig. 5.48: Comparison of the presure path between uniform and NDK 1D CUF models. The gray area denotes the domain where the TE2,0 model has been used. Fourth-order inlet velocity profile.

any loss of accuracy, as evident in Fig. 5.49 where one-dimensional constant and node-dependent kinematic models are compared with OpenFOAM solutions. The primary advantage of the method here presented is in terms of computational costs, as shown in Table 5.25. In this table, the maximum values of pressure at the inlet and the maximum values of velocity at the midspan cross-section evaluated using different models are enlisted. As in Ref. [85], the reference solution was obtained using the CFD code OpenFOAM [143]. As the Table 5.25 suggests, the possibility to reduce the expansion order node-by-node does not affect the accuracy of the solution and allows a reduction of DOFs.

A non-simemtric Dirichlet boundary condition has been considered as second case. A fifth-order distribution of velocity is enforced at the inlet cross-section, according to the Eq. 5.7.

$$\begin{cases} u_x = 0 \\ u_y = 10^{-4}\left(1 - x^2 - z^2\right)\left(1/4 + xz + x^3\right) \qquad \text{on } \Gamma_D^{\text{in}} \\ u_z = 0 \end{cases} \tag{5.7}$$

The meshes along the y-axis remain unvaried, as well as the other boundary conditions. Since the inlet flow is no more axisymmetric, as shown in Fig. 5.50, the one-dimensional models need high-order expansions to describe the profiles of both

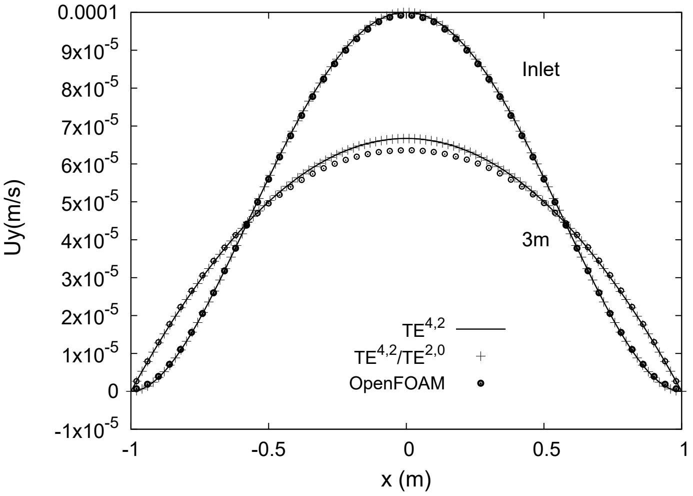

FIG. 5.49: Comparison of the velocity distribution between CUF-1D models and OpenFOAM results at inlet and midspan cross-section. Fourth-order inlet velocity profile.

TABLE 5.25: Maximum value of pressure at inlet y=0m and maximum axial velocity at midspan y=3m. Comparison among different 1D CUF results and OpenFoam solutions .Fourth-order inlet velocity profile.

Model	$p \times 10^5 (m^2/s^2)$	$u_y \times 10^5 (m/s)$	$DOFs$
	$OpenFoam$		
$OpenFOAM_a$	1.70	6.50	10560
$OpenFOAM_b$	1.79	6.53	54400
	TE		
$TE^{4,3}$	1.79	6.66	2031
$TE^{4,2}$	1.79	6.66	2031
	LE		
$5LE^{9,4}$	1.75	6.53	2493
$5LE^{16,9}$	1.82	6.67	5361
	NDK		
$TE^{4,2}$ / $TE^{2,0}$	1.78	6.66	852

velocity ($N^U = 6$) and pressure ($N^P = 5$), ([85]). Since the boundary conditions lead the flow to become Poiseuille-like, it can be convenient to analyze the model by using a node-dependent kinematic approach. The variation of the velocity profile is visible in Fig. 5.51, in which 1D models, with constant and node-dependent kinematic, are compared to the OpenFOAM solutions. The goodness of the results obtained is confirmed also numerically by the Table 5.26, in which the values of pressure at the inlet and velocity at the midspan are compared among different models. At the end of these analyses, it is possible to make the following comments:

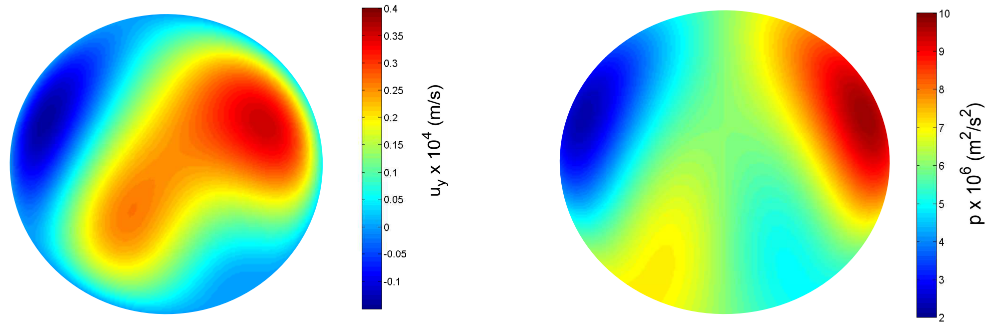

(a) Velocity distribution

(b) Pressure distribution

Fig. 5.50: Fifth-order inlet boundary condition, ditrubutions across the section. Velocity (a) and pressure (b).

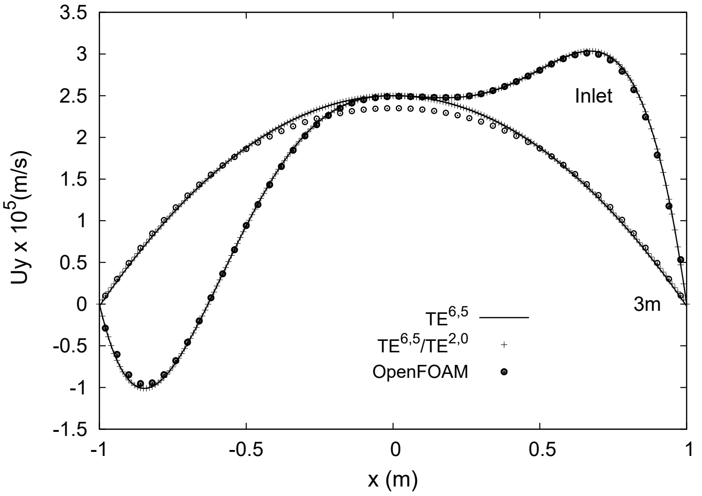

Fig. 5.51: Comparison of the velocity distribution between CUF-1D models and OpenFOAM results at inlet and midspan cross-section. Fifth-order inlet velocity profile.

- One-dimensional models are able to predict the evolution of complex flows in presence of different Dirichlet boundary conditions at the inlet.
- The models with node-dependent kinematics allow to describe flow parameters without any loss of accuracy and saving computational effort when compared to commercial tool solutions.

5.4.3 Analysis of a flow in a square-section pipes

The validation of one-dimensional models with node-dependent kinematics has been conducted through the example of the Poiseuille flow in a circular cylinder and then has been confirmed by applying the method to more complex flows. The last numerical example is related to a second-order flow in a square-section pipe. In this case, the aim is to demonstrate the capability of the present method

Table 5.26: Maximum value of pressure at inlet y=0m and maximum axial velocity at midspan y=3m. Comparison among different 1D CUF results and OpenFoam solutions. Fifth-order inlet velocity profile.

Model	$p \times 10^6 (m^2/s^2)$	$u_y \times 10^5 (m/s)$	$NDOF$
	OpenFoam		
$OpenFOAM_a$	8.17	2.44	54400
$OpenFOAM_b$	9.08	2.35	435520
	TE		
$TE^{6,5}$	9.23	2.50	4095
$TE^{6,4}$	10.72	2.50	3909
$TE^{5,4}$	10.80	2.50	3048
	LE		
$9LE^{16,9}$	9.19	2.50	9045
$20LE^{16,9}$	9.36	2.50	19818
	NDK		
$TE^{6,5}$ / $TE^{2,0}$	9.09	2.50	1379

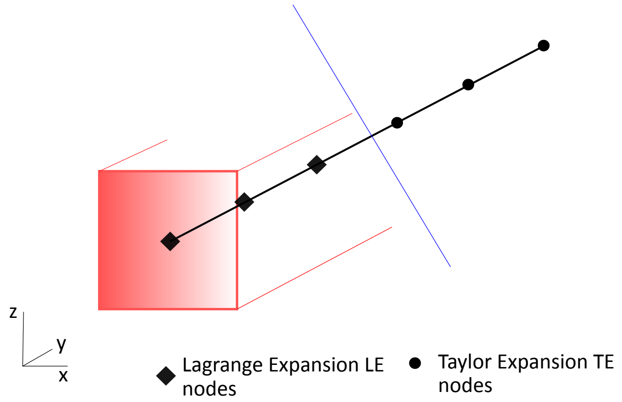

Fig. 5.52: Scheme of the one-dymensional model with mixed kinematics LE/TE.

also in the analysis of non-conventional pipes and to show the capabilities of a model with a mixed LE/TE kinematics, as shown in the scheme in Fig. 5.52. The flow considered keeps the same viscosity of the previous cases as well as for the boundary conditions on the outlet and lateral surfaces. At the inlet section, a second-order velocity profile is enforced. Figure 5.53 shows the behavior of the pressure field along the square-section pipe. TE models have not a good response at the beginning of the pipe, even using higher-order polynomials. This approach leads to an accurate descritpion of the velocity and the pressure fields, even in the proximity of the inlet cross section where a $4LE^{9,4}$ model is used. At the same time, the use of a $TE^{4,0}$ models elsewhere entails a reduction of the computational costs. The kinematics changing at the 8^{th} node does not affect the model: the flow, in fact, keeps on his parabolic nature, as in Fig. 5.54.

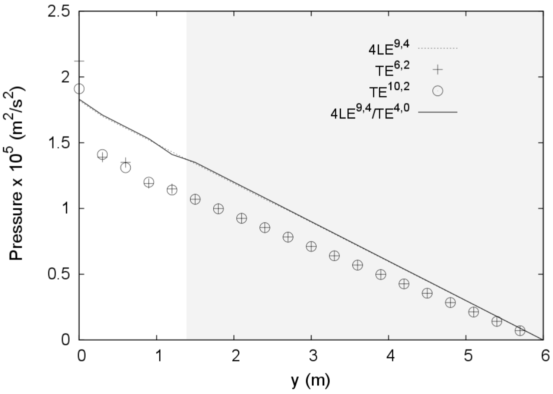

FIG. 5.53: Comaprison of pressure trends for different one-dimensional models. The gray area denotes the domain where the NDK model with $TE^{4,0}$ model has been used.

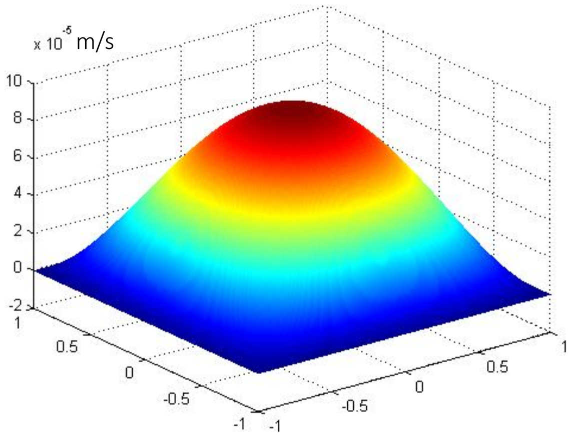

FIG. 5.54: Parabolic shape of axial velocity at 8^{th} where the change of kinematics is.

In this section the Carrera Unified Formulation has been used for the description of incompressible, laminar and viscous flows in pipes. In particular, the novel node-dependent kinematics technique has been extended to the analysis of axial flows. According to the CUF, the flow parameters are expressed as expansion of the generalised unknowns and this is possible through some interpolation functions, that can be different on each node. Different numerical examples have been considered to demonstrate the effectiveness of the present approach. Different 1D models have been employed to describe Poiseuille and higher-order flows in circular and square-section pipes. The results obtained by one-dimensional NDK models have been compared with the analyitical solution or with finite-difference solutions coming from OpenFoam freeware tool. The following considerations can be drawn from the results:

- Both 1D models, with uniform or node-dependent kinematics, are able to provide accurate results in comparison with the analytical solution.

- The NDK models provide results with a high grade of accuracy and allow a substantial saving of computational effort, with respect to the 3D solution.
- The ndk appraoch does not introduce any inconsistency in the kinematic transition area, that is, the continuity of teh velocity and pressure field is respected.

The outcomes of this research demostrates how the one-dimensional reduced models can e accurate and convenient: the efficiency of NDK models should be considered as the starting point on the modelization of complex networks as the cardiocirculatory system.

5.5 Fluid-Structure Interaction

5.5.1 Introduction

The interaction of a flexible structure with a flowing fluid in which it is submersed or by which it is surrounded gives rise to a rich variety of physical phenomena with applications in many fields of engineering, for example, the stability and response of aircraft wings, the flow of blood through arteries, the response of bridges and tall buildings to winds, the vibration of turbine and compressor blades, and the oscillation of heat exchangers. To understand these phenomena we need to model both the structure and the fluid. Due to the complexity of the problem, many challenges are still open and many researchers attempted to solve over the last years with several techinques. In general in a typical single-field mechanics problem, such as a fluid-only or structure-only problem, one begins with a set of governing differential equations in the problem domain and a set of boundary conditions on the domain boundary. The domain may or may not be in motion. The situation is more complicated in an FSI problem. The sets of differential equations and boundary conditions associated with the fluid and structure domains must be satisfied simultaneously. The domains do not overlap, and the two systems are coupled at the fluidstructure interface, which requires a set of physically meaningful interface conditions. These coupling conditions are the compatibility of the kinematics and at the fluidstructure interface.

The section here presented should be considered as the beginning of a path for the development of fluid-structure interaction within the CUF framework. The formulations untill here presented, could be the primay tools for the solution of typical FSI problems in one dimension. Due to the similarity of the formulations, structural and fluid-dynamics, it is possible to couple them directly without the introduction of any t́hird f́ield of any interface function. The CUF allows to describe the kinematic fields by using the Lagrange expansion functions; in this case the Lagrange points are adopted as interfacial links, as in Fig. 5.55.

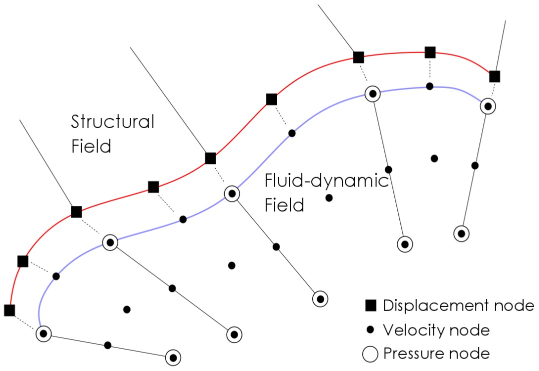

Fig. 5.55: Scheme of Lagrange points between structural and fluid-dynamic domain.

Fluid and geometry data	
ν	2.61E-05 m^2/s
U_y	0.0005 m/s
r	0.01 m
L	0.06 m
s	0.1 mm
E	0.1 MPa

TABLE 5.27: Input data of the model.

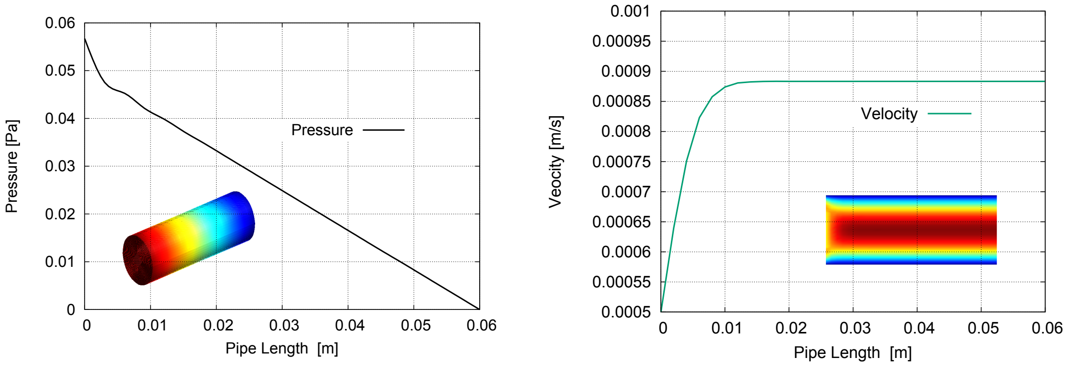

(a) Pressure distribution (b) Velocity distribution

FIG. 5.56: One-dimensional fluid-dynamic analysis of an incompressible highly viscous flow. Pressure trend (a) and velocity trend (b).

5.5.2 Circular Pipe

A very simple case is here used to assess the capabilities of the methods explained in this thesis about the structure and fluid-dynamic formulations. Although is not here considered any *coupling* condition, in the case of small deformations and displacements the following examples could be seen as starting point. The mechanical properties of a cylindrical rubber-like pipe are here investigated under the effect of the oil flow. In particular, the displacements values of the thin-walled cylinder are here reported. Tha main data of the test are resumed in Table 5.27. where ν is the kinematic viscosity, U_y is the constant inlet velocity, r is the radius of the pipe, L is the longitudinal length and finally s is the thickness. The value of viscosity belongs to a typical lubricant oil. As it concerns the structure, a rubber-like flexible material has been taken into account and E reported in the table is the Young's Modulus. The choice of this kind of material is related to the low values of pressure available from the Stokes flow. Figure 5.56 shows the pressure and the velocity trends obtained from the fluid-dynamic analysis. 48 quadratic elements L9 for the description of the velocity and 48 linear elements L4 for the description of the pressure field have been employed to compute the flow parameters. The model moreover, takes into account the no-slip condition for lateral walls and homogeneous Neumann boundary condition at the outlet section. As the Figure 5.56 suggests, the boundary condition imposed enforce the velocity field to become Poiseuille-like, while the pressure decreases linearly. As it concerns

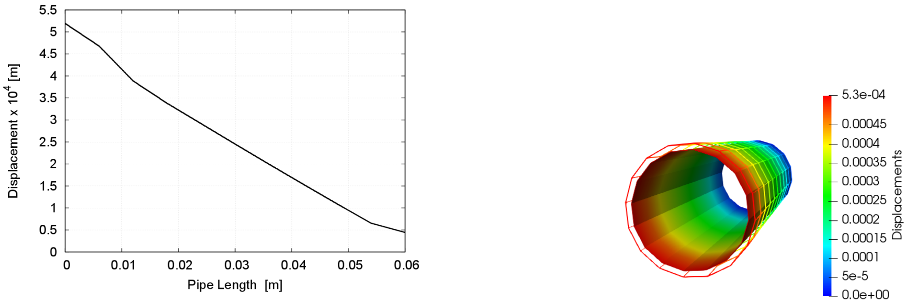

(a) Displacement trends

(b) 3D-deformed pipe

Fig. 5.57: Displacement field of a pipe subjected to fluid pressure. Linear and decay along the pipe axis (a), 3D sketch of the deformed pipe (b).

	$U_{st}^{z} \times 10^{4}$	von Mises
Inlet	5.20 m	5.30 kPa
Mid-span	2.50 m	2.40 kPa

Table 5.28: Results of displacements, von Mises stress and Plastic equivalent strain for linear and nonlinear model.

the structural domain, eight quadratic Lagrange elements have been employed to describe the thin-walled cylinder. Figure 5.57 presents the displacement trends of the pipe. As expected, the displacements values are greater close to the inlet due to the greater level of pressure, and then, it decrease quasi-linearly. The results in term of displacement and von Mises stress of the thin-walled pipe at two different coordinates can be summarized in the Table 5.28. where U_{st}^{z} is the component of structural displacement on the vertical direction.

5.5.3 Artery Profile

All the numerical examples presented in this thesis find their meeting point in this last example, discussed hereinafter. The last example of this thesis deals with the fluid-structure interaction between the linear model of artery of Section 5.1.1 and the blood flow. We must underline that the fluid here considered is not the real blood, since this accounts for higher value of Reynolds. This example aims in fact, not to represent the real physics of the problem, but rather, it would like to show the computational capabilities of the model. The fluid model makes use of 31 $LE^{9,4}$, with 14160 DOFs. On the other hand, the structural model of the artery affected by an atherosclerotic plaque is modeled by 191 LE9, and 76260 DOFs. The main flow properties are collected in the Table 5.29 where r is smallest length in x direction of the lumen, a is the largest length in z direction and l is the length along y direction of the portion of vessel. U_y is the constant velocity in y direction enforced at inlet, whereas a no-slip condition is kept on lateral walls; as in the other cases, a Neumann homogeneous boundary condition

Fluid data input	
ν	600 mm^2/s
U_y	75 mm/s
r	3.429 mm
a	12.32 mm
l	40 mm

TABLE 5.29: Fluid data input.

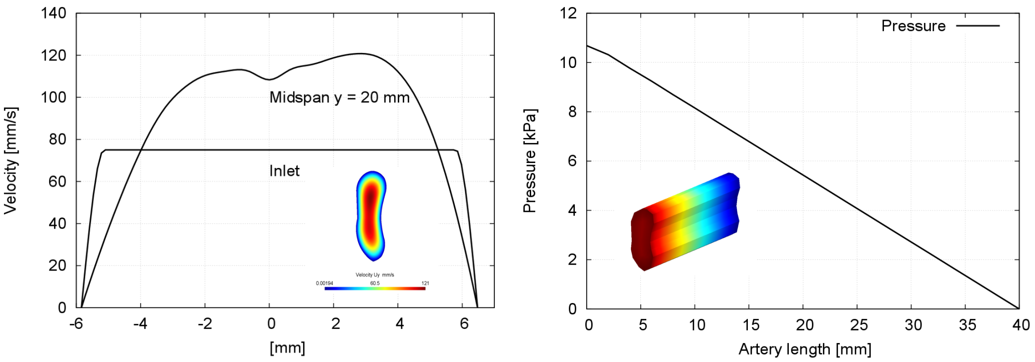

(a) Velocity trends (b) Pressure

FIG. 5.58: Fluid-dynamic analysis of blood flow whitin artery affected by atherosclerotic plaque. Axial velocity distribution along the inlet and mid-span cross-sections (a), pressure decay along the vessel(b).

is imposed at outlet section. At the end of fluid-dynamic analysis, velocity and pressure fields result as in Fig. 5.58. As visible in Fig. 5.58, the velocity distribution changes along the vessel direction, while the pressure maintains a the linear decay imposed by the boundary conditions, except at the beginning of the lumen. The pressure values obtained from the fluid-dynamic analyses were used for the linear static characterization of a portion of artery affected by atherosclerotic plaque modeled as in Section 5.1.1. It is noticed that, the application here considered is not time-dependent and not any preesure-rate is considered. By applying the decreasing pressure, as in Fig. 5.58(b), the horizontal displacement of the artery walls is greater at the beginning of the domain, as shown in Fig. 5.59(a). Due to the presence of different materials with different stiffnes, the stress and the deformations are not uniform along the cross-section, as depicted in Fig. 5.60, in which the shear deformation at mid-span cross section is shown. At the end of this section, the following comments can be done:

- Since there is no any comparison with other models, the results here presented can be seen only as a starting point for the developing of an efficient one-dimensional tool for fluid-structure interaction.
- The use of the Lagrange polynomials allows for a direct coupling between the structural and fluid-dinamic models. Even missing any numerical algorithm for the direct coupling, the number of DOFs used for the models seems to be promising.

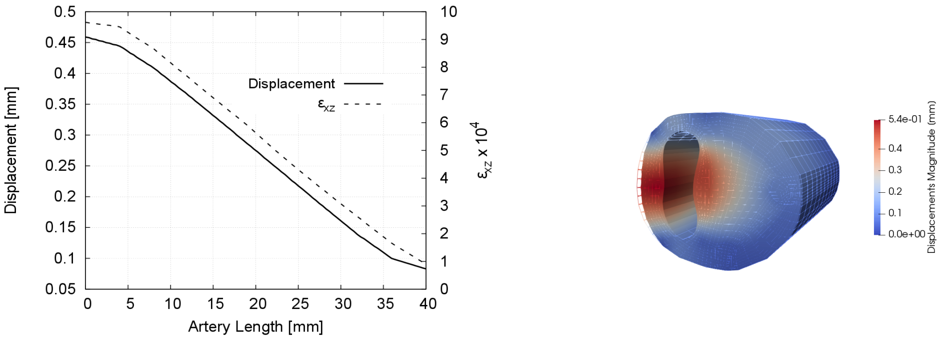

(a) Horizontal Displacement and Deformation trends

(b) Displacement Magnitude 3D-sketch

Fig. 5.59: Mechanical static resposnse of arterial walls under effect of blood flow. Displacement and deformation trends in Fibrous Cap along the vessel (a), displacement magnitude 3D sketch (b).

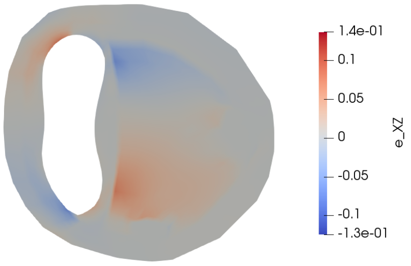

Fig. 5.60: Shear deformation at midspan-cross-section.

Chapter 6

Conclusions

The development of advanced one-dimensional models for bio-applications has been presented in this thesis. The Carrera Unified Formulation (CUF) has been used to derive structural and fluid-dynamic models in a compact manner. The hierarchical approach of this methodology provides 1D higher-order models with ease and allows the description of complex applications and a reasonable computational cost.

6.1 Remarks

The structural models presented in this thesis and the proposed results show enhanced capabilities summarised as follows:

- The compact and unified framework of the CUF allows to obtain beam models of any approximation order straightforwardly.
- Typical bio-structures issues, as concentration of stress and local effects, can be described accurately by CUF models, overcoming the limitations imposed by the classical beam theories.
- The Component-Wise (CW) approach allows to deal with multi-component and multi-material structures in linear and nonlinear regime at low computational cost. This technique ensures the continuity at the interface and does not introduce any mathematical artifice.

The 1D CUF models for fluid-dynamics demonstrated high potentialities, and the results obtained can be summarized as follows:

- The Stokes problem can be easily implemented along the CUF with ease and the Stokes flows can be accurately described with a noteworthy reduction of the computational times.

- The proposed methodology can describe the Poiseuille flow as well as non-axisymmetric flows. In addition, the enhanced capabilities of LE models allow to deal with non-cylindrical cross-section pipes.

- The novel Node-Dependent Kinematic method makes the system more flexible and allows a further reduction of the computational effort. This approach provide accurate results without the introduction of any kinematic inconsistency.

6.2 Future Developments

Future developments include the extension to other constituve models to study hyperelastic and viscoelastic materials, together with the development of more efficient fluid/structure interaction models, for the analysis of blood flow in compliant vessels. Whitin the fluid-dynamic formulation, the introduction of the convective term to the equation would be useful to study more complex fluids and enlarge the range of applicability of the formulation.

Bibliography

[1] I. Kokalari, T. Karaja, and M. Guerrisi. Review on lumped parameter method for modeling the blood flow in systemic arteries. *Journal Biomedical Science and Engineering,*, 6:92–99, 2013.

[2] Y.C. Fung. *Biomechanics: Mechanical Properties of Living Tissues.* Springer, 1993.

[3] J.M. Doyle and P.B. Dobrin. Finite deformation analysis of the relaxed and contracted dog carotid artery. *Microvascular Research*, (3):400–415, 1971.

[4] R.F. Janz and Grimm A.F. Finite-element model for the mechanical behavior of the left ventricle. prediction of deformation in the potassium-arrested rat heart. *Circulation Research*, (30):244–252, 1972.

[5] F.L. Matthews and J.B. West. Finite element displacement analysis of a lung. *Journal of Biomechanics*, (5):591–600, 1972.

[6] J.W. Farah, R.G. Craig, and D.L. Sikarskie. Photoelastic and finite element stress analysis of a restored axisymmetric first molar. *Journal of Biomechanics*, (6):511–520, 1973.

[7] T. Belytschko, R.F. Kulak, A.B. Shultz, and J.O. Galante. Finite element stress analysis of an intervertebral disc. *Journal of Biomechanics*, (7):277–285, 1974.

[8] N. Davids and M.K. Mani. A finite element analysis of endothelial shear stress for pulsatile blood flow. *Biorcheology*, (11):137–147, 1974.

[9] Y. C. Pao, E. L. Ritman, and E. H. Wood. Finite element analysis of left ventricular myocardial stresses. *Journal of Biomechanics*, (7):469–477, 1974.

[10] N. S. Hakim and A. I. King. A computer-aided technique for the generation of a 3-d finite element model of a vertebra. *Computers in Biology and Medicine*, (8):187–196, 1978.

[11] C. A. Vinson, D. G. Gibson, and A. L. Yettram. Analysis of left ventricular behaviour in diastole by means of finite element method. *British Heart Journal*, (41):60–67, 1979.

[12] M. Thibault. Biomechanics of brain tissue. *Acta Biomaterialia*, 7(1):83 – 95, 2011.

[13] C. H. Turner. Biomechanics of bone: Determinants of skeletal fragility and bone quality. *Osteoporosis International*, 13(2):97–104, Feb 2002.

[14] M.L. Cordova. Biomechanics of musculoskeletal injury. *Journal of Athletic Training*, (33):378, 1998.

[15] G. A. Holzapfel, M. Stadler, and C.A.J. Schulze-Bauer. A layer-specific three-dimensional model for the simulation of balloon angioplasty using magnetic resonance imaging and mechanical testing. *Annals of Biomedical Engineering*, 30(6):753–767, 2002.

[16] N. Oreskes, K. Shrader-Frechette, and K. Belitz. Verification, validation, and confirmation of numerical models in the earth sciences. *Science*, 263(5147):641–646, 1994.

[17] R. H. Taylor, S. Lavallee, G.C. Burdea, and R. Mosges. Introduction. in: Computer-integrated surgery: Technology and clinical applications. *MIT Press*, pages xiii–xix, 1996.

[18] S. Graham, R. Taylor, and M. Vannier. Needs assessment for computer-integrated surgery systems. *MICCAI 2000, Lecture Notes in Computer Science*, (1935):931–939, 2000.

[19] K. Miller, A. Wittek, and G. Joldes. Biomechanical modeling of the brain for computer-assisted neurosurgery. *Biomechanics of the Brain*, pages 111–136, 2011.

[20] A. Wittek, N. M. Grosland, G. R. Joldes, V. Magnotta, and K. Miller. From finite element meshes to clouds of points: A review of methods for generation of computational biomechanics models for patient-specific applications. *Annals of Biomedical Engineering*, 44(1):3–15, Jan 2016.

[21] E. Carrera and G. Giunta. Refined beam theories based on a unified formulation. *International Journal of Applied Mechanics*, 2(01):117–143, 2010.

[22] E. Carrera, G. Giunta, P. Nali, and M. Petrolo. Refined beam elements with arbitrary cross-section geometries. *Computers & structures*, 88(5-6):283–293, 2010.

[23] E. Carrera, M. Cinefra, and M. Petrolo. Comparisons between 1D (Beam) and 2D (Plate/Shell) finite elements to analyze thinwalled structures. *Aerotecnica Missili & Spazio*, 93(1-2):3–16, 2016.

[24] E. Carrera and M. Petrolo. Refined beam elements with only displacement variables and plate/shell capabilities. *Meccanica*, 47(3):537–556, 2012.

[25] E. Carrera and M. Petrolo. Refined one-dimensional formulations for laminated structure analysis. *AIAA journal*, 50(1):176–189, 2012.

[26] E. Carrera, M. Filippi, and E. Zappino. Free vibration analysis of laminated beam by polynomial, trigonometric, exponential and zig-zag theories. *Journal of Composite Materials*, 48(19):2299–2316, 2014.

[27] E. Carrera, M. Filippi, and E. Zappino. Laminated beam analysis by polynomial, trigonometric, exponential and zig-zag theories. *European Journal of Mechanics-A/Solids*, 41:58–69, 2013.

[28] A. Pagani, A.G. De Miguel, M. Petrolo, and E. Carrera. Analysis of laminated beams via unified formulation and legendre polynomial expansions. *Composite Structures*, 156:78–92, 2016.

[29] A.G. De Miguel, A. Pagani, W. Yu, and E. Carrera. Micromechanics of periodically heterogeneous materials using higher-order beam theories and the mechanics of structure genome. *Composite Structures*, 180:484–496, 2017.

[30] E. Carrera, A.G. de Miguel, and A. Pagani. Component-wise analysis of laminated structures by hierarchical refined models with mapping features and enhanced accuracy at layer to fiber-matrix scales. *Mechanics of Advanced Materials and Structures*, 25(14):1224–1238, 2018.

[31] G. De Pietro, G. Giunta, S. Belouettar, and E. Carrera. A static analysis of three-dimensional sandwich beam structures by hierarchical finite elements modelling. *Journal of Sandwich Structures & Materials*, pages –, 2017.

[32] I. Kaleel, M. Petrolo, A.M. Waas, and E. Carrera. Micromechanical progressive failure analysis of fiber-reinforced composite using refined beam models. *Journal of Applied Mechanics*, 85(2):–, 2018.

[33] I. Kaleel, M. Petrolo, and E. Carrera. Elastoplastic and progressive failure analysis of fiber-reinforced composites via an efficient nonlinear microscale model. *Aerotecnica Missili & Spazio*, 97(2):103–110, 2018.

[34] E. Carrera, M. Petrolo, and P. Nali. Unified formulation applied to free vibrations finite element analysis of beams with arbitrary section. *Shock and Vibration*, 18(3):485–502, 2011.

[35] G. Giunta, F. Biscani, S. Belouettar, A.J.M. Ferreira, and E. Carrera. Free vibration analysis of composite beams via refined theories. *Composites Part B: Engineering*, 44(1):540–552, 2013.

[36] Y. Hui, G. Giunta, S. Belouettar, Q. Huang, H. Hu, and E. Carrera. A free vibration analysis of three-dimensional sandwich beams using hierarchical one-dimensional finite elements. *Composites Part B: Engineering*, 110:7–19, 2017.

[37] G. Giunta, S. Belouettar, and E. Carrera. Analysis of fgm beams by means of classical and advanced theories. *Mechanics of Advanced Materials and Structures*, 17(8):622–635, 2010.

[38] G. Giunta, D. Crisafulli, S. Belouettar, and E. Carrera. Hierarchical theories for the free vibration analysis of functionally graded beams. *Composite Structures*, 94(1):68–74, 2011.

[39] D. S. Mashat, E. Carrera, A. M. Zenkour, S. A Al Khateeb, and M. Filippi. Free vibration of fgm layered beams by various theories and finite elements. *Composites Part B: Engineering*, 59:269–278, 2014.

[40] G. De Pietro, Y. Hui, G. Giunta, S. Belouettar, E. Carrera, and H. Hu. Hierarchical one-dimensional finite elements for the thermal stress analysis of three-dimensional functionally graded beams. *Composite Structures*, 153:514 – 528, 2016.

[41] E. Carrera and M. Petrolo. On the effectiveness of higher-order terms in refined beam theories. *Journal of Applied Mechanics*, 78(2):021013, 2011.

[42] E. Carrera, F. Miglioretti, and M. Petrolo. Computations and evaluations of higher-order theories for free vibration analysis of beams. *Journal of Sound and Vibration*, 331(19):4269–4284, 2012.

[43] E. Carrera, M. Maiarú, M. Petrolo, and G. Giunta. A refined 1d element for the structural analysis of single and multiple fiber/matrix cells. *Composite Structures*, 96:455–468, 2013.

[44] A. Varello, E. Carrera, and L. Demasi. Vortex lattice method coupled with advanced one-dimensional structural models. *Journal of Aeroelasticity and Structural Dynamics*, 2(2), 2011.

[45] A. Varello, A. Lamberti, and E. Carrera. Static aeroelastic response of wing-structures accounting for in-plane cross-section deformation. *International Journal of Aeronautical and Space Sciences*, 14(4):310–323, 2013.

[46] A. Pagani, M. Petrolo, and E. Carrera. Flutter analysis by refined 1d dynamic stiffness elements and doublet lattice method. *Advances in aircraft and spacecraft science*, 1(3):291–310, 2014.

[47] M. Petrolo. Advanced 1d structural models for flutter analysis of lifting surfaces. *International Journal of Aeronautical and Space Sciences*, 13(2):199–209, 2012.

[48] M. Petrolo. Flutter analysis of composite lifting surfaces by the 1d carrera unified formulation and the doublet lattice method. *Composite Structures*, 95:539–546, 2013.

[49] E. Carrera and E. Zappino. Aeroelastic analysis of pinched panels in supersonic flow changing with altitude. *Journal of Spacecraft and Rockets*, 51(1):187–199, 2013.

[50] E. Carrera and M. Filippi. Variable kinematic one-dimensional finite elements for the analysis of rotors made of composite materials. *Journal of Engineering for Gas Turbines and Power*, 136(9):092501, 2014.

[51] E. Carrera, E. Zappino, and M. Petrolo. Analysis of thin-walled structures with longitudinal and transversal stiffeners. *Journal of Applied Mechanics*, 80(1):011006, 2013.

[52] M. Filippi and E. Carrera. Capabilities of 1d cuf-based models to analyse metallic/composite rotors. *Advances in Aircraft and Spacecraft Science*, 3(1):1–14, 2016.

[53] E. Carrera and M. Filippi. Variable kinematic one-dimensional finite elements for the analysis of rotors made of composite materials. *Journal of Engineering for Gas Turbines and Power*, 136(9):art. n. 092501, 2014.

[54] E. Carrera, M. Filippi, and E. Zappino. Free vibration analysis of rotating composite blades via carrera unified formulation. *Composite Structures*, 106:317–325, 2013.

[55] A. Varello and E. Carrera. Nonhomogeneous atherosclerotic plaque analysis via enhanced 1d structural models. *Smart Structures and Systems*, 13(4):659–683, 2014.

[56] E. Carrera, D. Guarnera, and A. Pagani. Static and free-vibration analyses of dental prosthesis and atherosclerotic human artery by refined finite element models. *Biomechanical Modeling and Mechanobiology*, 2:301–317, 2018.

[57] G. Giunta, D. Crisafulli, S. Belouettar, and E. Carrera. A thermo-mechanical analysis of functionally graded beams via hierarchical modelling. *Composite Structures*, 95:676–690, 2013.

[58] M. Cinefra, M. Petrolo, G. Li, and E. Carrera. Variable kinematic shell elements for composite laminates accounting for hygrothermal effects. *Journal of Thermal Stresses*, 40(12):1523–1544, 2017.

[59] G. Giunta, Y. Koutsawa, and S. Belouettar. Analysis of three-dimensional piezo-electric beams via a unified formulation. In *Advanced Materials Research*, volume 745, pages 101–118. Trans Tech Publ, 2013.

[60] E. Zappino, E. Carrera, S. Rowe, C. Mangeot, and H. Marques. Numerical analyses of piezoceramic actuators for high temperature applications. *Composite Structures*, 151:36–46, 2016.

[61] F. Biscani, G. Giunta, S. Belouettar, E. Carrera, and H. Hu. Variable kinematic beam elements coupled via arlequin method. *Composite Structures*, 93(2):697–708, 2011.

[62] E. Carrera, A. Pagani, and M. Petrolo. Use of lagrange multipliers to combine 1d variable kinematic finite elements. *Computers & Structures*, 129:194–206, 2013.

[63] E. Carrera and E. Zappino. One-dimensional finite element formulation with node-dependent kinematics. 2017. Submitted.

[64] E. Carrera, E. Zappino, and G. Li. Analysis of beams with piezo-patches by node-dependent kinematic finite element method models. *Journal of Intelligent Material Systems and Structures*, 29(7):1379–1393, 2018.

[65] E. Zappino, G. Li, A. Pagani, and E. Carrera. Global-local analysis of laminated plates by node-dependent kinematic finite elements with variable esl/lw capabilities. *Composite Structures*, 172:1–14, 2017.

[66] E. Carrera, M. Filippi, and E. Zappino. Node-dependent kinematic one-dimensional models for the analysis of rotating structures. In *ASME 2017 International Mechanical Engineering Congress and Exposition*, pages V04BT05A065–V04BT05A065. American Society of Mechanical Engineers, 2017.

[67] E. Carrera, M. Petrolo, and A. Varello. Advanced beam formulations for free-vibration analysis of conventional and joined wings. *Journal of Aerospace Engineering*, 25(2):282–293, 2011.

[68] E. Carrera, A. Pagani, and M. Petrolo. Classical, refined, and component-wise analysis of reinforced-shell wing structures. *AIAA journal*, 51(5):1255–1268, 2013.

[69] E. Carrera, A. Pagani, and M. Petrolo. Component-wise method applied to vibration of wing structures. *Journal of Applied Mechanics*, 80(4):041012, 2013.

[70] E. Carrera, M. Maiarú, and M. Petrolo. Component-wise analysis of laminated anisotropic composites. *International Journal of Solids and Structures*, 49(13):1839–1851, 2012.

[71] A. Quarteroni L. Formaggia and A. Veneziani. *Cardiovascular Mathematics*, volume 1. 2009.

[72] C.B. Vreugdenhil. *Numerical Methods for Shallow/Water Flows*. 1998.

[73] L. Euler. *Principia pro motu sanguinis per arterias determinando*, volume 2. 1775.

[74] Y.C. Fung. *Biomechanics: Circulation*. 1997.

[75] S. Perotto, A. Reali, P. Rusconi, and A. Veneziani. Higamod: A hierarchical isogeometric approach for {MODel} reduction in curved pipes. *Computers and Fluids*, 142:21 – 29, 2017. Selected papers of 18th International Conference on Finite Elements in Flow Problems.

[76] L. Formaggia, J.F. Gerbeau, F. Nobile, and A. Quarteroni. On the coupling of 3d and 1d navier - stokes equations for flow problems in compliant vessels. *Computational Methods in Applied Mechanics and Engineering*, pages 561–582, 2001.

[77] F. Salmoiraghi, F. Ballarin, L. Heltai, and G. Rozza. Isogeometric analysis-based reduced order modelling for incompressible linear viscous flows in parametrized shapes. *Advanced Modeling and Simulation in Engineering Science*, pages 3–21, 2016.

[78] N.P. Smith, A.J. Pullan, and P.J. Hunter. An anatomically based model of transient coronary blood ow in the heart. *SIAM Journal of Applied Mathematics*, pages 990–1018, 2002.

[79] S.J. Sherewin, V. Franke, and J. Peiro. One-dimensional modelling of a vascular network in space-time variables. *Journal of Engineering Mathematics*, pages 217–250, 2003.

[80] L. Formaggia, D. Lamponi, and A. Quarteroni. One-dimensional models for blood flow in arteries. *Journal of Engineering Mathematics*, pages 251–279, 2003.

[81] S.S. Ravindran. Reduced-order approach for optimal control of fluids using proper orthogonal decomposition. *Int. Journal Numerical Methods and Fluids*, 2000.

[82] A. Quarteroni and G. Rozza. Numerical solution of parametrized navier-stokes equations by reduced basis methods. *Numer. Methods Partial Differential Eq.*, pages 923 – 948, 2006.

[83] S. Perotto, A. Ern, and A. Veneziani. Hierarchical local model reduction for elliptic problems i: a domain decomposition approach. *A SIAM Interdisciplinary Journal*, 8:1102–1127, 1775.

[84] A. Varello. Advanced higher-order one-dimensional models for fluid-structure interaction analysis. *Ph.D Thesis*, 2013.

[85] A. Varello, A. Pagani, D. Guarnera, and E. Carrera. Analysis of Stokes flows by Carrera Unfied Formulation. *Advances in Aircraft and Spacecraft Science.*, 2018.

[86] A. Pagani. Component-wise models for static,dynamic and aeroelastic analyses of metallic and composite aerospace structures. *Ph.D Thesis*, 2015.

[87] S.W. Tsai. *Composites Design.* Dayton, Think Composites, 4th edition, 1988.

[88] J.N. Reddy. *Mechanics of laminated composite plates and shells. Theory and Analysis.* CRC Press, 2^{nd} edition, 2004.

[89] E. Carrera, M. Filippi, P. K. R. Mahato, and A. Pagani. Advanced models for free vibration analysis of laminated beams with compact and thin-walled open/closed sections. *Journal of Composite Materials*, 2014.

[90] E. Carrera and S. Brischetto. Analysis of thickness locking in classical, refined and mixed multilayered plate theories. *Composite Structures*, 82(4):549–562, 2008.

[91] V.Z. Vlasov. *Thin-walled elastic beams.* National Technical Information Service, 1984.

[92] K. Washizu. *Variational Methods in Elasticity and Plasticity.* Pergamon, Oxford, 1968.

[93] E. Carrera, G. Giunta, and M. Petrolo. *Beam Structures: Classical and Advanced Theories.* John Wiley & Sons, 2011.

[94] E. Carrera and M. Petrolo. Refined beam elements with only displacement variables and plate/shell capabilities. *Meccanica*, 47(3):537–556, 2012.

[95] E. Carrera, A. Pagani, M. Petrolo, and E. Zappino. A component-wise approach in structural analysis. *Computational methods for engineering science*, 4:75–115, 2012.

[96] E. Carrera, M. Maiarú, and M. Petrolo. Component-wise analysis of laminated anisotropic composites. *International Journal of Solids and Structures*, 49:1839–1851, 2012.

[97] E. Carrera, A. Pagani, and M. Petrolo. Classical, refined and component-wise theories for static analysis of reinforced-shell wing structures. *AIAA Journal*, 51(5):1255–1268, 2013.

[98] E. Carrera, A. Pagani, and M. Petrolo. Classical, refined and component-wise theories for static analysis of reinforced-shell wing structures. *AIAA Journal*, 51(5):1255–1268, 2013.

[99] E. Carrera, A. Pagani, and M. Petrolo. Refined 1D finite elements for the analysis of secondary, primary, and complete civil engineering structures. *Journal of Structural Engineering*, 141(4):art. no. 04014123, 2014.

[100] E. Carrera and A. Pagani. Free vibration analysis of civil engineering structures by component-wise models. *Journal of Sound and Vibration*, 333(19):4597–4620, 2014.

[101] E. Carrera and G. Giunta. Refined beam theories based on Carreras unified formulation. *International Journal of Applied Mechanics*, 2(1):117–143, 2010.

[102] K.J. Bathe. *Finite element procedure.* Prentice Hall, 1996.

[103] B. Szabó and I. Babŭska. *Finite Element Analysis.* Wiley Interscience, 1991.

[104] E. A de Souza Neto, D. Peric, and D.R.J. Owen. *Computational methods for plasticity: theory and applications.* John Wiley & Sons, 2011.

[105] E. Carrera, I. Kaleel, and M. Petrolo. Elastoplastic analysis of compact and thin-walled structures using classical and refined beam finite element models. *Mechanics of Advanced Materials and Structures*, In Press.

[106] M. Petrolo, M.H. Nagaraj, I. Kaleel, and E. Carrera. A global-local approach for the elastoplastic analysis of compact and thin-walled structures via refined models. *Computers & Structures*, 206:54–65, 2018.

[107] A. Quarteroni. *Numerical Models for Differential Problems*, volume 1. Springer, 2009.

[108] F. Brezzi. On the existence, uniqueness and approximation of saddle-point problems arising from lagrange multipliers. *Revue Francaise de Automatique, Informatique, Recherche Operationnelle. Analyse Numerique*, 8:129–151, 1974.

[109] E. Carrera, M. Cinefra, M. Petrolo, and E. Zappino. *Finite element analysis of structures through Unified Formulation*. Wiley, 2014.

[110] V. C. Rideout and D. E. Dick. Difference-differential equations for fluid flow in distensible tubes. *IEEE Transactions on Biomedical Engineering*, 14(3):171–177, 1967.

[111] N. Westerhof, F. Bosman, C.J. De Vries, and A. Noordergraaf. Analog studies of the human systemic arterial tree. *Journal of Biomechanics*, 2(2):121–143, 1969.

[112] J. Ottesen. Tekst nh 297≫ 1995. 1995.

[113] G. Karniadakis and S. Sherwin. *Spectral/Hp Element Methods for CFD (Numerical Mathematics and Scientific Computation)*. Oxford University Press, New York, 1999.

[114] J.P. Pontaza and J.N. Reddy. Spectral/hp least-squares finite element formulation for the Navier-Stokes equations. *Journal of Computational Physics*, 190(2):523–549, 2003.

[115] S. Guzzetti, S. Perotto, and A. Veneziani. Hierarchical model reduction for incompressible fluids in pipes. *International Journal for Numerical Methods in Engineering*, 114(5):469–500, 2017.

[116] Luca Formaggia, Fabio Nobile, Alfio Quarteroni, and Alessandro Veneziani. Multiscale modelling of the circulatory system: a preliminary analysis. *Computing and visualization in science*, 2(2-3):75–83, 1999.

[117] E. Carrera and E. Zappino. One-dimensional finite element formulation with node-dependent kinematics. *Computers and Structures*, 192:114–125, 2017.

[118] E. Carrera, E Zappino, and G Li. Finite element models with node-dependent kinematics for the analysis of composite beam structures. *Composites Part B: Engineering*, 132:35–48, 2018.

[119] G. Zappino, E.and Li and E. Carrera. Node-dependent kinematic elements for the dynamic analysis of beams with piezo-patches. *Journal of Intelligent Material Systems and Structures*, 29(16):3333–3345, 2018.

[120] E. Carrera, E. Zappino, and G. Li. Finite element models with node-dependent kinematics for the analysis of composite beam structures. *Composites Part B: Engineering,*, 132:35–48, 2018.

[121] G. Holzapfel, G. Sommer, and P. Regitnig. Anisotropic mechanical properties of tissue components in human atherosclerotic plaques. *Journal of Biomechanical Engineering*, 126:657–665, 2004.

[122] D. Balzani, S. Brinkhues, and G. Holzapfel. Constitutive framework for the modeling of damage in collagenous soft tissues with application to arterial walls. *Computer Methods in Applied Mechanics and Engineering*, pages 139–151, 2011.

[123] A. Varello and E. Carrera. Nonhomogeneous atherosclerotic plaque analysis via enhanced 1D structural models. *Smart Structures and Systems*, 13(4):659–683, 2014.

[124] R. J. Allemang and D. L. Brown. A correlation coefficient for modal vector analysis. In *Proceedings of the International Modal Analysis Conference*, pages 110–116, Orlando, Florida, USA, 1982.

[125] E. Carrera, A. Pagani, and M. Petrolo. Component-wise method applied to vibration of wing structures. *Journal of Applied Mechanics*, 80(4):art. no. 041012 1–15, 2013.

[126] R. Burge, B. Dawson-Hughes, D. H. Solomon, J. B. Wong, A. King, and A. Tosteson. Incidence and economic burden of osteoporosis-related fractures in the united states, 2005–2025. *Journal of bone and mineral research*, 22(3):465–475, 2007.

[127] J. Koreska, D. Robertson, R.H. Mills, D.A. Gibson, and A.M. Albisser. Biomechanics of the lumbar spine and its clinical significance. *The Orthopedic clinics of North America*, 8(1):121–133, 1977.

[128] J.S.S Wu and J.H. Chen. Clarification of the mechanical behaviour of spinal motion segments through a three-dimensional poroelastic mixed finite element model. *Medical engineering & physics*, 18(3):215–224, 1996.

[129] K. G. Faulkner, S. R. Cummings, D. Black, L. Palermo, C.-C Glüer, and H. K. Genant. Simple measurement of femoral geometry predicts hip fracture: the study of osteoporotic fractures. *Journal of bone and mineral research*, 8(10):1211–1217, 1993.

[130] T. M. Keaveny. Biomechanical computed tomographynoninvasive bone strength analysis using clinical computed tomography scans. *Annals of the New York Academy of Sciences*, 1192(1):57–65, 2010.

[131] P. K. Zysset, E. Dall'Ara, P. Varga, and D. H. Pahr. Finite element analysis for prediction of bone strength. *BoneKEy reports*, 2, 2013.

[132] D. L. Kopperdahl, E. F. Morgan, and T. M. Keaveny. Quantitative computed tomography estimates of the mechanical properties of human vertebral trabecular bone. *Journal of orthopaedic research*, 20(4):801–805, 2002.

[133] X. Wang, A. Sanyal, P.M. Cawthon, L. Palermo, M. Jekir, J. Christensen, K. E. Ensrud, S. R. Cummings, E. Orwoll, D. M. Black, et al. Prediction of new clinical vertebral fractures in elderly men using finite element analysis of ct scans. *Journal of Bone and Mineral Research*, 27(4):808–816, 2012.

[134] T.M. Jackman, A. M. DelMonaco, and E. F. Morgan. Accuracy of finite element analyses of ct scans in predictions of vertebral failure patterns under axial compression and anterior flexion. *Journal of biomechanics*, 49(2):267–275, 2016.

[135] M. J. Silva, T. M. Keaveny, and W. C. Hayes. Computed tomography-based finite element analysis predicts failure loads and fracture patterns for vertebral sections. *Journal of Orthopaedic Research*, 16(3):300–308, 1998.

[136] T. M. Keaveny, D. W. Donley, P. F. Hoffmann, B. H. Mitlak, E. V. Glass, and J. A. San Martin. Effects of teriparatide and alendronate on vertebral strength as assessed by finite element modeling of qct scans in women with osteoporosis. *Journal of bone and mineral research*, 22(1):149–157, 2007.

[137] V. Shim, J. Fernandez, P. Gamage, C. Regnery, D. Smith, B. Gardiner, D. Lloyd, and T. Besier. Subject-specific finite element analysis to characterize the influence of geometry and material properties in achilles tendon rupture. *Journal of Biomechanics*, 47:3598–3604, 2014.

[138] T. Wren, D. Lidsey, G. Beaupr, and D. Carter. Effects of creep and cyclic loading on the mechanical properties and failure of human achilles tendons. *Ann. of Biomed. Engineering*, 31:710–717, 2003.

[139] D. Butler, G. Edward, N. Frank, Z. Ronald, and K. Brackett. Effects of structure and strain measurement technique on the material properties of young human tendons and fascia. *Journal of Biomechanics*, 17:579–596, 1984.

[140] M. Kongsgaard, P. Aagaard, M. Kjaer, and S. P. Magnusson. Structural achilles tendon properties in athletes subjected to different exercise modes and in achilles tendon rupture patients. *Journal of Applied Physiology*, 99:1965–1971, 2005.

[141] D. Tang, C. Yang, J. Zheng, P. Woodard, J. Saffitz, J. Petruccelli, G. Sicard, and C. Yuan. Local maximal stress hypothesis and computational plaque vulnerability index for atherosclerotic plaque assessment. *Ann Biomed Eng.*, 33:1789–1801, 2005.

[142] S. Stera and R. Skalak. *The history of Poiseuille's Law.* 1993.

[143] OpenFOAM Fundation. OpenFOAM. www.openfoam.com, 2011–2014.

Publications

- Guarnera, D., Zappino, E., Pagani, A. and Carrera, E., 2019.

  Finite elements with node dependent kinematics and scalable accuracy for the analysis of Stokes flows.

  Aerotecnica, Missili & Spazio.

- Varello, A., Pagani, A., Guarnera, D., and Carrera, E., 2018.

  Analysis of Stokes flows by Carrera Unified Formulation.

  Advances in Aircraft and Spacecraft Science.

- Carrera, E., Guarnera, D., and Pagani, A., 2018.

  Static and free-vibration analyses of dental prosthesis and atherosclerotic human artery by refined finite element models.

  Biomechanical Modeling and Mechanobiology.

  Guarnera, D., Zappino, E., Pagani, A. and Carrera, E., 2018.

  Finite Element Models of One-Dimensional Flows with Node-Dependent Accuracy.

  Proceedings of ASME 2018 International Mechanical Engineering Congress and Exposition (IMECE), Nov 2018, Pittsburgh, Pennsylvania, US.

- Guarnera, D., Carrera, E., Kaleel, I., Pagani, A. and Petrolo, M., 2018.

  Non-Linear analysis of bio-structures through refined beam models.

  Proceedings of ASME 2018 International Mechanical Engineering Congress and Exposition (IMECE), Nov 2018, Pittsburgh, Pennsylvania, US.

- Guarnera, D., Carrera, E., Kaleel, I., Pagani, A. and Petrolo, M., 2018.

  Advanced models for nonlinear static response of biological structures

  Proceedings of the 1st International Conference on Mechanics of Advanced Materials and Structures (ICMAMS), June 2018, Turin, Italy.

- Carrera, E., Guarnera, D., and Pagani, A., 2017.

  Higher-Order modelling of One-Dimensional Flows.

Proceedings of the 23rd Conference of the Italian Association of Theoretical and Applied Mechanics (AIMETA), Sep 2017, Salerno, Italy.

- Carrera, E., Cinefra, M., Filippi, M., Pagani, A., Petrolo, M., Zappino, E., Garcia, A., Kaleel, I., Manish, N., Li, G., Guarnera, D., Viglietti, A. and Valvano, S., 2017.

  Advanced numerical methods for failure analysis of metallic and composite aerospace structures.

  Proceedings of the technical interchange meeting (TIM) on fracture control of spacecraft, launchers and their payloads and experiments.

- Pagani, A., Guarnera, D., and Carrera, E., 2016

  Unified theory of one-dimensional structures and flows with applications to biomedical engineering and coupled problems.

  Proceedings of the European Congress on Computational Methods in Applied Sciences and Engineering, (ECCOMAS), June 2016, Crete, Greece.